Université de Strasbourg

UNIVERSITÉ DE STRASBOURG

EDSC École Doctorale des Sciences Chimiques

ÉCOLE DOCTORALE ED222

UMR 7006

THÈSE présentée par :

Kripa Merin JOSEPH

soutenue le : **22 Septembre 2022**

pour obtenir le grade de : **Docteur de l'université de Strasbourg**

Discipline/ Spécialité : Chimie Physique

Conductivity and supramolecular assembly under light-matter strong coupling

Conductivité et assemblage supramoléculaire sous couplage fort lumière-matière

THÈSE dirigée par :

M. EBBESEN Thomas	Professor, ISIS, Université de Strasbourg

RAPPORTEURS :

M. NITZAN Abraham	Professor, University of Pennsylvania
M. DEGIRON Aloyse	Chargé de Recherche, CNRS & Université Paris Cité

AUTRES MEMBRES DU JURY :

Mme. HELLWIG Petra	Professor, Chimie de la Matière Complexe, Université de Strasbourg

---

INVITÉ :

M. GENET Cyriaque	Directeur de Recherche, ISIS, CNRS & Université de Strasbourg
M. MORAN Joseph	Professor, ISIS, Université de Strasbourg

“If you want to find the secrets of the universe, think in terms of frequency, energy, and vibrations.”

-Nikola Tesla

CONTENTS

ABBREVIATIONS AND SYMBOLS

QED	Quantum electrodynamics
EM	Electromagnetic
cQED	Cavity quantum electrodynamics
R-L-C circuit	Resistor-Inductor-capacitor circuit
SPs	Surface plasmons
RCE	Resonance cavity effect
VCSELs	Vertical cavity surface emitting lasers
DBR	Distributed Bragg reflector
WM	Wannier- Mott
OSC	Organic semiconductors
ESC	Electronic strong coupling
VSC	Vibrational strong coupling
FP cavity	Fabry-Perot cavity
RWA	Rotating wave approximation
FWHM	Full- width at half-maximum
DBR	Distributed Bragg reflector
SPPs	Surface plasmon polaritons
FTIR	Fourier-transform infrared
ATR	Attenuated total reflectance
PVA	poly (vinyl alcohol)
PMMA	poly(methyl methacrylate)

PPE	poly(*p*-phenylene ethynylene)
OPE	Oligo phenylene ethynylene
dcb	o-dichlorobenzene
D_4-dcb	Deuterated o-dichlorobenzene
rr-P3HT	regio-regular poly(3-hexylthiophene)
SEM	scanning electron microscopy
TEM	transmission electron microscopy
σ	Conductivity
Si	Silicon
PEDOT: PSS	poly(3,4-ethylene dioxythiophene) polystyrene sulfonate

PREFACE

The interaction between light and matter is responsible for numerous day-to-day observations, such as the formation of a rainbow, the reflection in the mirror, the multi-colored oil spill on water due to interference, or the sky or oceans appearing blue due to Rayleigh scattering. These interactions can be used to investigate the properties of matter through spectroscopic techniques involving fundamental processes such as absorption, emission, transmission, diffraction, and reflection. Nearly a hundred years ago, Dirac, laid the foundations of quantum electrodynamics (QED) which changed our understanding of such light-matter interactions.[1] QED can be thought of as the fusion of electromagnetism and quantum physics. Of particular interest in the context of this thesis, is the so-called cavity QED where matter is placed in the confined field of a cavity which can enhance the interaction between light and matter and thereby give rise to new phenomena. For instance, it is possible to generate hybrid light-matter states, known as polaritonic states, by so-called light-matter strong coupling. The presence of these states naturally changes the material and chemical properties of the system.

In the early 1970s, the prime focus of cQED was on 'atoms in perturbative regime', which slowly transitioned to 'semiconductor physics in cavities' by the end of 1980s. Over the last two decades, the significant effect of light-matter strong coupling[2] on molecular and chemical properties such as conductivity[3–15], work-function[16], non-linear optics[17], chemical kinetics,[18–22], and magnetism[23] has attracted much attention from researchers. Coupling of molecular absorption and an optical mode leads to the generation of hybrid light-matter states, called polaritonic states, which are delocalized over many molecules. In addition to the bright

states (P+ and P-), dark states are also formed. This coupling is possible even in the dark due to the interaction with the zero-point energies of the optical mode. Due to extended coherence and delocalization of hybrid light-matter states, transport properties benefit from strong coupling. [3–15] The original focus of this thesis was to study changes in the conductivity of organic semiconductors when the molecular vibrations of the material are coupled (so-called vibrational strong coupling or VSC). However, in the course of the work, other issues emerged, in particular the effects of strong coupling on intermolecular interactions and self-assembly. The thesis is organized as follows:

- The first chapter introduces the fundamentals of cavity quantum electrodynamics and its consequences on atomic physics, semiconductors, and material chemistry.

- The second chapter gives a theoretical outline of light-matter coupling through the most straightforward approach – the Jaynes-Cummings model and gives a brief overview of different regimes of light-matter coupling. This is followed by a comparative discussion of charge transport theories of organic semiconductors through polaronic/ hopping and band transport models, the two opposite limiting regimes.

- In the third chapter, we study the effect of light-matter strong coupling on conductivity and photoconductivity of p-type organic semiconductor *rr*-P3HT. This chapter demonstrates that under ultra-strong coupling, the ground state has a finite photonic content, and thus even the valence band is modified, leading to an enhancement of conductivity and photoconductivity of the p-type organic semiconductor.

- The fourth chapter reports the serendipitous observation of the modification of the morphology of supramolecular assembly under VSC of a conjugated conducting polymer poly(*p*-phenylene ethynylene) through a cooperative effect. The chapter also includes a similar modification observed for a conjugated monomer - oligo(*p*-phenylene ethynylene).

- The fifth chapter focuses on the enhancement of conductivity of the highly conducting polymer – poly(3,4-ethylene dioxythiophene) polystyrene sulphonate (PEDOT: PSS) by strongly coupling its vibrational bands to the plasmonic resonance of metallic gratings. It involved a collaborative effort in order to obtain plasmonic structures with resonances having quality factors necessary to achieve strong coupling condition.

- Sixth chapter: Conclusion and outlook.

1.

LIGHT-MATTER STRONG COUPLING: A NEW TOOL FOR MODULATING MOLECULAR PROPERTIES

The 20th century marked the beginning of quantum physics with some revolutionary postulates from Planck and Einstein, with the former proposing that the energy of any mode of oscillation is quantized and that is equal to the mode's frequency times a constant, Planck's constant.[24] This fundamental equation, E=hv, motivated Einstein to publish his famous quantum paper in 1905, proposing that light consists of discrete quantum particles or 'wave packets of energy', later called photons. Unlike Planck, Einstein applied energy quantization to the radiation field. After more than a decade, he also put forth the idea that excited atoms emit photons and return to a lower energy state to achieve thermal equilibrium, a process he called "spontaneous emission".[25] In 1913, both these works and Rutherford's planetary model of the atom were intertwined by Niels Bohr in his theory of atomic spectra, which correctly described the emission spectrum of hydrogen.[26] It was the quantum mechanical theory developed by Dirac in 1926 that played a crucial role in laying the foundations of QED; in this theory, the radiation field and the emitter are coupled such that fluorescence is understood to

be an emission into an optical vacuum state.[1] By vacuum, we mean 3D space, not a material void. These vacuum states are quantum states with zero-point energy that thereby generate electromagnetic fluctuations. Later in 1932, Enrico Fermi, using Dirac's theory, proposed that spontaneous emission rate also depends on the local photonic mode density, now known as Fermi's golden rule.[27] This has since been well verified. Spontaneous fluorescence is actually triggered by vacuum electromagnetic fluctuations and the radiative rate and the fluorescence quantum yield depends on this density of states.

The virtual photons associated with vacuum fluctuations disappear as soon as they are formed and hence do not violate energy conservation. In the late 1940s, Willis Lamb reported the spectral shift of the hydrogen atom, the first evidence of the impact of vacuum fluctuations.[28] It is also a demonstration that vacuum fluctuations affect the properties of matter, a topic of this thesis. The evolution of QED led to an important sub-field known as cavity QED (cQED); the following section will briefly browse through its history.

1.1. Cavity quantum electrodynamics: A brief history

cQED is concerned with light-matter interactions in the confined EM fields of a cavity and other optical resonators. Through progressive improvements in the design of high finesse cavities and atom manipulations, this has led to a revolution in laser metrology, attosecond physics, atomic clock precision, quantum information, and solid-state devices. In 1946, Purcell and his colleagues showed how cQED enhances the spontaneous emission rate of nuclear magnetic transitions when coupled to a resonant R-L-C circuit, at radio frequencies.[29] The seminal paper defined the 'Purcell factor' η which quantifies the coupling between an emitter and a cavity mode.[30] In the late 1960s, Karl Drexhage reported how the spontaneous emission

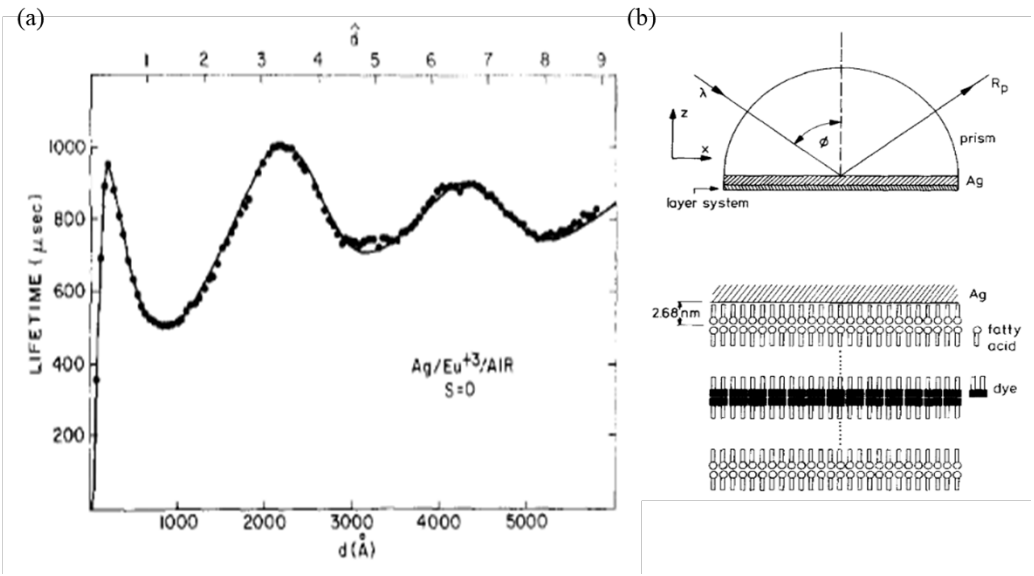

Figure 1.1. (a) The lifetime of the europium complex as a function of distance from the metallic mirror was measured by Drexhage. Reproduced from ref [31], (b) the Kretschmann configuration used by Pockrand *et al*. for strongly coupling dye molecules using Langmuir-Blodgett monolayer assemblies. Reproduced from ref [32]

decay rate of dye molecules in Langmuir film varies with distance from a metallic mirror with nanometer precision (Figure 1.1).[31,33] According to QED, in Drexhage's experiments, the coupling between the radiation field and the emitter is altered. In other words, the presence of a mirror changes the 'density of states', leading to the variation of radiative lifetime of the dipole emitter. This seminal observation was another experimental evidence of a 'perturbative regime', now known as the weak coupling regime. In 1981, Kleppner predicted that spontaneous emission rate could not only be enhanced but also be inhibited in a cavity.[34] Similar experiments were reproduced much later by Barnes *et al*.[35]

By the 1970s, the focus of interest shifted from the weak coupling regime just described to the so-called light-matter strong coupling. In the latter regime, the interaction is so strong that hybrid light-matter (or polaritonic) states are formed, opening a multitude of possibilities. Following theoretical calculations,[36] the first experimental evidence demonstrating strong

coupling in an inorganic material was given by Zhizhin and his coworkers in 1975, wherein surface plasmons (SP) were coupled to the phonon modes of the material.[37] In the 1980s, coupled atom-cavities systems were studied in many laboratories around the world which allowed fundamental aspects and theoretical predictions to be studied.[38–43] The demonstration of strong coupling of excitons in semiconductors cavities [44] further broadened the field to solid-state materials. This includes several significant works on exciton-polariton dynamics,[45] photoluminescence of exciton-polaritons,[46,47] and polariton lasing. [48–51] This led to resonance cavity-enhanced (RCE) devices that have improved optoelectronics.[52] For instance, due to the increased optical field, RCE photodetectors have higher efficiency and are thinner and faster, making them technologically viable.[52] Furthermore, due to the hybrid Boson-Fermion nature of polaritons, it is possible to observe polariton condensation at high temperatures, analogous Bose-Einstein condensation, and lasing at lower threshold powers than the usual photonic lasers.[49] The first demonstration of strongly coupled organic semiconductors was reported by Pockrand and his coworkers in 1982, wherein they studied exciton-surface plasmon interactions by coupling excitons of dye molecules in Langmuir-Blodgett monolayer assemblies to the underlying metal film (Figure 1.1 b).[32] In 1998, this field was further stimulated by Fujita *et al*.[53] and Lidzey *et al*.[54] They confirmed the possibility of strong coupling of organic semiconductors (perovskites and porphyrins) in distributed feedback and Fabry-Perot microcavities, respectively.

In the last 20 years, there have been many studies on molecules and organic semiconductors under strong coupling, such as the experiments where cyanine J-aggregates are coupled to optical modes.[55–57] Interestingly, the focus of such studies was on the optical and quantum properties. About 15 years ago, the study of the consequences of light-matter strong coupling on material and chemical properties was initiated by the Strasbourg group. The

investigation of modifications of molecular properties has emerged as a new frontier of science-discussed in the following section.

1.2. Consequences of light-matter strong coupling on chemistry and material properties

The impact of light-matter strong coupling on chemical and material properties has been much greater than expected and generated considerable interest around the world for both the fundamental and the technological potential. Various properties have been analyzed and found to be changed in the strong coupling regime such as conductivity, [3–15] work-function,[16] ferromagnetism,[23] superconductivity, non-linear optics,[17] supramolecular assemblies,[58–60] ionic conductivity,[61] and chemical reactivity, [18–22] (Figure 1.2). It has emerged as a new tool to alter molecular and material properties by coupling either electronic transitions (electronic strong coupling, ESC) or vibrational modes (vibrational strong coupling, VSC). The first observation of the effect of strong coupling in chemistry was reported by Hutchison *et al.* in 2012, wherein they showed that the energy landscape of molecules could be modified under ESC through the study of spiropyran-merocyanine photoisomerization.[62] Following this work, other properties were investigated under ESC such as the work function,[16] the phase transition of hybrid perovskites,[63] enhancement in energy transfer,[64–69] and enhancement in conductivity of n- and p-type OSC [4,8–11,70]. In the third Chapter, we will present our investigation of the enhancement of the conductivity of a p-type organic semiconductor under ESC.

Following the demonstration of vibrational strong coupling (VSC) in the liquid phase,[71,72] Thomas *et al*. reported that VSC could strongly influence the ground-state chemical landscape, a surprising and exciting development.[73] In addition to the retardation in the reaction kinetics, they found that the thermodynamics was completely modified under VSC, suggesting that the reaction changed from an associative to a dissociative mechanism. These findings were

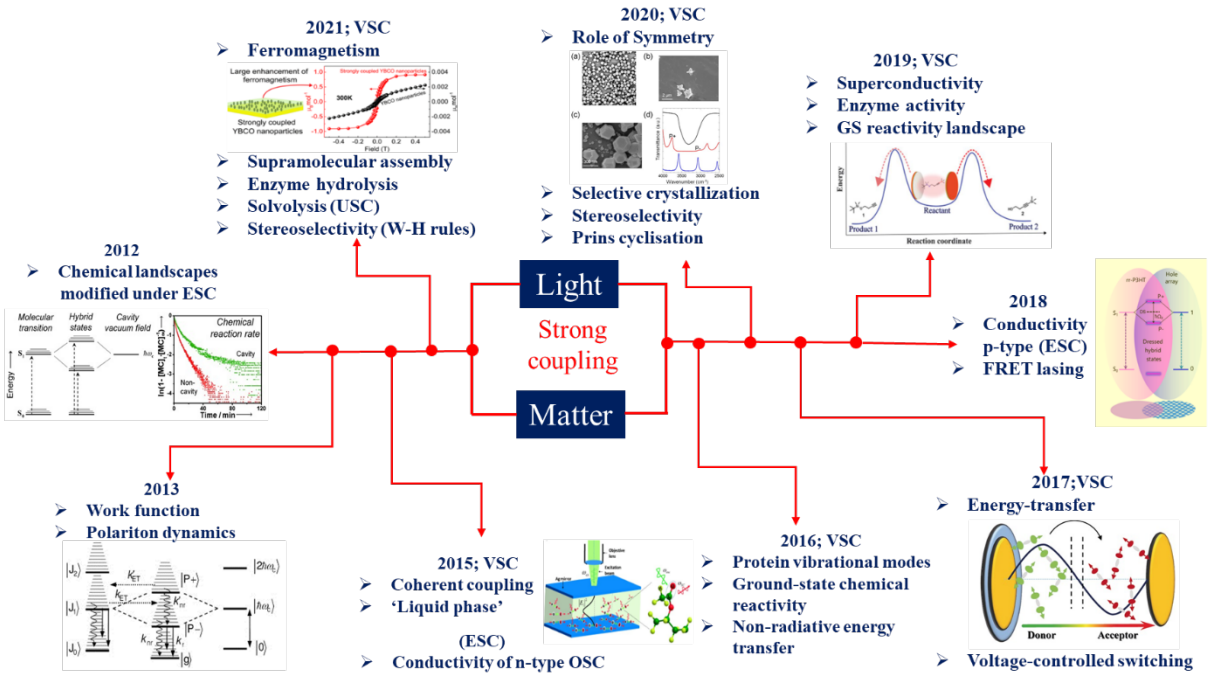

Figure 1.2. Highlights the consequences of light-matter strong coupling in materials investigated since 2010.

theoretically confirmed very recently.[74] Such results highlighted the potential of VSC for controlling chemical reactivity and triggered many other studies on a variety of reactions such as Prins cyclization,[75] hydrolysis,[76] solvolysis,[19,77] enzymatic [78,79] and charge transfer reactions.[80] The solvolysis of PNPA in ethyl acetate was the first example of cooperative strong coupling. When direct coupling of solute is not possible due to its limited solubility, it is possible to couple them *via* cooperative effect if the solute and the selected solvent have overlapping vibrational bands and thereby also influence the chemical reactivity.[81] Vergauwe *et al.* reported retardation in enzymatic activity of protease pepsin by a factor of 4.5 when O-H stretch of water is strongly coupled, but no effect was observed for the bending mode of water under VSC.[79] On the contrary, when the vibrational mode of a different enzyme, α-chymotrypsin, was cooperatively coupled through the O-H stretching mode of water, the kinetics increased *via* the perturbation of the proton-transfer process under VSC.[78] Recent

reports have shown that VSC also modifies vibrational energy transfer which might play a role in cavity chemistry.[82,83]

The large thermodynamic changes induced by VSC came as a surprise. After all the Rabi splitting in VSC is typically on the order of k_BT, i.e. 25 meV (ca. 2.5 kJ/mole) while the modification of the transition state energies is typically 10 times larger. Hence there must be other factors at play such as symmetry which is known to have a fundamental role in chemical reactivity. Indeed Pang *et al*. showed that the free-energy of mesitylene-iodine charge transfer complexation reaction is lowered or raised, depending only on the symmetry of the vibrational band coupled to the optical mode (Figure 1.3 a).[80] As they concluded, it appears that the strong coupling process with the cavity mode modifies the symmetry of the vibropolaritonic mode relative to the original vibrational band. Another work that emphasized the importance of vibrational bands' symmetry was the study of molecules that obey Woodward-Hoffman's rules (Figure 1.3 b). The typical expectation of stereoselectivity in the resultant products of electrocyclic ring-opening of cyclobutene derivative was altered under VSC.[84]

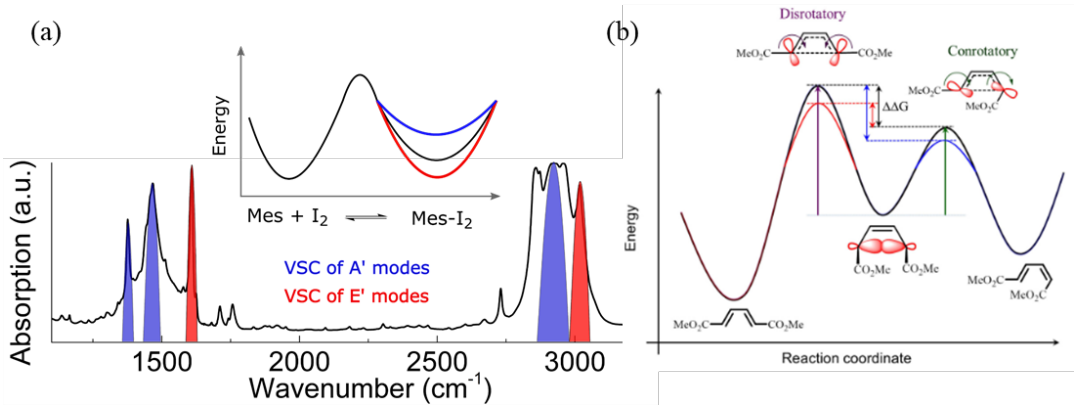

Figure 1.3. Significance of symmetry in light-matter strong coupling (a) Chemical landscape of mesitylene-iodine charge transfer complex modified with respect to the symmetry of vibrational bands being strongly coupled. (b) Energy level diagram for con- and dis-rotatory opening of electrocyclic reactions. Figures reproduced from refs. [80,84]

In addition to the VSC effects on chemical reactions, recent studies demonstrate that intermolecular interactions can also by modified by VSC of the solvent, the solute or both through the cooperative process. [58–60] Hirai and his colleagues investigated pseudo-polymorphism of ZIF metal-organic frameworks in resonant optical resonators.[58] They observed that Cubo-octahedral-shaped ZIF-8 crystals are 'selectively crystallized' when O-H stretch of water is strongly coupled, instead of both cross-hair star-shaped ZIF-L and Cubo octahedral ZIF-8 being formed in non-cavity. In yet other studies, we found that the morphology of supramolecular assemblies could be modified when the system was under cooperative VSC.[59,60] we will present these results in the fourth Chapter.

There are many aspects of strong coupling that are not still understood, most notably that in order to see an effect on a property, the material must be coupled at k//=0, e.g. at normal incidence for a Fabry-Perot cavity. It points to the challenges of modeling strongly coupled systems, especially when they involve the complexity of chemical reactivity. Many theoretical groups have taken the challenge to improve the model from a fundamental perspective. [74,85–95] Recent studies using ab-initio QED calculations were able to reproduce experimental results related to silyl deprotection reaction under VSC.[74] Also, other theoretical studies were successful in proving that intermolecular interactions are indeed modified under ESC.[85,89] Ab-initio QED studies look promising in terms of understanding experiments, and predicting the patterns and fundamental rules in results.[85,93,94] Nevertheless, more sophisticated theoretical descriptions are required to fully understand the mechanism in coupled systems, and to be able to predict the outcome of strong coupling on a given chemical reaction. In the next Chapter, we will describe Jaynes-Cummings model – the simplest theoretical model for describing light-matter strong coupling before presenting the models used to describe the properties of organic semiconductors.

2.

THEORETICAL MODELS

Since the thesis work involves both strong coupling and organic semiconductors, we will introduce, in this Chapter, the corresponding theoretical models. We start with the Jaynes-Cummings model (Figure 2.1 a) which yields the fundamental features of strong coupling. This section is followed by the comparison of two opposing conductivity models of organic semiconductors, hopping and band regimes, briefly discussing how different parameters determine the mobility of organic systems. This Chapter is then concluded by discussing the recent reports on the enhancement of conductivity of OSCs under light-matter strong coupling.

2.1. Jaynes-Cummings model for a two-level system

The simplest model describing light-matter strong coupling- the Jaynes-Cummings model, was developed by Fred Cummings and Edwin Jaynes in 1963. This model describes the interaction of an atom approximated as a two-level system, with a single mode of a quantized electromagnetic field. [96] Following this model, different theoretical models have been defined, such as the Tavis-Cummings[97] (Figure 2.1 b), in which a single mode of the quantized electromagnetic field is coupled to a collection of multiple identical atoms. *N* two-level atoms

interact strongly with the cavity resonance to give upper and lower polaritonic states in addition to *N-1* dark states. Since organic molecules have rotational and vibrational degrees of

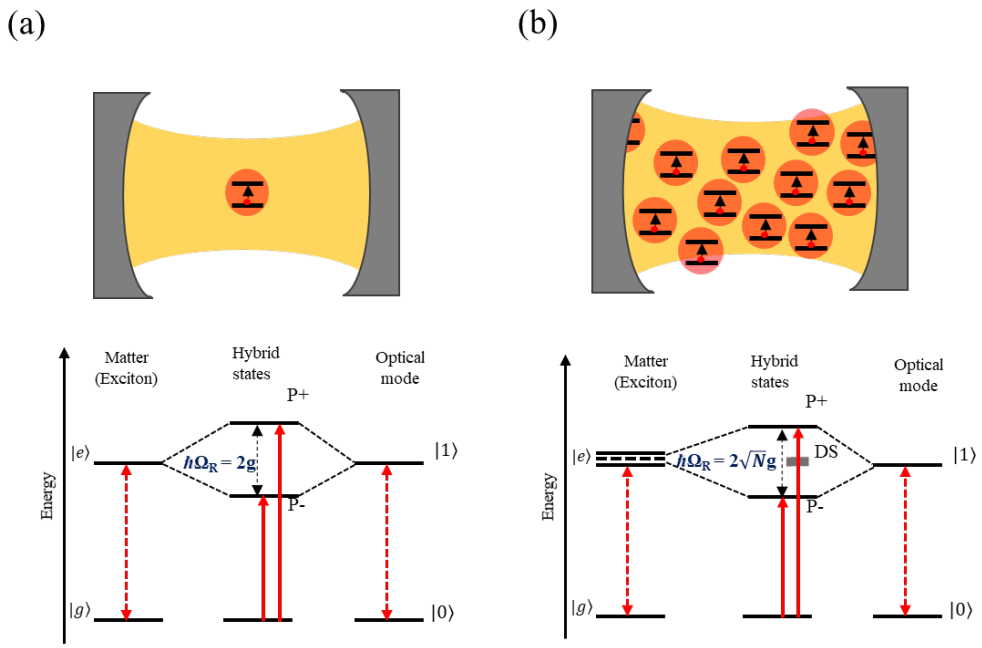

Figure 2.1. (a) Schematics of Jaynes-Cumming's model describing the interaction of a two-level emitter to a single quantized electromagnetic mode, and (c) Tavis-Cummings model describing the interaction of *N* two-level emitters to a single quantized EM mode.

freedom in addition to the electronic transitions, approximating them as two-level systems cannot predict the effect of strong coupling on their properties. Although several theoretical groups have modelled rovibrational degrees of freedom, [98–101] as discussed in the previous Chapter, more complicated theoretical calculations are required to gain further insight into the coupled systems and the origin of the modified properties.

Using the formalism found in references, [96,102] we detail below the simplest model of light-matter coupling- the Jaynes-Cummings model and its consequences.

Following is the corresponding Jaynes-Cummings Hamiltonian:

$$\hat{H}_{JC} = \hat{H}_{atom} + \hat{H}_{field} + \hat{H}_{in} \qquad (2.1)$$

The atom Hamiltonian $\hat{H}_{atom}$ is described with a two-dimensional state space having two energy eigenstates and energy eigenvalues: excited state, $|e\rangle$, E_e and ground state, $|g\rangle$, E_g

$$|e\rangle = \begin{pmatrix}1\\0\end{pmatrix}, \quad |\mathrm{g}\rangle = \begin{pmatrix}0\\1\end{pmatrix}, \qquad (2.2)$$

$\hat{\sigma}_+$ is the operator defining the transition from $|g\rangle$ to $|e\rangle$ and $\hat{\sigma}_-$ for the reverse process, the Hermitian Pauli operator $\hat{\sigma}_z$ defines the energies of the states,

$$\hat{\sigma}_+ = |\mathrm{g}\rangle\langle e| = \begin{pmatrix}0 & 1\\0 & 0\end{pmatrix} \qquad (2.3)$$

$$\hat{\sigma}_- = |\mathrm{e}\rangle\langle g| = \begin{pmatrix}0 & 0\\1 & 0\end{pmatrix} \qquad (2.4)$$

$$\hat{\sigma}_z = |\mathrm{e}\rangle\langle e| - |\mathrm{g}\rangle\langle g| = \begin{pmatrix}1 & 1\\0 & -1\end{pmatrix} \qquad (2.5)$$

Therefore, the Hamiltonian for an atom is

$$\hat{H}_{atom} = \frac{1}{2}\hbar\omega_0\hat{\sigma}_z \qquad (2.6)$$

Hamiltonian of the quantized field, $\hat{H}_{field}$ is given by

$$\hat{H}_{field} = \hbar\omega\hat{\mathrm{a}}^\dagger\hat{\mathrm{a}} \qquad (2.7)$$

where $\hat{\mathrm{a}}^\dagger$ and $\hat{\mathrm{a}}$ are the creation and the annihilation operator for creating or annihilating photons.

The Hamiltonian defining the interaction between the dipole moment of an atom, $\hat{d}$, and quantized electric field operator $\hat{E}(t)$ is given by:

. $\hat{H}_{in} = -\hat{d}.\hat{E}(t)$ with $\hat{E}(t) = \hat{E}_0\,(\hat{\mathrm{a}} + \hat{\mathrm{a}}^\dagger)$

Since counter-rotating terms oscillate at a very high frequency $\omega + \omega_0$, their effect is negligible. Therefore, under the RWA, counter-rotating terms $(\hat{a}^\dagger\hat{\sigma}_+ + \hat{a}\hat{\sigma}_-)$ cancel out, and interaction Hamiltonian can be given as:

$$H_{in} = -i\frac{\hbar\Omega_R}{2}(\hat{a}\hat{\sigma}_+ - \hat{a}^\dagger\hat{\sigma}_-) \qquad (2.8)$$

where the first term in $(\hat{a}\hat{\sigma}_+ - \hat{a}^\dagger\hat{\sigma}_-)$ describes the annihilation of a photon and transition of the atom to the excited state, while the second term describes the opposite process, Rabi frequency, Ω_R is associated to the oscillation frequency to the coupling strength and the coupling constant, g, is given by

$$g = \frac{\Omega_R}{2}$$

Therefore, Jaynes-Cummings Hamiltonian within the RWA can be written as:

$$\hat{H}_{JC} = \frac{1}{2}\hbar\omega_0\hat{\sigma}_z + \hbar\omega\hat{a}^\dagger\hat{a} - i\frac{\hbar\Omega_R}{2}(\hat{a}\hat{\sigma}_+ + \hat{a}^\dagger\hat{\sigma}_-) \quad (2.9)$$

Introducing the parameter, $\Delta = \omega - \omega_0$, to measure the effect of detuning of cavity mode with respect to the transition in the atom, the Hamiltonian becomes

$$\hat{H}_{JC} = \frac{\hbar(\omega+\omega_0)}{2}\begin{pmatrix}1 & 0\\ 0 & 1\end{pmatrix} + \frac{1}{2}\begin{pmatrix}-\Delta & -i\Omega_R\\ i\Omega_R & \Delta\end{pmatrix} \qquad (2.10)$$

We get the new energy eigenvalues,

$$E_\pm = \frac{\hbar(\omega+\omega_0)}{2} \pm \frac{1}{2}\left(\sqrt{\Delta^2+\Omega_R^2}\right) \qquad (2.11)$$

The dispersion of the eigenstates corresponding to the above eigenvalues leads to the anti-crossing behavior of the following polaritonic states $|P_\pm\rangle$:

$$|P_+\rangle = \cos\theta\,|e\rangle|0\rangle + i\sin\theta\,|g\rangle|1\rangle \qquad (2.12)$$

$$|P_-\rangle = \sin\theta\,|e\rangle|0\rangle - i\cos\theta\,|g\rangle|1\rangle \qquad (2.13)$$

in which angle θ is defined as

$$\Omega_R \tan(2\theta) = -\frac{\Omega_R}{\Delta} \quad (2.14)$$

At Δ = 0, the angle θ is calculated as $\pi/4$, the entanglement between the polaritonic states is the maximum and is given by

$$|P_{ON,+}\rangle = \frac{1}{\sqrt{2}}(|e\rangle|0\rangle + i|g\rangle|1\rangle) \quad (2.15)$$

$$|P_{ON,-}\rangle = \frac{1}{\sqrt{2}}(|e\rangle|0\rangle - i|g\rangle|1\rangle) \quad (2.16)$$

At this tuning, polaritonic states have 50 % of each photonic and bosonic character, and the wavefunction is localized over the mode volume.

In the following sub-section, we will compare different regimes of light-matter coupling.

2.1.1 Different regimes of light-matter coupling

Light-matter coupling can be classified into the following regimes based on five different time scales: cavity and molecular decay rates (κ and γ), the coupling strength between the dipole interactions of matter and the resonant optical mode (g), and the frequencies of molecular transition and cavity mode (ω_0 and ω).

1. *Weak coupling regime*: Also called as 'perturbative regime', the rate of dissipative processes of the material (κ) and decay rate of the cavity (γ) dominate the coupling frequency. Therefore, Rabi splitting (Ω_R),

$$\frac{\hbar\Omega_R}{2} = g < \kappa, \gamma, \omega_0, \omega \quad (2.17)$$

Due to this, only radiative properties such as spontaneous emission rate and Lamb shift are altered. Fermi's golden rule holds for this regime. As already described in the previous

section, the Purcell effect falls in this category, wherein spontaneous emission rate can either be enhanced or inhibited due to vacuum coupling in a resonant structure, demonstrated years ago by Drexhage.[31,33] The RWA and Jaynes-Cummings Hamiltonian are valid in this regime.

2. *Strong coupling regime*: In this regime, the coupling constant, g dominates the cavity and material decay rates (κ and γ); the Rabi splitting is such that:

$$\kappa, \gamma << \frac{\hbar\Omega_R}{2} = g << \omega_0, \omega$$

which implies that the photon can be absorbed and re-emitted before leaking from the cavity. In other words, for a system to be in this regime, following criterion needs to be satisfied:

$$\hbar\Omega_R > (\Gamma_m + \Gamma_c)/2,$$

where Γ_m and Γ_c are the full width at half maximums (FWHM) of molecular and optical modes, respectively,[103,104] i.e., Rabi splitting needs to be larger than the FWHM of optical and molecular absorption modes (Figure 2.2 e and f).

Fermi's golden rule is no longer valid here, but the Jaynes-Cummings model can be used. Hybrid light-matter states are formed, in addition to the bright states: P+ and P-, dark states (DS) are also formed (as shown in Figure 2.2 d), which does not necessarily exist between the bright states.[105]

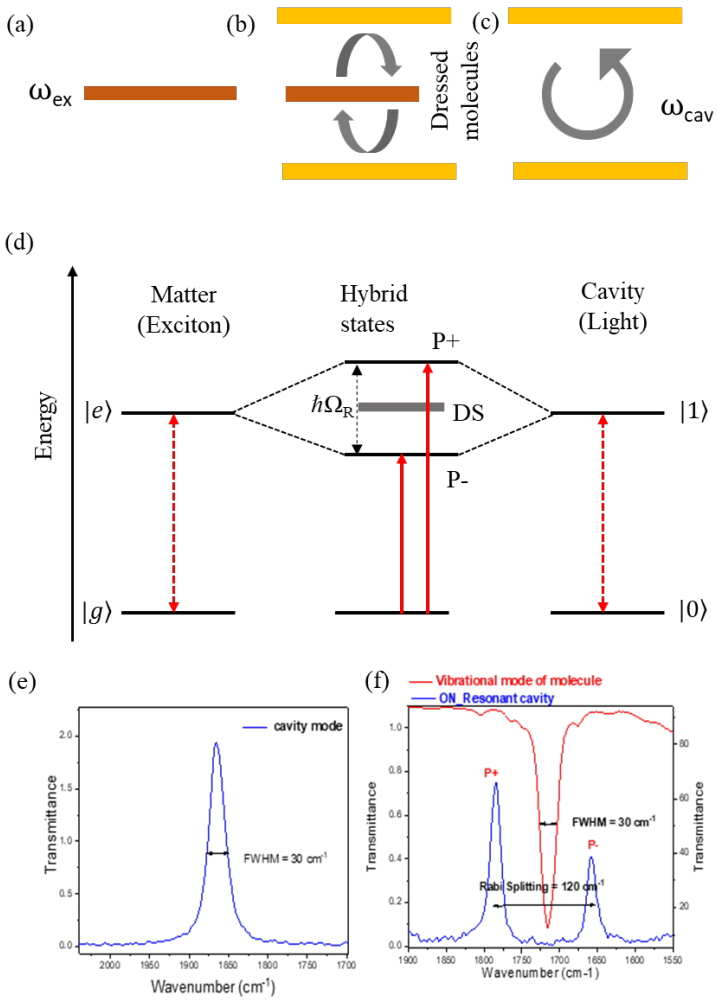

Figure 2.2. When an (a) exciton and (c) optical cavity mode have frequencies ω_{ex} and ω_{cav} that come in resonance, (b,d) exchange of energy takes place and leads to the dressing of the molecules with EM vacuum field inside the cavity leading to the generation of hybrid light-matter states. In addition to the bright states (P+ and P-), dark states (DS) are also formed. € shows the optical mode of full width at half maximum (FWHM), and (f) shows the vibrational mode of cyclohexanone with carbonyl stretch at 1720 cm^{-1}, coupled to the optical mode, leading to the formation vibro-polaritonic states. Note that the Rabi splitting is larger than the FWHM of both molecular transition and the optical mode.

The energy difference between the upper and lower polaritonic states is given by:

$$\hbar\Omega_R = \sqrt{4g^2 - (\kappa - \gamma)^2} \qquad (2.18)$$

when $g \gg \kappa$, the Rabi splitting is given as:

$$\hbar\Omega_R = 2g = 2d.E_0 = 2d\sqrt{\frac{\hbar\omega}{2\varepsilon_0 V}} \times \sqrt{n_{ph}+1} \qquad (2.19)$$

Such a coupling is possible even in the dark ($n_{ph} = 0$) due to the coupling of matter with the zero-point vacuum fluctuations. $\hbar\Omega_R$ is dependent on the number N of molecules coupled to the optical mode,

$$\hbar\Omega_R \, \alpha \, \sqrt{\frac{N}{\nu}}$$

For an optical Fabry-Perot cavity, dispersion of light-matter hybrid states, or polaritonic states, is given by:

$$k_{//} = \frac{2\pi}{\lambda} sin\theta \qquad (2.20)$$

where λ is the peak wavelength and θ is the angle of incidence. In our experiments, the system is said to be in resonance when strong coupling occurs at normal incidence ($k_{//} = 0$). At larger values of $k_{//}$, P+ behaves more like photons and P− like materials, and vice-versa for lower $k_{//}$ values.

This thesis focuses on the results obtained in the strong coupling regime as measured at $k_{//} = 0$.

3. *Ultra-Strong coupling regime*: Due to the high values of coupling constant, g, RWA breaks down as the counter-rotating term is no more negligible, and the Jaynes-Cummings model does not hold in this regime, where.

$$\frac{\hbar\Omega_R}{2} = g \lesssim \omega_0,$$

In this regime, the ground state is shifted and the material properties are expected to be modified.[106] The ground state acquires a photonic content and thereby the polaritonic

qualities such as delocalization under collective coupling. In Chapter 3, we will show an example of this for the conductivity of a p-type organic semiconductor under ultra-strong coupling.

2.2 ORGANIC SEMICONDUCTORS

Conventional inorganic semiconductors such as Si have been dominant since the first transistors were made with such materials in the 1950's. Organic semiconductors (OSC) were first reported in the 1970's and were seen as very promising since they offered the possibility of large-scale synthesis, low cost, electronic tuning, room temperature stability, and many other advantages such as mechanical flexibility. They are typically carbon-based π −conjugated systems, and have potential applications in optoelectronic and mechatronic devices such as solar cells, transistors, sensors, thermoelectrics, light-emitting

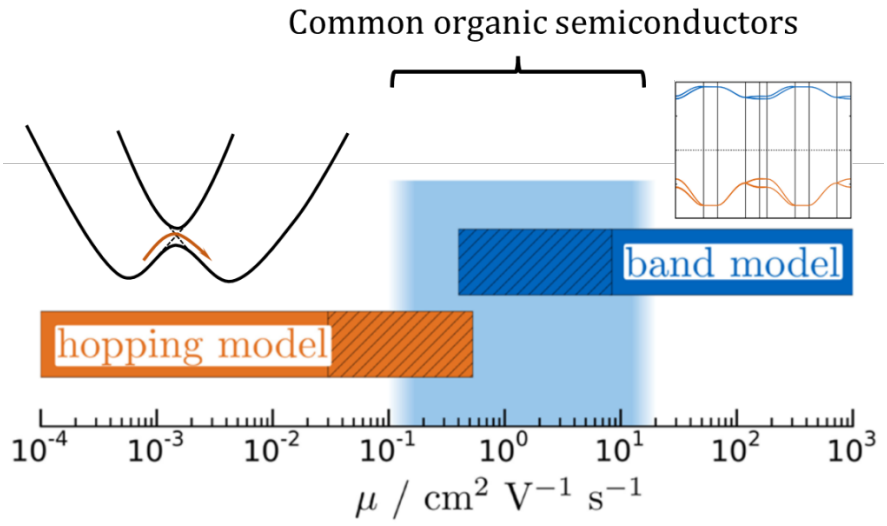

Figure 2.3. Schematic illustration of ranges of organic semiconductors theoretically described by hopping or band transport regimes. Reproduced from ref [107]

diodes, and neuromorphic devices. The biggest limiting factor in the use of OSC has been their low carrier mobility compared to inorganic semiconductors. The first organic field-effect transistor (OFET), which incorporated polythiophene as a semiconductor, reported a charge carrier mobility of $10^{-5}\ cm^2V^{-1}s^{-1}$.[108] The optimization of device architecture and synthesis of novel conducting organic systems has improved the charge carrier mobility to reach values of $11\ cm^2V^{-1}s^{-1}$ and $40\ cm^2V^{-1}s^{-1}$ for electron and hole mobilities respectively. [109,110] The conduction mechanism in organic semiconductors are typically described through hopping and band transport models, and we will briefly discuss both models in the section below.

2.2.1 Transport regimes in organic semiconductors: Hopping and Band models

Based on the localization of charge carriers, transport mechanisms can be explained through three regimes: two opposing limiting mode–s - hopping[111] and band regimes[112,113], and an intermediate mixed regime. The hopping model assumes charge carriers to be localized at specific sites, which then jump between the sites. This model is applicable within the constraints of high reorganization energy and small electronic coupling, where the activation barrier between the localized states exists. In contrast, the band transport theory is valid for organic semiconductors with delocalized charge carriers. The mean free path of charge carriers is then longer than the lattice spacing, which is the case for pure organic crystals with large electronic coupling.[107,114] However, in real systems, charge transport in molecular organic semiconductors follows the characteristics of the mixture of both regimes and is therefore described with the intermediate regime model.

2.2.1 Hopping model

Spatial and energetic disorders in organic solids result in the localization of charge carriers. In such organic molecules, charge transport occurs via a hopping process of localized charge carriers from one specific site to another. Lattice distortion due to localization of charges in organic semiconductors leads to the downward shift of the conduction band (LUMO) and upward shift ($\Delta\epsilon$) of the valence band (HOMO). When this change in ionization potential is larger than distortion energy ($\Delta\epsilon > E_{dis}$), hopping model dominates over band transport- leading to the formation of polarons.[115] Polarons are the $\pi -$ radical ions (radical cations or anions, with spin $^1/_2$), stabilized by polarizing the medium surrounding it while polaronic states are the localized states formed in the bandgap. Polaron hopping rate depends on the spatial overlap between electronic wavefunctions of two sites. Two significant parameters, that determine the exchange rate and thus the charge carrier mobility, are transfer integral (t) and reorganization energy (λ).[116] Transfer integral quantifies the electronic coupling between neighboring molecules and depends on intermolecular interactions, molecular packing, and $\pi - \pi$ stacking distance, while reorganization energy incorporates both inner (short-range) and outer (long-range) sphere contributions. Charge transfer leads to the deformation of molecules, incorporated as inner sphere contributions whereas external contributions results from the changes in the surrounding medium due to charge transfer.[107] The rate of electron transfer between the donor and acceptor states is given by,

$$k_{et} = \frac{4\pi^2}{h} t^2 \frac{1}{\sqrt{4\pi\lambda RT}} e^{-\lambda/4RT} \qquad (2.21)$$

As can be seen from equation (2.21), large transfer integral (t) and small reorganization energy (λ) result in faster charge transfer rates (k_{et}), which is required for high hopping carrier mobility in organic semiconductors.

2.2.2 Band theory

In the band transport regime, we assume that the charge carriers are delocalized in the carrier bands. Holes and electrons reside in the valence band maximum and conduction band minimum, respectively. The carrier mobility is given by:

$$\mu = \frac{\bar{\tau}}{m_e} \qquad (2.22)$$

where m_e is the effective mass along the direction of transport and $\bar{\tau}$ is the average time between the scattering events for charge carriers. m_e can be determined from the parabolic fit of carrier bands and is given by:

$$m_e = \frac{\hbar^2}{2ta^2} \qquad (2.23)$$

where t is the transfer integral and a is the intermolecular distance. Organic semiconductors are in this regime when the electron-phonon coupling is small, i.e., when the mean free path of the charge carrier is larger than the intermolecular spacing, which is observed only at relatively

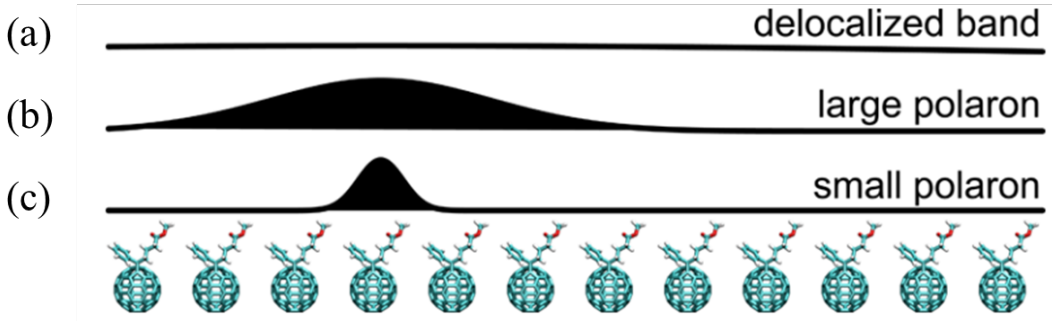

Figure 2.4. Schematic illustration of localization of charge carriers in organic solids. (a) Band model- fully delocalized band state (b) Intermediate regime– large polaron delocalized over many molecular sites. (c) Hopping model– a small polaron is localized on a single molecular site. Reproduced from ref [107]

low temperatures. Since the number of scattering events increase with the increase in temperature, $\bar{\tau}$ decreases and therefore, mobility is inversely proportional to temperature.

In most organic semiconductors, charge carriers experience both partial delocalization in a band all the while encountering traps at specific sites. Hence charge carrier mechanisms in most organic crystals cannot be explained solely by either the hopping or band transport idealized models. Therefore, typically the 'intermediate transport regime' (a combination of both models) is employed to study charge transport in organic solids.[107] While the theoretical model is beyond the scope of this thesis, the regime between polaron hopping and band models – has charge carriers delocalized over multiple molecular units. Since such large polarons (Figure 2.4 b) are delocalized, the polaronic states can be described as bands and the propagation of these polarons are similar to the charge propagation in band theory.[112]

2.3. Effect of strong coupling on organic semiconductors

Although low mobility and large disorder in organic semiconductors limit their applications in optoelectronics, the delocalized nature of polaritonic states and their coherence have been shown to provide a pathway to improve transport properties[3–15]. The large molecular transition dipole moments make them better candidates for strong coupling over inorganic solids. In 2015, George *et al*. reported that the conductivity of an n-type organic semiconductor can be enhanced by an order of magnitude under ESC with plasmonic modes leading to the splitting of the conduction band into hybrid light-matter states.[4] To investigate whether electronic strong coupling also affects the conductivity of a p-type organic semiconductor wherein charge transport occurs in the valence band, we have studied the transport properties, both conductivity and photoconductivity, of regio-regular poly-(3-hexylthiophene) (*rr*-P3HT)

as reported in Chapter 3. It should be noted that another study reporting changes in photoconductivity of a p-type organic semiconductor under ESC appeared after submission of our paper.[9]

Since intermolecular and intramolecular lattice vibrations have a crucial role in determining charge transport mobility of OSCs,[117–119] we have investigated the effect of VSC on the conductivity of highly conducting polymer: poly(3,4-ethylenedioxythiophene) polystyrene sulfonate (*PEDOT: PSS*) by coupling one of its vibrational bands to the plasmonic resonance. With the help of theoretical calculations done by Prof. Luis Martin-Moreno and his colleagues, and the fabrication done by Prof. Sang Hyun-Oh's group, we have optimized the plasmonic structures with resonances having significantly improved Q (quality) factors reaching what is necessary for achieving VSC in the mid-IR. We see an enhancement in conductivity by a factor of 12 under coupled condition. The results will be discussed in Chapter 5.

3.

CONDUCTIVITY OF A P-TYPE ORGANIC SEMICONDUCTORS UNDER ELECTRONIC STRONG COUPLING

3.1 Introduction

As just discussed, in 2015, George *et al.* reported that the transport properties of an n-type organic semiconductors can be improved by strongly coupling the electronic transition to the plasmonic modes. An associated theoretical model showed that such an enhancement in the mobility of n-type organic molecules in the strong coupling regime is due to the extended coherence and delocalized character of the collective states, in particular the dark states, generated from the hybridization with the vacuum field.[4] However, the effect of electronic strong coupling on the conductivity of p-type organic semiconductors wherein charge (holes are majority carriers) transport occurs in the valence band, had not been investigated. According to the theoretical simulations reported in 2005, the quantum properties of ground states are also modified in ultra-strong coupling regime because they acquire photonic character.[106] To investigate the effect of ESC on the transport properties of p-type organic

semiconductors, we have studied the conducting polymer regio-regular poly(3-hexylthiophene) (*rr*-P3HT). Since photoconductivity plays a key role in many applications such as photovoltaics and photodetectors,[120,121] we have also studied photoconductivity under ESC. For our study, the electronic transition of P3HT is strongly coupled to the plasmonic resonance of the hole arrays wherein optical mode can be tuned by changing the periodicity (P) of arrays. Large parts of this Chapter are taken from the already published work[70].

3.2 Experimental details

3.2.1 System under study

The organic semiconductor rr-P3HT (Figure 3.1 a) was synthesized and purified as described in the literature,[122] it was then dissolved in trichloroethylene by Soxhlet extraction method and spin-coated on the hole arrays, yielding *ca.* 85 nm thick films.

3.2.2 Two-terminal device with nanohole arrays

All the 2-terminal electrodes were realized on a glass substrate BK7 (25×25 mm) after standard cleaning procedures with Hellmanex™ III solution (1.0% solution in milliQ water) in a 35 kHz sonication bath, then rinsed with water and sonicated for 1 h in (spectroscopically pure) ethanol. The glass substrates were then dried in an oven covered with Aluminium foil. 100 nm thick Ag electrodes were fabricated using a metallic cross mask containing 12 fingers (approx. 50 μm width) in an electron beam evaporator (Plassys ME 300) at optimized working pressure ($\sim 10^{-6}$ mbar) and deposition rates (~ 2 nm s^{-1}). Plasmonic hole arrays were generated by the NPVE software program and milled using a Carl Zeiss Auriga FIB system. 1.0 wt% of

rr-P3HT and PDI solutions were freshly prepared by dissolving the molecules in spectroscopic grade trichloroethylene (Soxhlet extraction) and anhydrous chloroform respectively at ambient conditions and spin-coating onto the electrodes at 1000 r.p.m., to achieve 85 nm-thick films. The reddish, smooth rr-P3HT and PDI thin-films were completely dried and annealed on a hot plate above the glass transition temperature. A passive layer of PVA was spin-coated (~200 nm) further to protect the active layer to avoid direct exposure to air and moisture. For a test experiment, to introduce an insulating layer in between the metal hole array and organic semiconductor, 20 nm SiO_x was sputtered on top of the metal hole array by using magnetron sputter under reduced pressure (10 mTorr) at 200 W for 50 sec. On top of the sputtered SiO_x, organic semiconductor and PVA layer were spin coated as explained above.

3.2.3 *Electrical characterization of the device*

The electrical characterization of the 2-terminal device was carried out by means of a Cascade Microtech MPS-150 probe station equipped with micro-positioners to contact the electrode pads. Both the dark current and photoconductivity I–V characteristics are recorded by means of a Keithley 2636B source meter interfaced with Labtracer 2.0 software. Photocurrent generation was tested under white light cw illumination and with a super-continuum ps pulsed laser (NKT Photonics) with a nominal power of 100 mW to 200 mW, with variable wavelength (500-800 nm; 10 nm FWHM) provided by a SuperK tunable single line filter. The output of the FC/PC fiber was directed to the center of the electrode covering a spot size of 2 mm in diameter.

3.3 Results and discussions

The conductivity and the photoconductivity of the rr-P3HT were studied on Ag nano-hole arrays (having hexagonal periodicity) between drain and source electrodes, using the same approach as in ref [4]. Ag was chosen for its capacity to sustain low-loss surface plasmon modes in the wavelength range of interest while still providing good injection capacity for the electrical measurements.[4] As explained previously, the hexagonal hole arrays were milled with a Zeiss Auriga dual beam FIB/SEM in a 100 nm thick Ag film and the period P of the holes were varied (from 320 nm to 560 nm) in such a way that the plasmonic resonances are in the

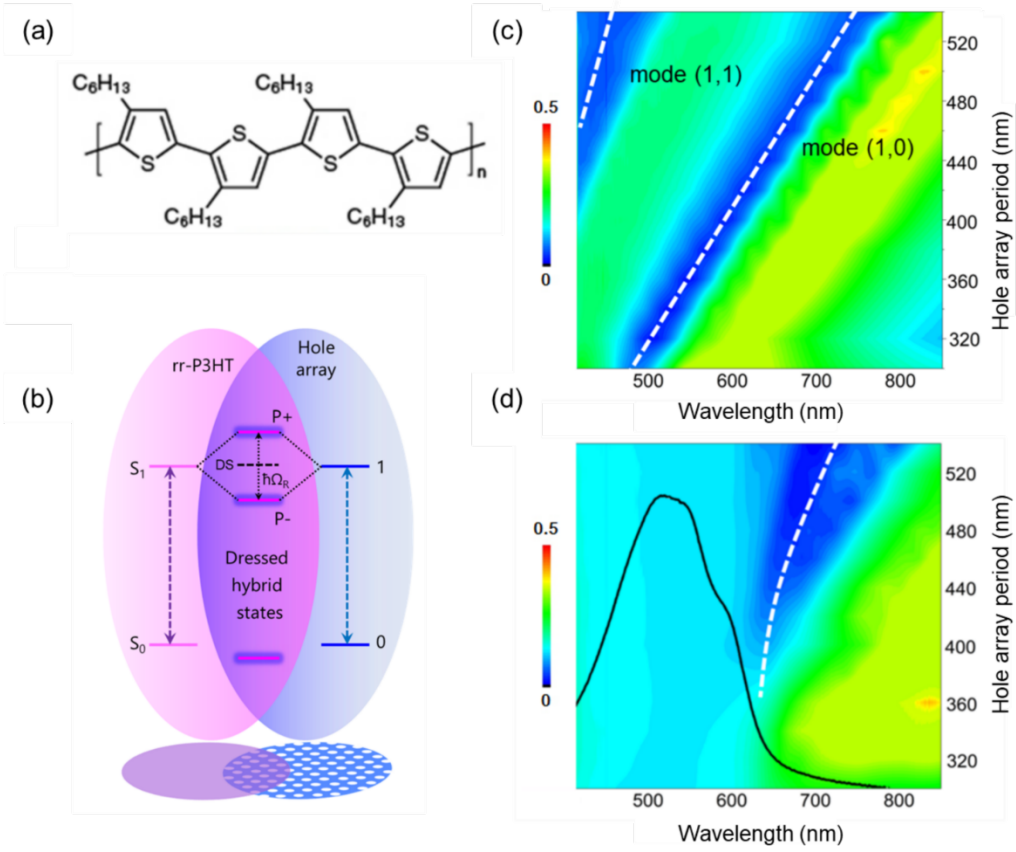

Figure 3.1. Strong coupling between surface plasmon and organic semiconductor: (a) Molecular structure of the *p-type* semiconductor rr-P3HT polymer. (b), Schematic representation of ultra-strong coupling between Ag hole array and rr-P3HT film. Contour image of transmission spectra of the hole arrays in the (c) absence and (d) presence of rr-P3HT (black curve shows the molecular absorption) as a function of period ranging from 320 nm to 540 nm

(dashed white lines are guidelines to eyes) (x-axis data is not shown below 415 nm, the lower wavelength limit of our optical spectrophotometer detection). Figure reproduced from [70].

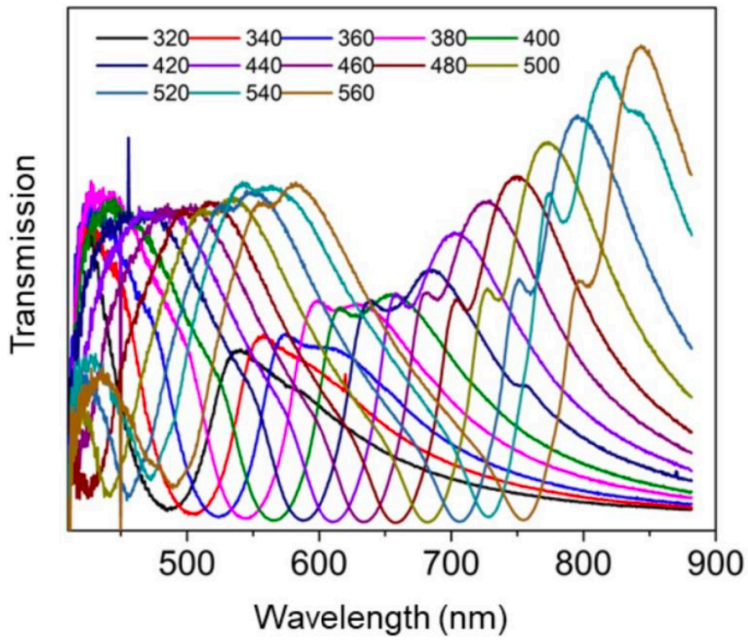

Figure 3.2. Surface plasmon resonance of hole arrays, periodicty varied from 320 to 560 nm. Figure reproduced from [70].

same range as the first absorption bands of the semiconductor. Surface plasmon resonances (λ_{sp}) of hexagonal hole arrays having different periodicity (P) are given by:

$$\lambda_{sp} = \frac{P\frac{\sqrt{3}}{2}}{\sqrt{i^2 + j^2 + ij}}\sqrt{\frac{\varepsilon_m \varepsilon_d}{\varepsilon_m + \varepsilon_d}} \qquad (3.1)$$

where, i and j are integers; ε_m and ε_d are the refractive index of metal and dielectric material respectively.[123] The different modes of the hole array is denoted by the indices i and j as (i,j). Thus Ag hole arrays of given periodicity (320 nm to 560 nm, Figure 3.2) exhibit corresponding (1,0) and (1,1) surface plasmon modes in the visible region, which can be tuned to the absorption band of the semiconductors. The hole arrays spin-coated with rr-P3HT was then covered with a 200 nm PVA (poly vinyl alcohol) film.

The strong coupling regime was verified by measuring their transmission spectra for different hole array periods P and comparing them with the bare hole arrays (*i.e.* without absorber) (Figure 3.1 c and d). We observe a mode bending of the lower polaritonic branch (P-) in the presence of organic semiconductor. The upper polaritonic branch (P+) is in the UV

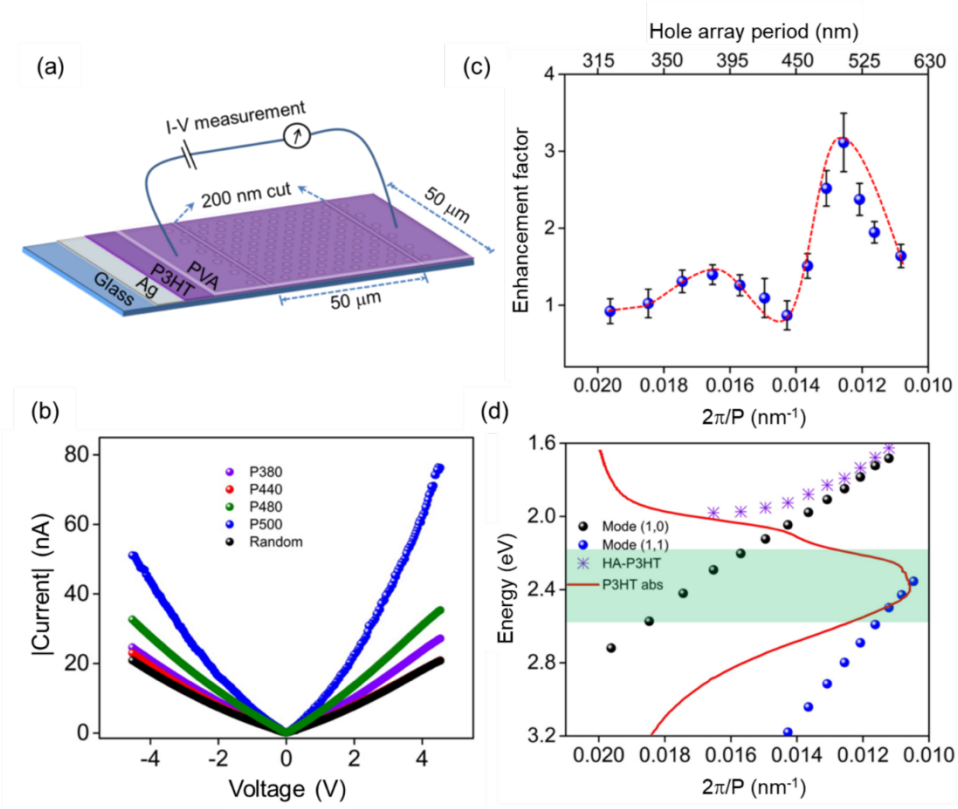

Figure 3.3. Current-Voltage measurement: (a) Schematic representation of the set-up used to perform conductivity measurement. (b) Current-voltage (I-V) curves of the rr-P3HT samples as a function of the period P of the hole arrays. (c) Conductivity enhancement with respect to the in-plane momentum of hole arrays (top axis shows corresponding hole array period in nm). Blue dots show the average value of three different experiments and the error bars show the standard deviation. Red dashed line is a guide to the eye. (d) The conductivity enhancement observed in c, correspond to the intersection of the rr-P3HT molecular absorbance (red line) and the surface plasmon resonance for the (1,0; black dots) and (1,1; blue dots) modes of hexagonal hole arrays in Ag; The violet

stars show the lower polaritonic band. The broad absorption region of rr-P3HT is highlighted. Figure reproduced from [70].

region and cannot be detected with optical microscope with which the spectra were taken. The resulting Rabi splitting are estimated to be *ca.* 0.6 eV for rr-P3HT corresponding to 27% of the transition energy. Such large Rabi-splitting indicates that the system is in the ultra-strong coupling regime where all the states of the system are modified with significant consequences as we will discuss further down.

The conductivity of the samples was then characterized using the setup schematically shown in Figure 3.3 a. The I-V (current-voltage) curves of the various samples were then recorded as shown in Figure 3.3 b as a function of the hole period over a voltage range (-5 to 5 V). From the measured I-V curve, current enhancement factor was calculated by comparing the current in the periodic hole array systems with that of a random hole array. Figure 3.3 c plots the current enhancement factor at ± 5V as a function of $2\pi/P$ for dark current of rr-P3HT coated hole arrays with respect to a random array. The current enhancement factor peaks when the absorption maximum of rr-P3HT crosses the (1,0) and (1,1) modes of the hexagonal plasmonic array (Figure 3.3 d) and undergoes strong coupling. In other words, this occurs only when the plasmonic array is in resonance with the rr-P3HT absorption. The small differences, 3% and 8%, between the crossings of the (1,0) and (1,1) modes with the rr-P3HT absorption (Fig. 3.3 d) and the current peaks (Fig. 3.3 c) is well within experimental error when considering the following. The surface plasmon mode position in the bare Ag hole arrays can only be calculated in the absence of the absorber. Obviously, the refractive index and therefore the surface plasmon modes will be modified by the presence of the absorber even in the absence of strong coupling. In addition, the rr-P3HT absorption is so broad that it overlaps with both modes simultaneously. When compared to the conductivity on a random hole array, *rr*-P3HT on resonance hole array (P = 500 nm; $k_x = 0.0126$ nm^{-1}) exhibits an enhancement factor of ~3

for the dark current measurement. This enhancement is smaller than the maximum observed for an n-type perylene di-imide semiconductor where it reached a factor of 10. As we

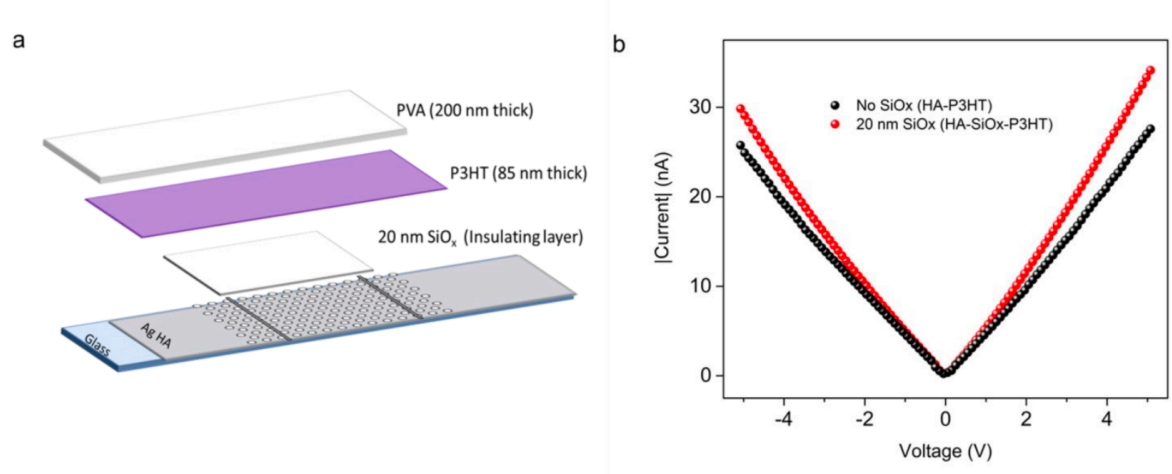

Figure 3.4. a) Schematic representation of the device fabrication with the insulating layer in between the metal and organic semiconductor. b) Comparison of I-V curves of the hole array (P=380 nm) samples with and without an insulating layer in between the metal and organic semiconductor. Figure reproduced from [70].

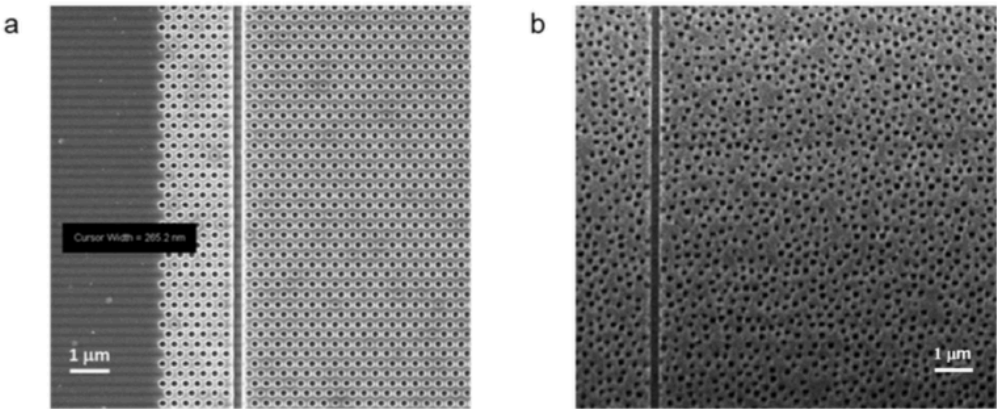

Figure 3.5. SEM image of the a) hole array and b) random array, milled on a 100 nm Ag electrode with the cut clearly shown. Figure reproduced from [70].

demonstrated by comparing three different n-type semiconductors, the disorder in the material appears to have a large negative effect on the enhancement.[68] So one possible explanation for lower enhancement in rr-P3HT, as compared to the best n-type PDI semiconductor we have tested, is the higher disorder.

Several control experiments were carried out to exclude possible artifacts. The presence of oxygen can modify the conductivity of rr-P3HT compounds, so we checked that the results under nitrogen atmosphere for our coated samples were the same within experimental error. The metal substrate is floating and does not contribute to the conductivity due to the Schottky barrier at the semiconductor-metal interface. This was confirmed by depositing a 20 nm insulating SiO_x layer between the metal hole array and organic semiconductor which gave very similar results (Figure 3.4). It was also verified that the observed boosts in current were not due to the cuts that are made in the hole arrays. As shown in the SEM image of the array after the cutting (Figure 3.5 a), the edge is smoothed by the FIB

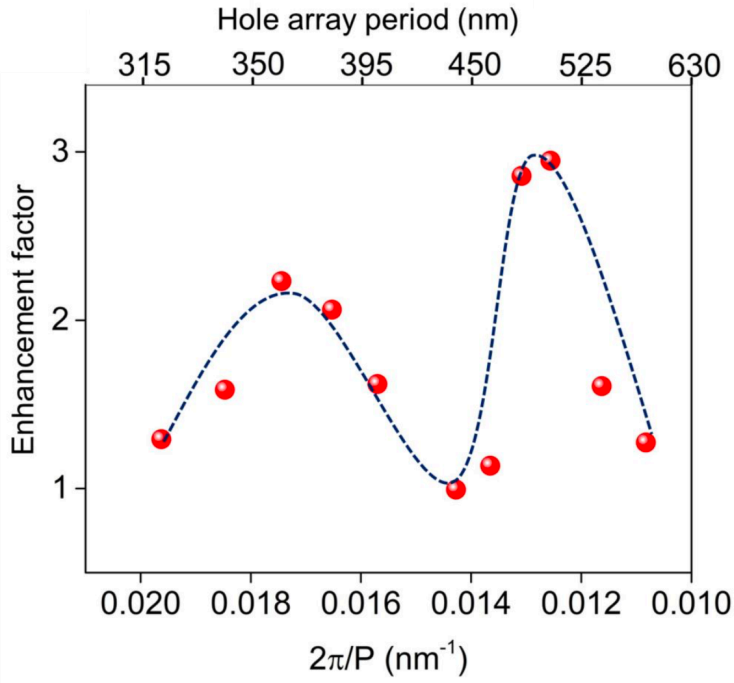

Figure 3.6. Photo-Conductivity enhancement of rr-P3HT with respect to the in-plane momentum of hole arrays. Red dots show the value and blue dashed line is guide to the eye. Figure reproduced from [70].

and finally random hole arrays, which have no pronounced plasmon mode, displays no enhancement (Figure 3.5 b). Enhanced conductivity in a p-type semiconductor under strong coupling indicates that the charge carrying valence band is also affected by the presence of polaritonic states even in the absence of illumination.

We now turn to the photoconductivity measurements. Interestingly, the photoconductivity of rr-P3HT benefits from the enhanced conductivity (Figure S4, SI) under strong coupling in the same way as the dark current does, although the absolute values are higher under illumination (Figure 4). The photoconductivity also peaks for the resonant hole array (P=500 nm; k_x=0.0126 nm^{-1}) with an enhancement factor of ~3, when compared to that of on a random hole array (Figure 3.6). Figure 3.7 a shows the linear dependence of the photocurrent on the excitation intensity for rr-P3HT when measured under white light cw (continuous wave) illumination. At such low intensities per unit area (<15 mW per cm^2), the fraction of excited state absorbers remains at all time negligible and as a consequence there is no significant depopulation of the ground state and the collective Rabi splitting is unmodified. The quantum yield for the photogeneration of charge carriers is estimated to be ca. 5 x 10^{-3} for rr-P3HT (520 nm illumination). The spectral response of the photocurrent was also studied using a tunable pulsed laser source (NKT laser) under strong coupling conditions and compared to that of a random hole array film. The ratio of the current for these two conditions is shown in Figure 4c and reveals enhanced photocurrent at longer wavelengths than the absorbance peak of the bare rr-P3HT with a maximum around 620 nm. This corresponds to the *P*- peak. Since the spectral enhancement at long wavelengths is due to splitting of the original peak into *P*+

and *P*-, a similar enhancement is expected to be seen at shorter wavelength corresponding to the *P*+ transition but our tunable laser system cannot reach the corresponding wavelengths.

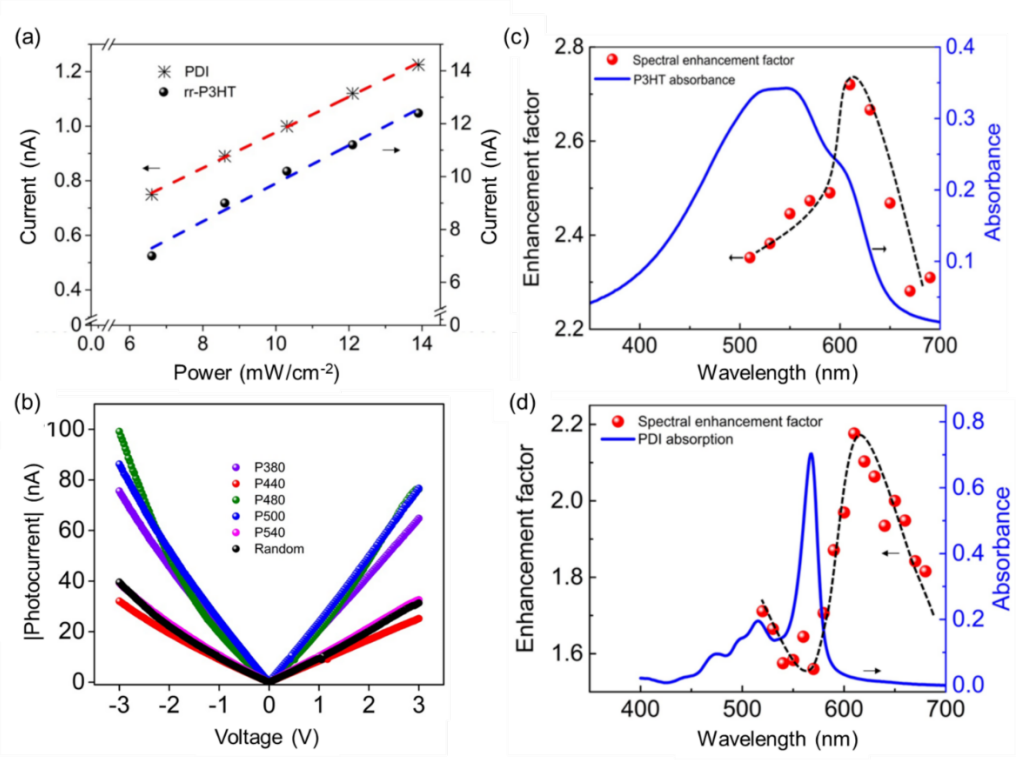

Figure 3.7. Photoconductivity under ultra-strong coupling: (a) Photocurrent as function of the white light illumination power for rr-P3HT and PDI under strong coupling (P= 500 nm and P=280 nm respectively). (b) Current-Voltage (I-V) curves of rr-P3HT samples as a function of the period of the hexagonal hole array under white light illumination (47 mW cm-^{2}). (c) Spectral response under ultra-strong coupling (red dots, P=500 nm) as a function of excitation wavelength, the enhancement factor is the ratio of the photocurrent divided by the corresponding photocurrent of an uncoupled (random array) rr-P3HT film. A tunable pulsed laser with a 10 nm bandpass was used for this study. The peak at 620 nm corresponds to the *P*- peak. The blue curve gives the absorbance spectrum of the bare rr-P3HT film. The black lines are guides to the eye. (d) Idem for PDI under strong coupling (P=280 nm), the peak at 610 nm corresponds to *P*- peak. Figure reproduced from [70].

For purposes of comparison, we also studied the photoconductivity of a perylene di-imide (PDI) n-type semiconductor under strong coupling (Figure 3.8). We have already shown that this class of compounds exhibits an enhanced conductivity under strong coupling.[11]

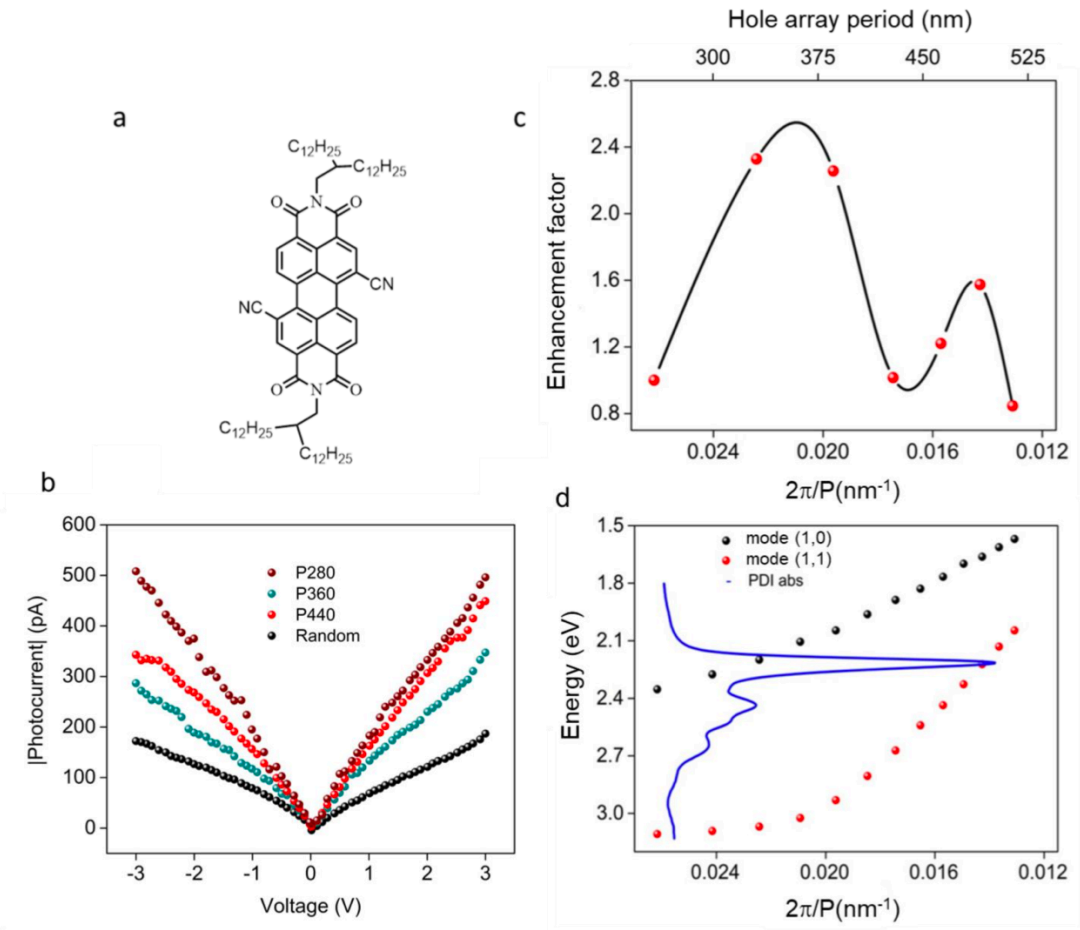

Figure 3.8. a) Molecular structure of PDI. Photocurrent as function of the white light illumination power for PDI under strong coupling (P= 280 nm). b) I-V curves for PDI as a function of the period P of the hole arrays under illumination at 570 nm (41 mW cm^{-2}). c) Conductivity enhancement with respect to the in-plane momentum of hole arrays under illumination. Red dots show the value and black line is guide to the eye. d) The resonance in the current in (c) corresponds to the intersection of the molecular absorbance (blue solid line) and the (1,0) mode (black dots) of the Ag array plasmon resonances where strong coupling occurs. The (1,1) mode of the hole array is indicated by red dots. Figure reproduced from [70].

Figure 3.8 summarizes the results. We observe that the photoconductivity of PDI is also enhanced upon ultra-strong coupling (Rabi splitting is 34% of transition energy) with two current peaks appearing at the crossing of the PDI film absorbance peak and the plasmonic modes. Figure 3.7 a shows the linear dependence of the current with illumination power and Figure 3.7 d shows that just as for rr-P3HT, the spectral response of PDI is enhanced where *P*-absorbs.

3.4 Conclusion

In conclusion, using a p-type organic semiconductor, we have demonstrated that hole transport in the ground state can also be enhanced by strong coupling. This is in turn a direct evidence of the polaritonic character of the valence band, in agreement with theoretical predictions on material properties under ultra-strong coupling.[106] We have also shown that the photoconductivity, like conductivity, can be boosted by the formation of the delocalized polaritonic states and in addition their spectral response can be extended and tailored by the coupling strength. This works for both n- and p-type semiconductors. Strong coupling is easy to implement in a variety of configurations. We, therefore, expect that such results will find applications in devices where photoconductivity plays a role, in particular in photovoltaics and photodetectors. Currently, we are also studying two p-type organic semiconductors with different core structures – perylene and terylene, synthesized by our collaborators from ULB. Comparing the effect of ESC on the conductivity of both the organic molecules will give further insight into the fundamentals of ESC.

4.

SUPRAMOLECULAR ASSEMBLIES UNDER VIBRATIONAL STRONG COUPLING

4.1 Introduction

Supramolecular assemblies are driven by non-covalent interactions such as London dispersion forces, hydrogen bonding, hydrophobic, $\pi - \pi$, and electrostatic interactions.[124,125] External factors such as light,[126] sound,[127] heat,[128] mechanical forces,[129] electrochemical and magnetic effects,[130] and surface plasmons[131] are employed to modulate such assemblies for a plethora of applications, including sensors, drug delivery, and tissue engineering. Last year, Hirai *et al.* reported that VSC of the solvent leads to selective crystallization of metal-organic frameworks (MOFs), thus, indicating that VSC can alter molecular organization.[58] In this Chapter, we demonstrate that VSC modifies supramolecular assemblies and their dynamics.

Since the initial idea was to study the effect on the transport properties of self-assemblies, we have investigated the charge transport properties of conducting polymers under VSC through two different configurations: Fabry-Perot cavity and plasmonic structures. In the former configuration, we observed a massive drop in current during one of the conductivity measurements under ON-resonance conditions. To understand the effect of VSC on the self-assembly process, we analyzed the system using spectroscopic and imaging techniques. Thus,

we found that the morphology of the supramolecular organization is modified under VSC, a serendipitous observation. The results are summarized in the first section, followed by a comparative study of structural isomers of phenylene ethynylene to understand the influence of symmetry on the effect of light-matter strong coupling. Large parts of this Chapter are taken from our already published works. [59,60]

4.2. Supramolecular assembly of Poly(*para*-phenylene ethynylene) under VSC

For years, poly(aryl acetylenes) have been of great interest in the semiconductor industry for polymer electronic devices due to their optoelectronic properties such as efficient charge and energy transfer because of the extended conjugation between the triple bond and adjacent phenyl groups.[132,133] In addition it forms a conductive gel and the gelation phenomenon has been well studied.[134,135] The structure of the assembled molecules depends on the polymer's preparation processes and molecular systems. In this section, we explore the gelation of rigid-rod conjugated polymers under VSC.

4.2.1 Experimental methods

4.2.1.1 System under study

We selected dinonanyloxy-substituted poly(para-phenylene ethynylene) (PPE, inset of Figure 4.1 c) for our study. Concentrated solutions of PPEs form one-dimensional nanowires growing into a fibrous network *via* thermal saturation. In its gel form, PPEs exhibit lamellar packing, which is responsible for the appearance of a well-resolved planarization band in the absorption spectra. In general, both the absorption and the fluorescence spectra of PPEs are

sensitive to molecular packing. Figure 4.1 c shows the vibrational spectra of PPE and dcb (o-dichlorobenzene). Due to the limited solubility of PPE in dcb, it is not possible to directly

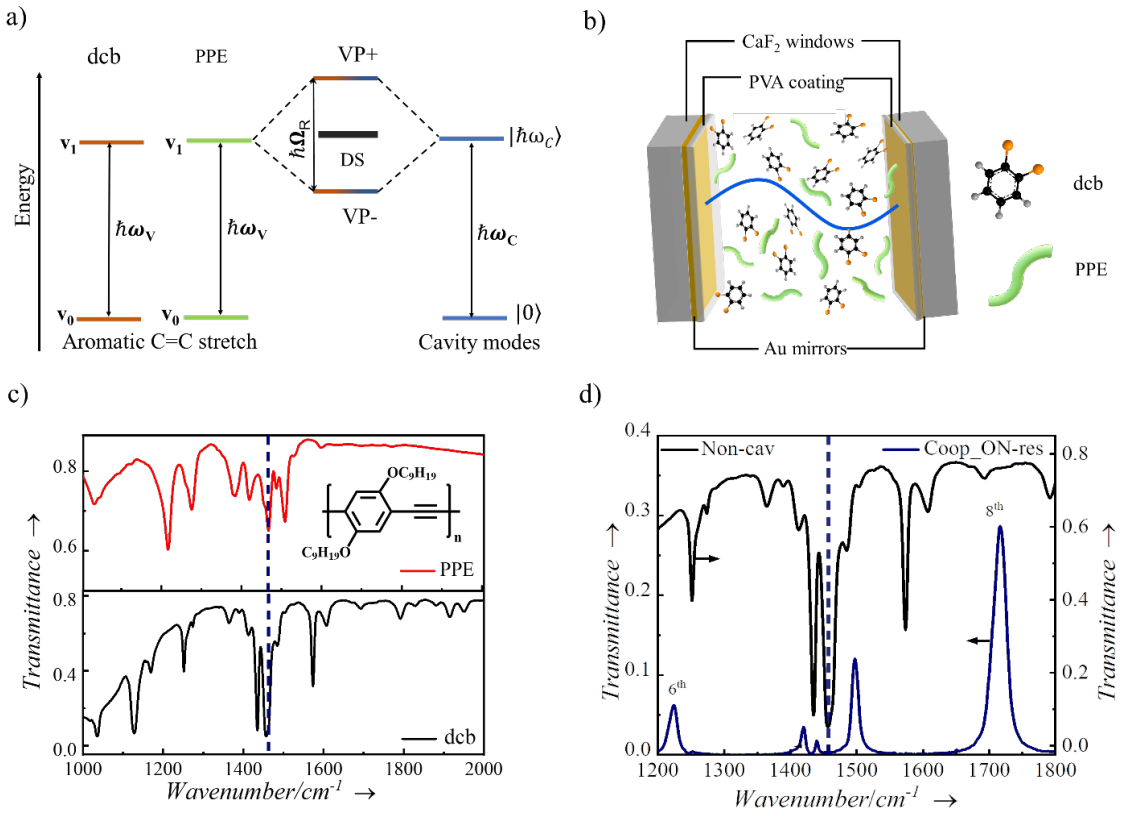

Figure 4.1. a) Schematic representation of cooperative strong coupling between molecular vibration and optical mode of Fabry-Pérot cavity leading to the formation of vibro-polaritonic states. b) Illustration of a microfluidic Fabry-Pérot cavity containing a molecular solution. c) FT-IR transmission spectra of PPE (red curve) and dcb (black curve), blue dashed line shows the overlap of aromatic C=C stretch in PPE and dcb at 1460 $cm^{-1,}$ and the inset shows the chemical structure of dinonanoyloxy-substituted poly(para-phenyleneethynylene) (PPE). d) FT-IR transmission spectra showing the vibro-polaritonic states formed when the aromatic C=C stretching mode at 1460 $cm^{-1}$of the PPE/dcb solution (20mg/ml) is strongly coupled to the cavity. Figure reproduced from [59]

couple the solute. Therefore, we adapt the concept of cooperative effect, i.e., if the solute and solvent have overlapping bands, it is possible to couple the solute via the solvent.

4.2.1.2 Fabrication of Fabry-Perot cavity

To study the effects of VSC on the supramolecular organization of PPE, we have used microfluidic tunable optical Fabry-Perot (FP) cavities. The FP cavity (Figure 4.1 b) consists of two parallel mirrors fabricated by sputtering 10 nm of Au on CaF_2 substrates and protecting them with a 100 nm thick layer of spin-coated polyvinyl alcohol (PVA). The two mirrors were separated by a 10 μm thick Mylar spacer and assembled into a microfluidic cell. The spacing between the two mirrors is finely tuned with four screws holding the microfluidic cell together (see URL: https://seafile.unistra.fr/d/7bb78e5a4607424f94b5/) to couple the desired vibrational mode of the solvent o-dichlorobenzene (dcb) in which PPE is dissolved.

4.2.2 Results and discussions

4.2.2.1 Characterization through absorption and fluorescence studies

PPE is strongly coupled to the 7^{th} optical mode of the FP cavity by coupling the aromatic C=C stretch of dcb ($1460cm^{-1}$), which leads to the formation of vibro-polaritonic states (Figure 4.1 a, d). Figures 4.2 a-c show the progression of supramolecular self-assembly recorded every 0.5 minutes with a Shimadzu spectrophotometer, at 24 °C, in non-, OFF- and ON- resonance cavities. In non- and OFF-resonance cavities, the results are identical with the appearance of a sharp maximum at 478 nm corresponding to the planarization band (planar assembly of the PPE) and a slight decrease in the band at 440 nm, in agreement with the literature.[136,137]

Spectral evolution under ON-resonance is entirely different, with a red-shifted isosbestic point suggesting a new type of assembly. The band at 478 nm is much less pronounced, and the 440 nm band is red-shifted and broader. The self-assembly rate constant increases by ca. 20% under cooperative VSC (see Table 4.1). Figures 4.2 d-f show the final absorption and fluorescence spectra of the assemblies. The latter spectra are again very different for the supramolecular assembly under cooperative VSC.

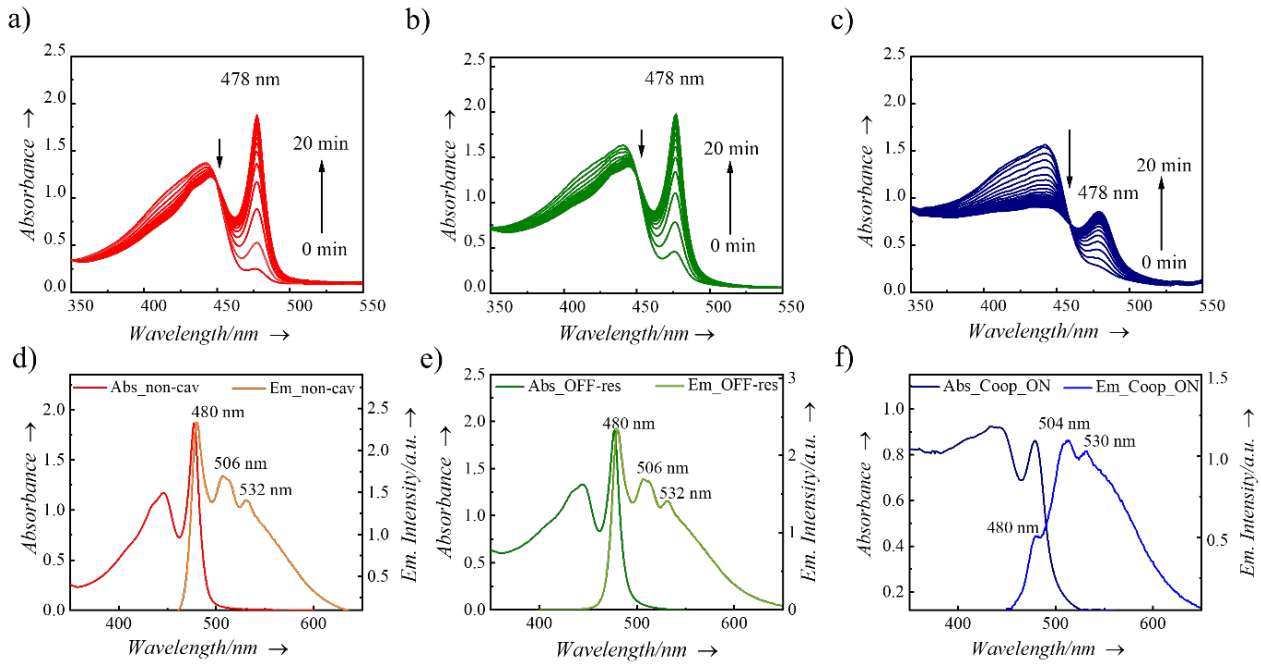

Figure 4.2. Absorption spectra showing the time evolution of self-assembly in a) non-cavity, b) OFF-resonance, and c) ON-resonance cavities. Absorption and emission spectra of the self-assembled structures were recorded in d) non-cavity, e) OFF-resonance, and f) ON-resonance cavities. Figure reproduced from [59]

Experiment	**Vibrational mode (cm^{-1})**	**Rabi splitting ($\hbar\Omega_R$, cm^{-1})**	**Morphology**	**Rate constant (10^{-3} sec^{-1})**
		PPE/dcb		
Non-cavity			Fibers	6.2 ± 0.19
OFF-resonance			Fibers	6.3 ± 0.25
Coop. ON-resonance[§]	1460	62	Flakes	7.4 ± 0.07
ON-resonance[†]	1435	40	Fibers	8.1 ± 0.21
ON-resonance[†]	1127	46	Fibers	1.8 ± 0.02
		PPE/D_4-dcb		
Non-cavity			Flakes	3.4 ± 0.03
ON-resonance[†]	1345	64	Flakes	~3*

Table 4.1: Morphology and rate constants of the PPE supramolecular assembly. §= ON-resonance cavity experiment under cooperative VSC of solvent and solute; † = ON-resonance cavity experiments with VSC of only solvent. * = value estimated from first half-life due to complex kinetic trace. Reproduced from ref [59]

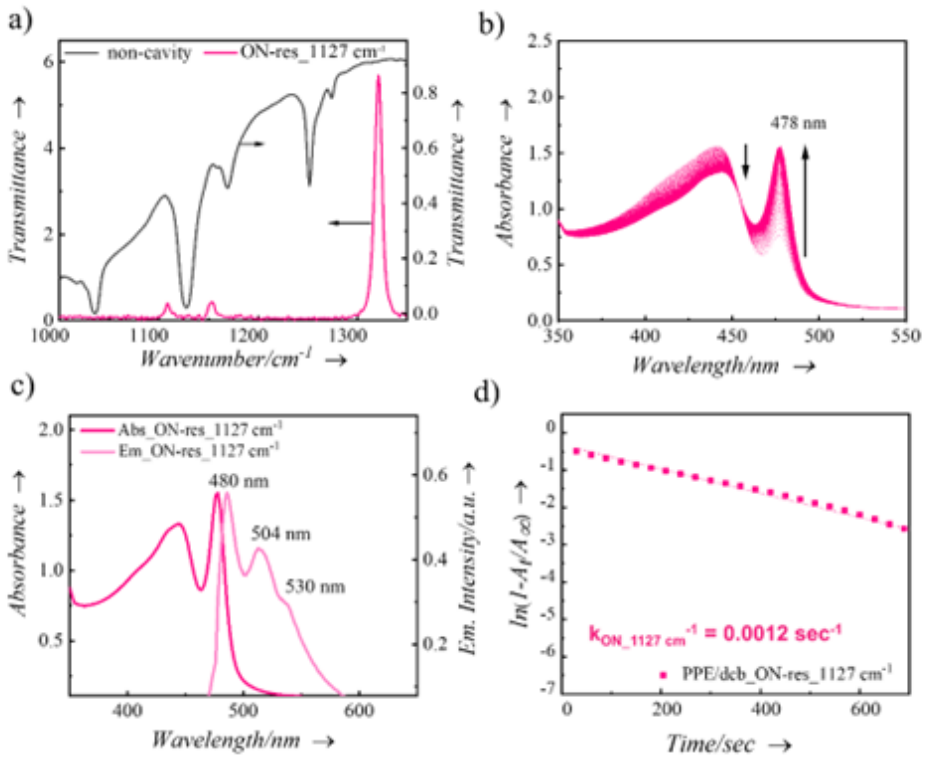

Figure 4.3. (a) FT-IR transmission spectra showing the vibro-polaritonic states formed when aromatic C=C stretch of solution (PPE/dcb) at 1127 cm^{-1} is strongly coupled to the cavity. (b) Absorption spectra showing the evolution of self-assembly in an ON-resonance cavity. (c) Absorption and emission spectra of the self-assembled structures recorded in an ON-resonance cavity (d) the corresponding self-assembly kinetics. Figure reproduced from [59]

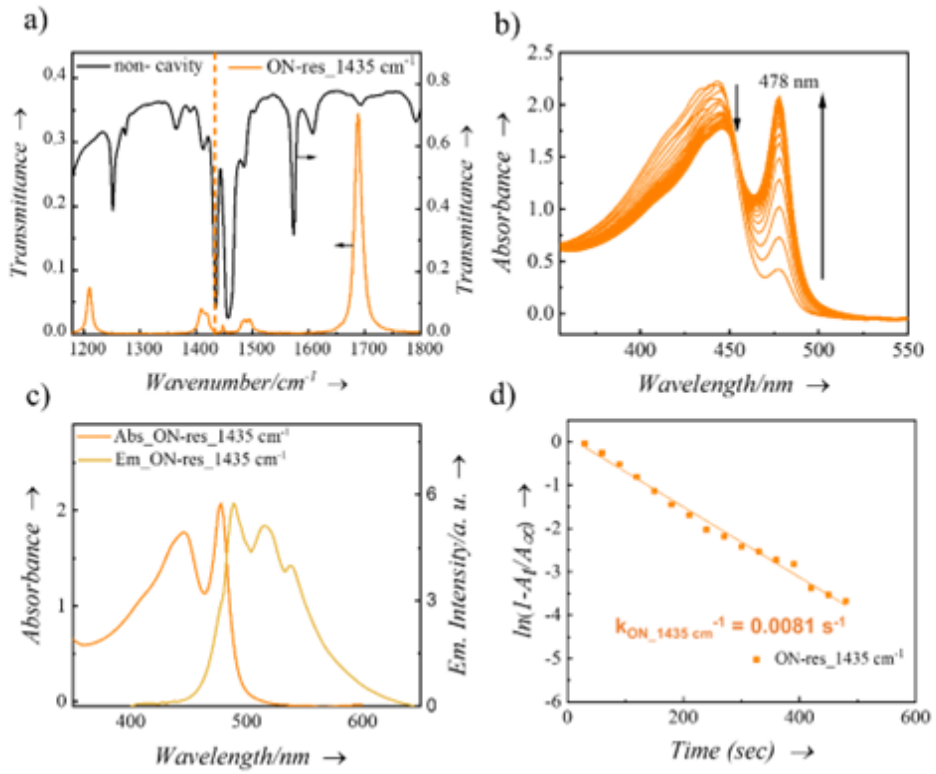

Figure 4.4. (a) FT-IR transmission spectra showing the vibro-polaritonic states formed when aromatic C=C stretch of solution (PPE/dcb) at 1435 cm^{-1} is strongly coupled to the cavity and is detuned at 1460 cm^{-1}. Note that the vibrational band at 1460 cm^{-1} suppresses the VP+ peak. (b) Absorption spectra showing the evolution of self-assembly in the ON-resonance cavity. (c) Absorption and emission spectra of the self-assembled structures recorded in the ON-resonance cavity and (d) the corresponding self-assembly kinetics. Figure reproduced from [59]

Finally, VSC of other vibrational bands of the solvent, such as the ones at 1127 cm^{-1} (Figure 4.3 a, C-H deformation mode) and 1435 cm^{-1} (Figure 4.4 a, asymmetric aromatic C=C stretching mode), modify the kinetics (Figure 4.3 d, Figure 4.4 d) as summarized in Table 4.1. While the absorption spectra of the final assembly are very similar to the non-cavity case, there is a small 4 nm shift in the isosbestic points (Figures 4.3 b and 4.4 b), indicating some change in the organization at the molecular scale. It should be recalled that only the solvent is coupled in these cases.

4.2.2.2 Morphology studies through SEM and TEM

The resulting assemblies were characterized by scanning and transmission electron microscopies (SEM and TEM) to verify whether the supramolecular organization is modified under cooperative VSC. The different cavities were opened after the evaporation of the solvent, and CaF_2 substrates were directly studied first by SEM. The deformation of CaF_2 windows under tuning restricts the ON-resonance region to the tuned central area of the cavity. When analyzing this area, the SEM images of material in non-cavity and ON-resonance cavity show a significant difference in the structure of the supramolecular organization (Figures 4.5 a and d). A fibrous network is seen for both non- and OFF-resonance cavities, typical of PPE self-assembled structures. In contrast, the PPE formed large flakes for the ON-resonance condition, as seen in Figure 4.5 d. Furthermore, in the latter case, if one moves to an area that is OFF-resonance due to deformation of the mirrors, fibers are seen as expected.

To further understand the packing structures on a smaller scale, PPE self-assembled material was transferred to a TEM grid and imaged. To transfer the self-assembled structures, selected region on the surface of CaF2 substrate was scratched using a diamond cutter under an acetone drop, as shown in Figure 4.5 g, and the fragments were collected on a TEM grid. Figures 4.5 b and c reveal the ordered lamellar packing of the PPE fibers in agreement with the literature.[136,137] In the ON-resonance cavity, on the other hand, the flakes appear completely amorphous, as seen in Figures 4.5 e and f. Nevertheless, the peak at 478 nm in Figure 4.2 c indicates that some packing order remains at the molecular scale.

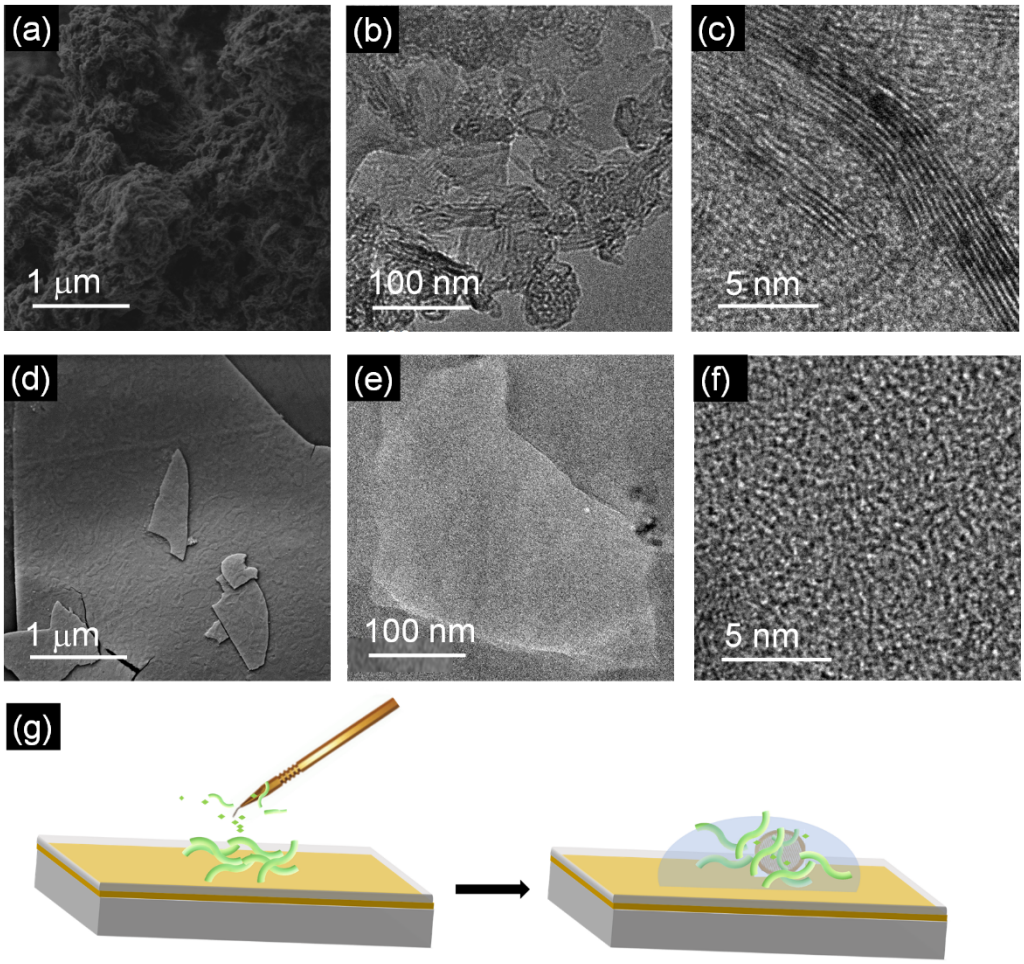

Figure 4.5. SEM and TEM images of PPE rigid polymer assembled into the fibrous network in non-cavity (a-c) and flakes under cooperative VSC (d-f). a and d are SEM images, and b, c, e, and f are TEM images. (g) Illustration of the method used to transfer samples to the TEM grid. Figures a-f reproduced from [59]

4.2.2.3 Detuning studies

A fibrous network is seen for both non- and OFF-resonance cavities, typical of PPE self-assembled structures (Figures 4.6 d, h and t). In contrast, the PPE formed large flakes for the ON-resonance condition, as seen in Figures 4.7 l and p. Furthermore, in the ON-resonance case, if one moves to an area that is OFF-resonance due to deformation of the mirrors, fibers are seen as expected. The complete results of detuning experiments are shown in Figure 4.6.

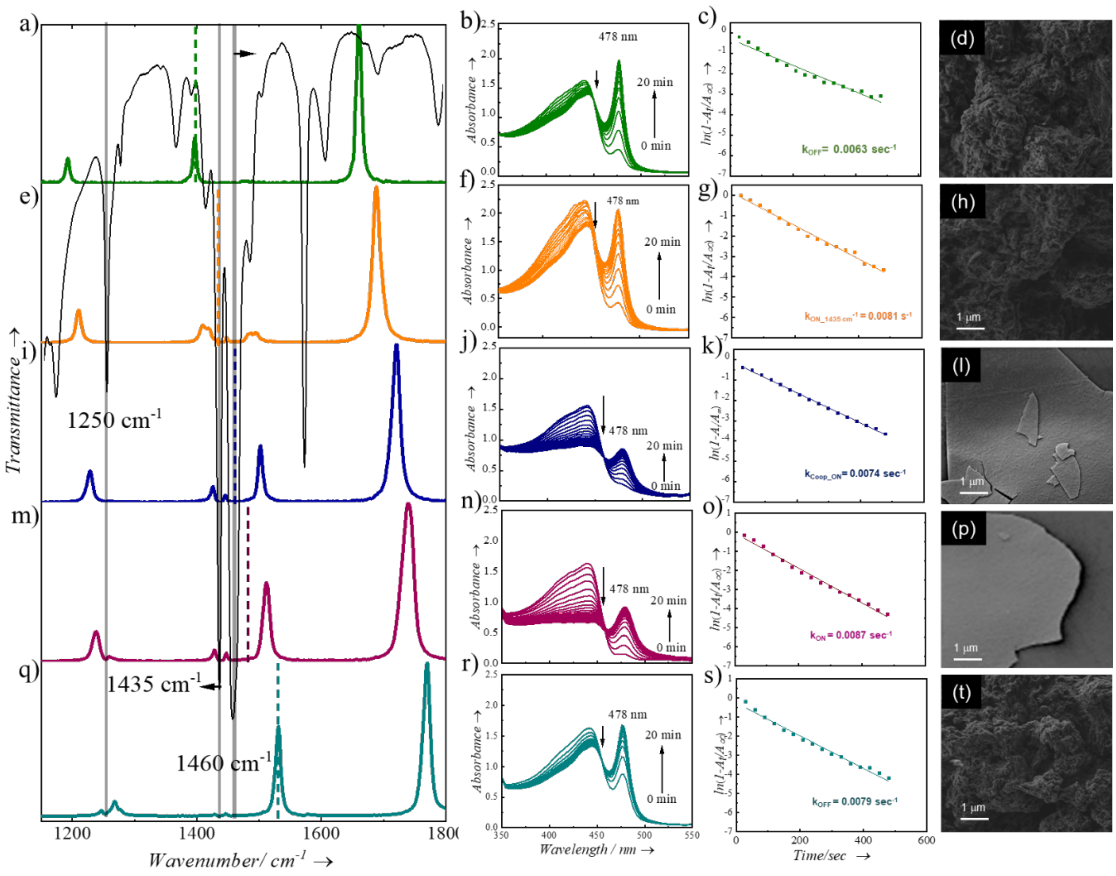

Figure 4.6 Results from the cavity tuning experiment. (a) FT-IR transmission spectrum of an OFF-resonance cavity. (Black solid line is the FT-IR transmission spectrum of dcb) (b-d) are the corresponding absorption spectra, kinetics and SEM image of fibrous network formed in the OFF-resonance cavity. (e) FT-IR transmission spectrum of the cavity where the optical mode is detuned from the vibrational mode at 1460 cm^{-1} but strongly coupled to the mode at 1435 cm^{-1}. (f-h) are the corresponding absorption spectra, kinetics plot and SEM image of fibrous network formed in the detuned cavity. (i) FT-IR transmission spectrum of an ON-resonance cavity. (j-l) are the corresponding absorption spectra, kinetics plot and SEM image of amorphous flakes formed in the ON-resonance cavity. (m) FT-IR transmission spectrum of the cavity with optical mode slightly detuned to the higher wavenumbers. (n-p) are the corresponding absorption spectra, kinetics plot and SEM image of amorphous flakes formed in the cavity. (q) FT-IR transmission spectrum of an OFF-resonance cavity with cavity mode at higher wavenumbers. (r-t) are the corresponding absorption spectra, kinetics plot and SEM image of fibrous network formed in the OFF-resonance cavity. Figure reproduced from [59].

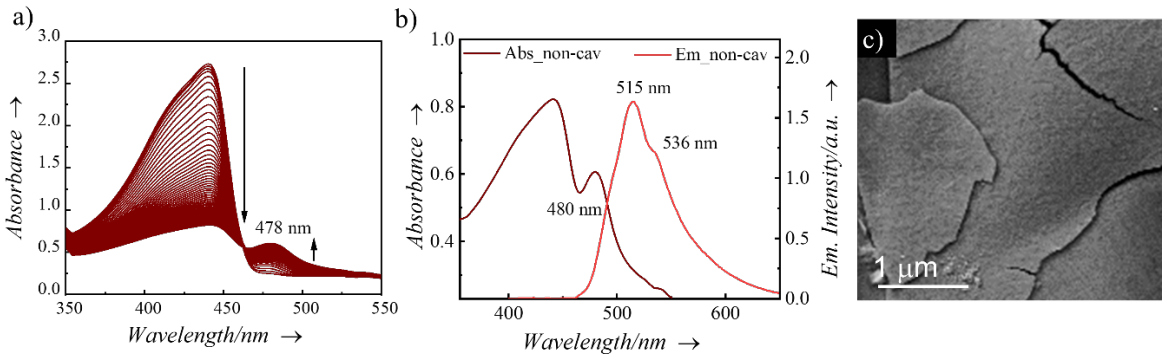

Figure 4.7. a) Absorption spectra showing the evolution of self-assembly of PPE in D_4-dcb in non-cavity. b) Absorption and emission spectra of the self-assembled structure of a). c) SEM image of flakes of PPE formed in D_4-dcb in non-cavity. Figure reproduced from [59]

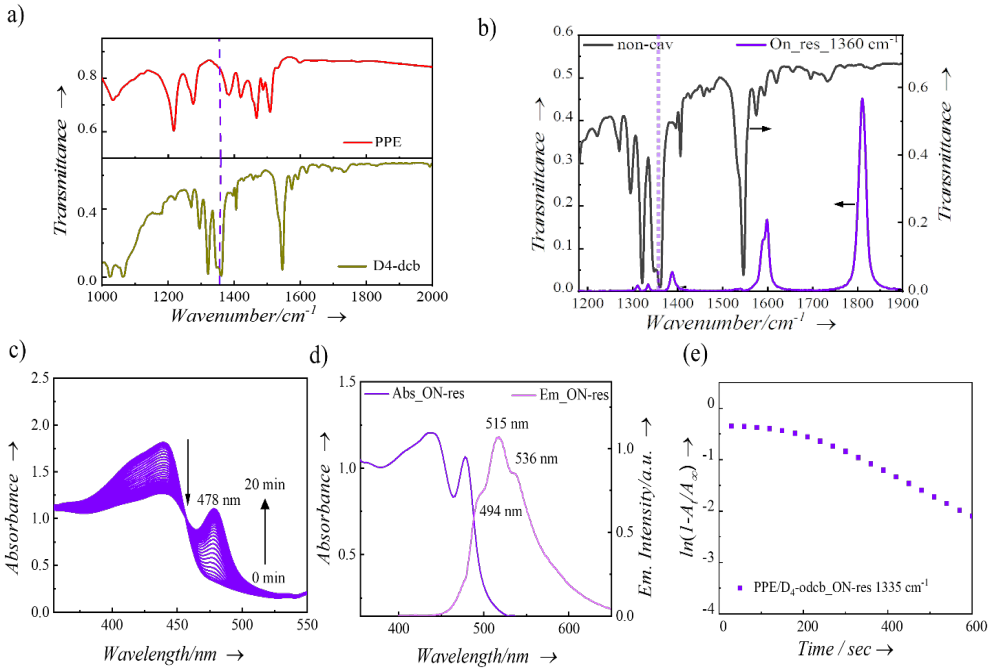

Figure 4.8. (a) FT-IR transmission spectra of PPE (red curve) and D_4-dcb (mustard-yellow curve), (b) FT-IR transmission spectra showing the vibro-polaritonic states formed when aromatic C=C stretch of solution (PPE/D_4-dcb) at 1350 cm^{-1} is strongly coupled to the cavity. (c) Absorption spectra showing the evolution of self-assembly in ON-resonance cavity. (d) Absorption and emission spectra of the self-assembled structures recorded in ON-resonance cavity and (e) the corresponding ln plot of self-assembly. Figure reproduced from [59]

4.2.2.4 Isotope studies

In Table 1, while cooperative VSC perturbs both the kinetics and the morphology of the PPE supramolecular assembly, coupling the solvent alone just leads to kinetic changes. To gain further insight into the factors influencing these results, the PPE assembly was studied in a deuterated solvent, 1,2-dichlorobenzene-D_4. While cooperative coupling is not possible in this case because none of the vibrations of this deuterated solvent match that of PPE (Figure 4.8 a), the spectral changes in a non-cavity (deuterated, Figure 4.7 a, b) are very similar to the ON-resonance under cooperative VSC (non-deuterated, Figure 4.2 c, f) with the appearance of flakes as shown in Figure 4.7 c.

Under VSC of the deuterated solvent (Figure 4.8 b), nothing changed in morphology and spectra (Figure 4.8 c, d) with respect to the non-cavity of the same solvent as summarized in Table 1. There are reports showing the effect of isotope substitution (upon changing from H_2O to D_2O) on the rates and morphology of other self-assemblies such as J-aggregate formation and self-assembled macroions.[138,139] Change in charge distribution around atoms and molecules due to the isotope effect leads to the modification of intermolecular interactions.[140,141] This can cause a disparity in the energy barrier during the self-assembly process, creating a difference in kinetic rates. Since the interactions between solute and solvent are also modified, it affects the self-assembly pathway and thus the modification of morphology of supramolecular organization.

In light of these observations, it is clear that vibrational strong coupling strongly influences the evolution of supramolecular assembly. To verify the possible influence of symmetry of molecules on the effect of strong coupling, we now compare the self-assembly of structural isomers of organic molecules- phenylene ethynylenes under VSC.

4.3.Supramolecular assembly of Oligo phenylene ethynylene under VSC

4.3.1 Experimental methods

We have studied two structural isomers of phenylene ethynylenes (PE) molecules: linear and bent isomers having different polarities. PE based molecular systems are known to aggregate through π–π stacking and CH- π interactions.[142] We observed that VSC has a profound effect on the self-assembly of V-shaped isomers but surprisingly not on the other, as presented below. The PE molecules (PE1 and PE2) were synthesized by palladium-catalyzed Heck-Cassar-Sonogashira-Hagihara cross-coupling reactions (Scheme 4.1). [143] In this synthesis, diiodobenzene is allowed to react with two equivalents of phenylacetylene in the presence of $Pd(PPh_3)_2Cl_2$, CuI, and triethylamine at room temperature under an inert atmosphere.

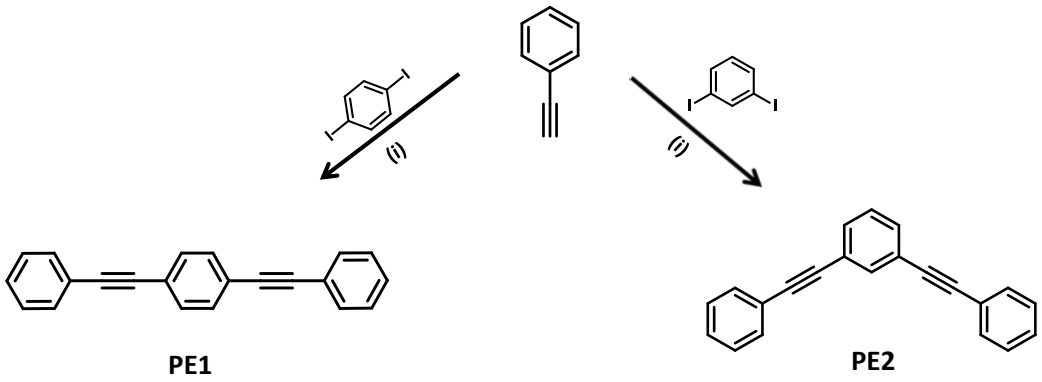

Scheme 4.1. Synthesis of PE molecules: (i) $Pd(PPh_3)_2Cl_2$, CuI, triethylamine, and tetrahydrofuran. The linear isomer is labeled as PE1 and the bent molecule as PE2. Reproduced from [60]

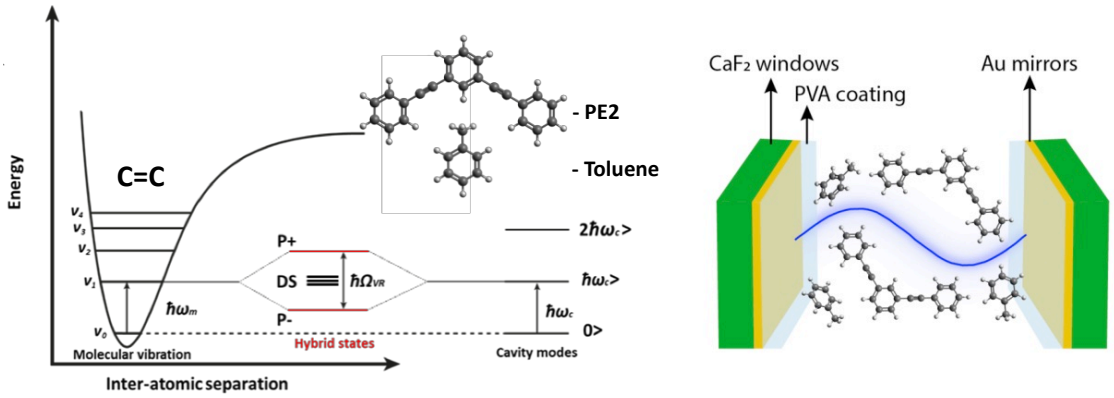

Figure 4.9. (A) Schematic representation of the generation of polaritonic states, P+ and P-, as a result of cooperative VSC of toluene and PE molecules in an FP (CaF_2/Au/PVA) cavity. Figure reproduced from [60]

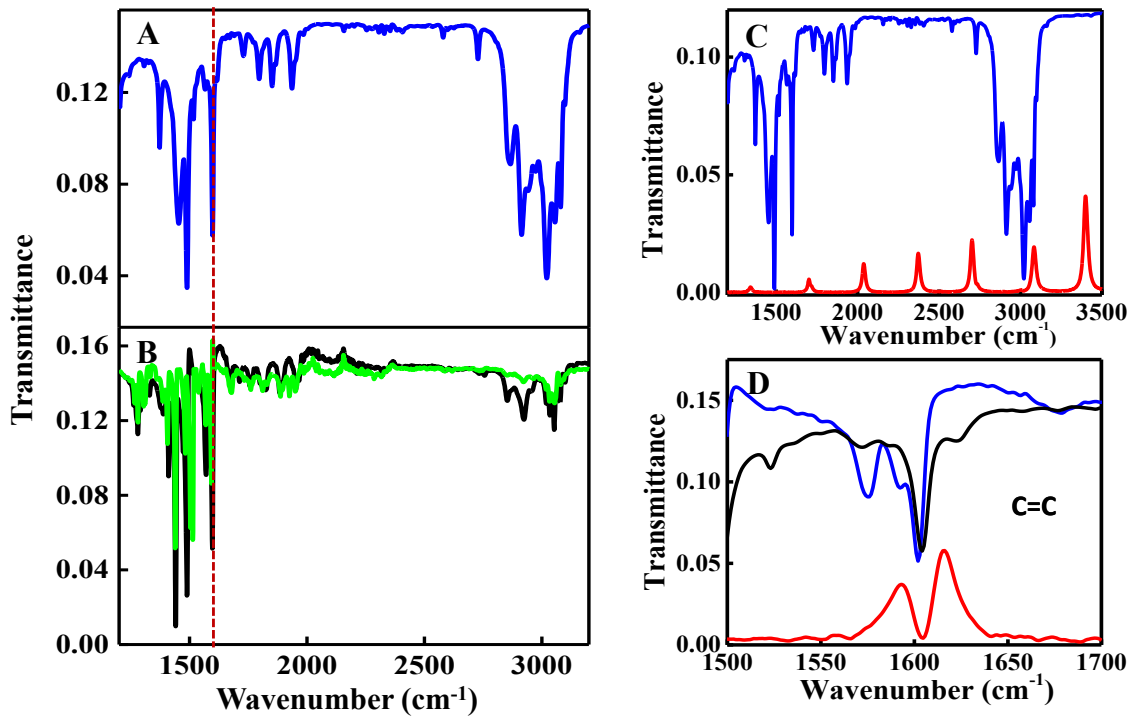

Figure 4.10. (A,B) Fourier transform infrared (FTIR) spectrum of toluene (A, blue trace) taken in a cell is compared with the attenuated total reflectance IR spectra of PE1 (B, green trace) and PE2 (B, black trace). All the molecules show a vibrational transition around 1603 cm^{-1}, and which facilitates the cooperative strong coupling. (C) FTIR spectrum of the off-resonance cavity, where none of

the optical modes (red traces) of the cavity are in resonance with the vibrational transitions of PE and toluene (blue trace). (D) On-resonance cavity where the IR peak at 1603 cm^{-1} of the PE and toluene are coupled with the 5th mode of the FP cavity. Figure reproduced from [60]

Using the method mentioned in previous section (Section 4.2.1.2), Fabry-Perot cavities were fabricated (Figure 4.9 B). The vibrational spectrum of toluene in a cell (i.e., non-cavity made by assembling of two CaF_2 windows separated by a 8 μM Mylar spacer without the Au mirror coating) was recorded and compared with the infrared (IR) spectrum of the PE molecules (Figure 4. 10 A,B). The C=C stretching frequency of the toluene and the PE molecules is very close at ca.1603 cm-1, enabling the cooperative coupling of toluene and PE. In other words, toluene is strongly coupled, and intermolecular interactions in the solvation shell drive the VSC of the resonant PE molecules.[19] The concentration of the PE molecules was 9 mM in toluene, and thus, the absorbance of neat toluene (ca. 9 M) completely dominates at 1603 cm^{-1}. The OFF-resonance cavity (Figure 4.10 C, red curve), in which none of the vibrational transitions of toluene and PE are in resonance with the optical modes of the cavity, serves as a control experiment. The ON-resonance condition was achieved by coupling the aromatic C=C stretch of toluene to the 5th cavity mode of the FP cavity (Figure 4.10 D), where the Rabi splitting was found to be 24 cm^{-1} which is larger than the full width at half maximum (FWHM) of the cavity modes (20 cm^{-1}) and the vibrational transitions (7 and 9 cm^{-1}, toluene and PE respectively), thereby meeting the necessary conditions for VSC.

4.3.2 Results and discussions

The self-assembly of the PE molecules in toluene in the presence and absence of VSC was investigated by both spectroscopic and imaging techniques. First, we will discuss the

effect of VSC on the supramolecular organization of PE2 (bent molecule). This section is followed by the study of PE1 (linear molecule) under similar conditions.

4.3.2.1 Characterization through absorption and fluorescence studies

Figure 4.11 shows the results for the PE2 molecule under cooperative VSC. The experiments were carried out at a fixed temperature (23 ºC) with 9 mM PE2, and the absorption

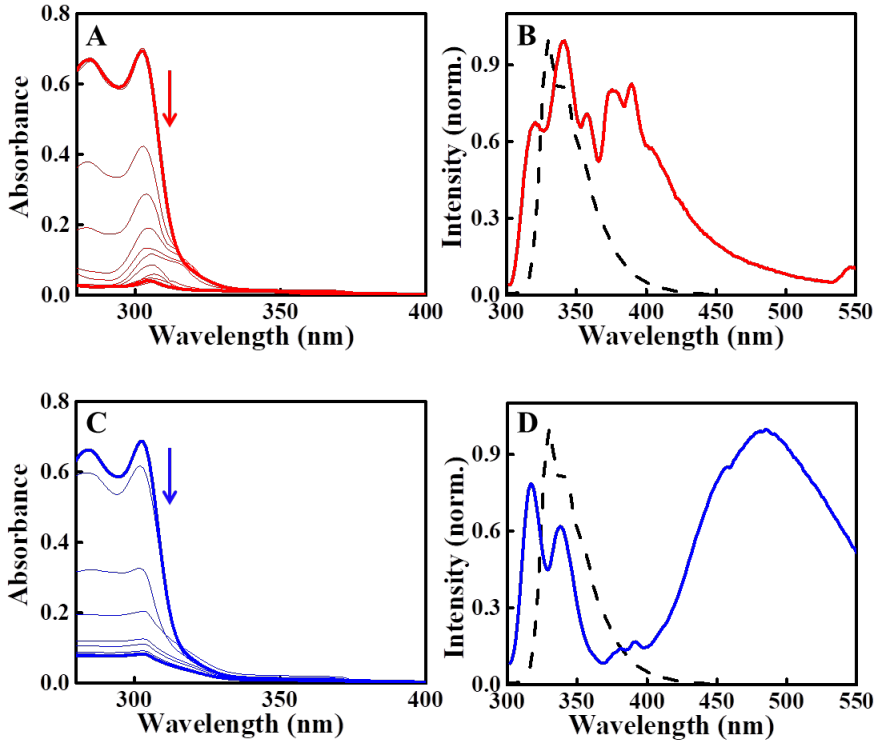

Figure 4.11. (A-D) Spectroscopic investigations of the self-assembly of PE2 molecules (9 mM in toluene, 23ºC) under ON-resonance (A,B) and OFF-resonance (C,D) conditions. Self-assembly of the PE2 molecule is monitored as a function of time by UV-vis absorption spectroscopy under VSC (A) and OFF-resonance (C) conditions (spectra are recorded every minute). The emission spectra (B,D) of the PE2 monomer (black dashed line) and after aggregation in the presence (B, red trace) and absence (D, blue trace) of VSC. Figure reproduced from [60]

was monitored in the presence (Figure 4.11 A) and the absence (Figure 4.11 C) of VSC as a function of time. As a result of the aggregation, we observed a decrease in absorbance in both cases. Interestingly, a small but significant difference in the absorption spectrum of the self-assembled structures is found under VSC.

It is well known in the literature that the different types of aggregate packing result in a change in electronic absorption and emission properties in such conjugated molecules.[143,144] Thus, we also checked the fluorescence of the different samples under ON-resonance and OFF-resonance conditions and compared it with the emission spectrum of the monomer (Figure 4.10 B,D). As can be seen, VSC induces drastic changes in the fluorescence spectrum, confirming that the self-assembled structure has a different packing under strong coupling.

4.3.2.2 Morphology studies through imaging techniques: SEM and optical microscopy

Next, scanning electron microscopy (SEM) was used to visualize the structural changes induced by VSC (Figure 4.12 A-D). The cavities were opened, and the substrates were directly studied under SEM. Interestingly under cooperative VSC of PE2, mostly spherical structures are formed, as is clearly visible in the sample, whereas, in the absence of strong coupling, the aggregation of PE2 resulted in the formation of 2D amorphous flakes (Figure 4 C, D). Interestingly, the spherical structures are very large, ranging from 2 to 20 μm in diameter, and sparse, probably due to few nucleation events. They consist of an outer wall and a dense core that scatters brightly in the SEM image, and these are separated by a dark zone suggesting much less material present. The formation of monomer molecules upon dissolving the aggregates formed in the absence and presence of VSC in a good solvent discard any type of chemical modifications. The optical images taken before opening the ON- and OFF- resonance

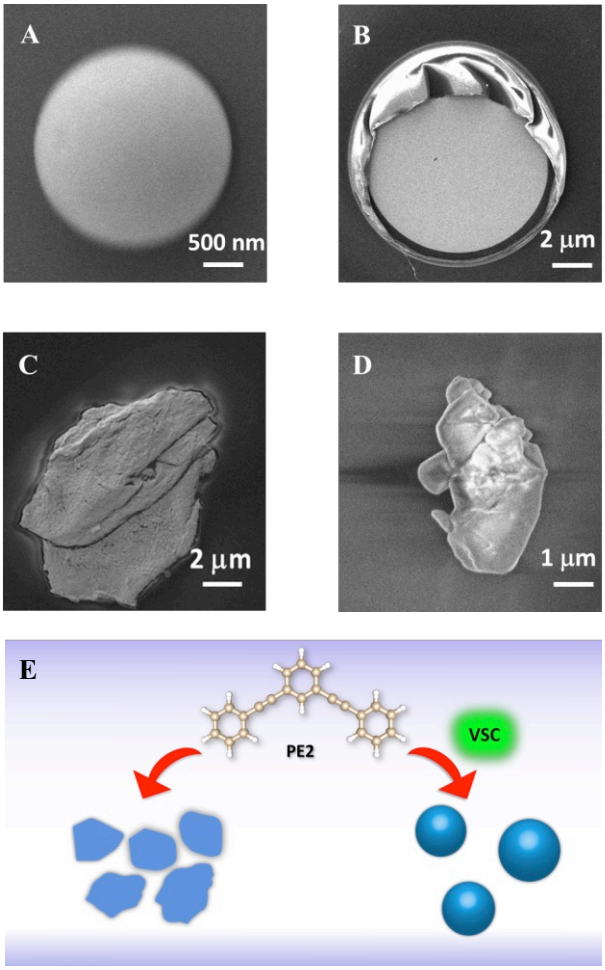

Figure 4.12. SEM images of the structures formed after the self-assembly of PE2 under VSC (A,B) and off-resonance (C,D) conditions. (E) Schematic representation of the formation of different self-assembled structures in the absence and presence of VSC. Figure reproduced from [60]

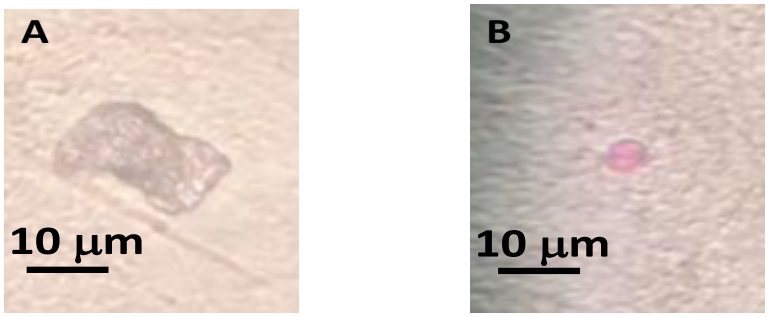

Figure 4.13. Characterization of PE2 aggregates with optical microscopy under (A) OFF-resonance and (B) ON-resonance conditions. Note: under OFF-

resonance conditions, aggregation of PE2 results in the formation of amorphous flakes and forms spheres under VSC. Figure reproduced from [60]

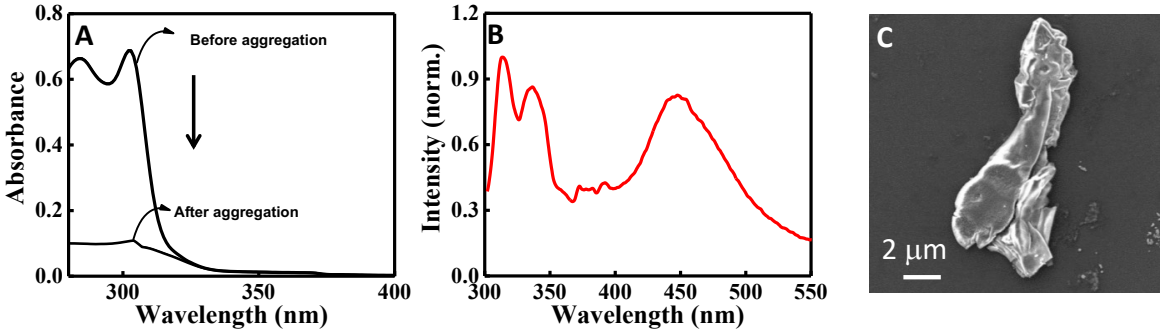

Figure 4.14. Self-assembly of PE2 carried out under non-cavity conditions. (A) The absorption spectrum of the PE2 molecule before and after aggregation. (B) Emission spectrum (B) and the SEM image of PE2 aggregate. Note: cell experiments resemble the OFF-resonance aggregation of PE2. Figure reproduced from [60]

cavities (Figure 4.13), confirm that the corresponding spherical structures and flakes are already present in the solution.

The aggregation experiments in a non-cavity under similar conditions were also performed as a control experiment. The absorption, emission, and structure of the aggregates are identical to those of OFF-resonance conditions as shown in the Figure 4.14. We will now discuss the PE1 results in cavity.

4.3.2.3. PE1 supramolecular structures formed inside and outside the cavity

Figures 4.15 A and B show the FTIR transmission spectra of OFF- and ON-resonance cavities with PE1 molecules. In the latter one, optical mode is coupled to the aromatic C=C stretch of toluene. From the spectroscopic and imaging data (Figure 4.13 C-H), one can confirm

that the self-assembled structures of PE1, the linear isomer of phenylene ethynylene, were not modified by cooperative VSC, under the identical conditions. It is clear from these results that

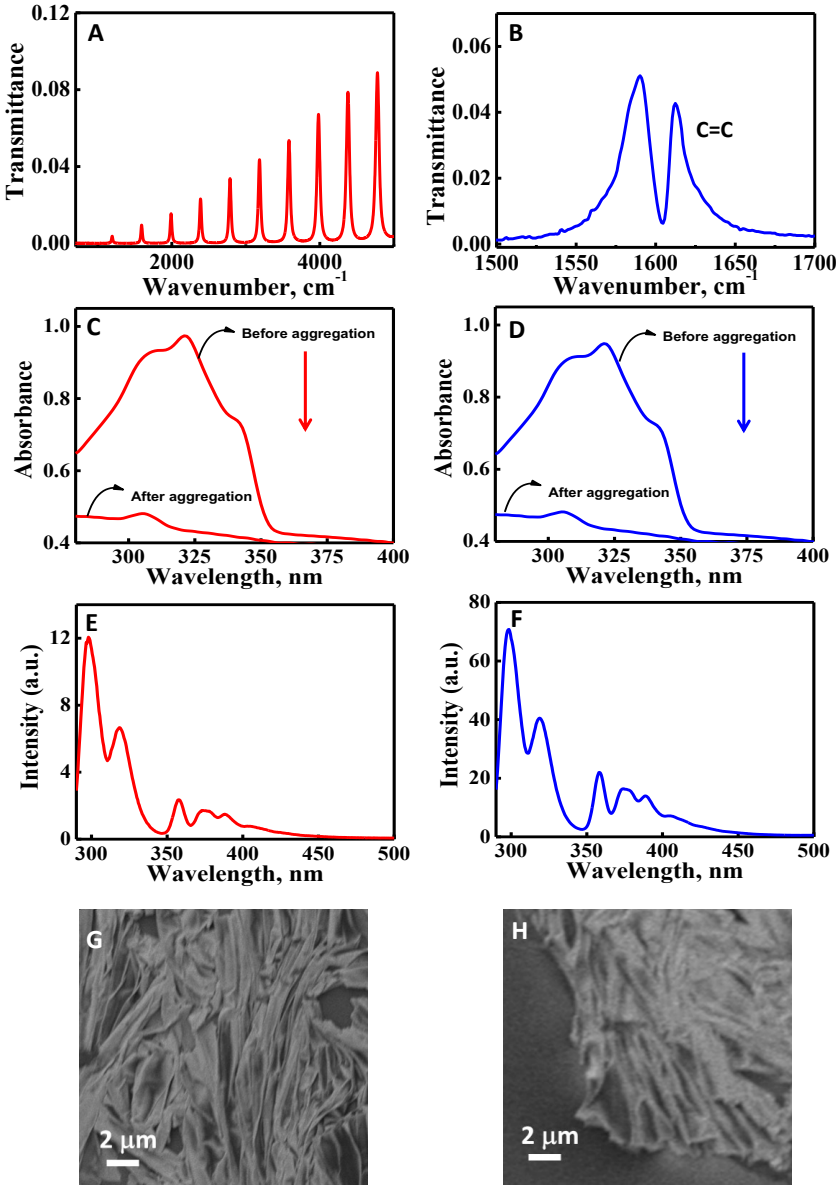

Figure 4.15. (A) FTIR spectrum of the off-resonance cavity, where none of the optical modes (red traces) of the cavity are in resonance with the vibrational transitions of PE1 and toluene. (B) On-resonance cavity where the IR peak at 1603 cm^{-1} of the PE1 and toluene are coupled with the optical mode of the FP cavity. (C,D) Absorption spectrum of the PE1 before and after aggregation under off-resonance (C) and on-resonance (D) conditions. (E,F) Emission spectrum of the self-assembled product formed in the absence (E) and presence

(F) of VSC. (G,H) SEM images of the aggregates formed under off-resonance (G) and on-resonance (H). Figure reproduced from [60]

PE2 (C_{2v} point group) has larger dipole moment than that of centrosymmetric PE1 ($D_{\infty h}$ point group) which might make more sensitive towards the changes induced by cooperative VSC.

4.4. Conclusion

PPE and OPE results confirm that cooperative VSC drives the self-assembly process through a different chemical potential landscape, thus modifying their morphology and kinetics. Isotopic differences in vibrational anharmonicities alter the electronic properties of molecules, thus, affecting chemical equilibrium, reaction kinetics, and self-assembly processes.[140,141] The similarities between the isotope effect and cooperative VSC observed for PPE molecules suggest that the shift in vibrational frequencies and other fundamental parameters might modify the self-assembly processes. In addition, the OPE results indicate that symmetry and the dipole moment of the molecules has a significant role in determining the effect of VSC on supramolecular interactions in agreement with earlier studies.[80,84]

The most likely reason for these observations is a modification in the dispersive interactions. As known from quantum electrodynamics, vacuum electromagnetic field fluctuations occur everywhere in the universe and play an essential role in the van der Waals dispersive forces.[38] The dispersive interactions might therefore be amplified by the strong coupling with the vacuum field and the coherent collective coupling of many solvent molecules to the same optical mode. So it is perhaps not surprising that the supramolecular interactions are modified under strong coupling with the 'vacuum' electromagnetic field. These results indicate that VSC can alter solvent properties and solvation.

To summarize, the modification of supramolecular organization under VSC is a powerful example of the potential of light-matter strong coupling to control molecular processes. Once the complex effect of VSC on solvents and intermolecular interactions is better understood, it could be used to manipulate supramolecular assemblies in a systematic way.

5.

CONDUCTIVITY OF PEDOT: PSS UNDER VIBRATIONAL STRONG COUPLING

5.1 Introduction

It has already been shown that coupling the electronic transition of a p-type and n-type organic semiconductor to optical modes can enhance their conductivity and photoconductivity as discussed in Chapter 3. [3–15] Since lattice vibrations are known to have a significant role in the transport properties of organic semiconductors, in this Chapter, we explore the effect of VSC on the conductivity of the poly(3,4-ethylene dioxythiophene) polystyrene sulfonate (PEDOT: PSS, structure shown in Figure 5.1). Due to its optical transparency, thermal stability, and high conductivity, this conducting polymer has received much attention in the past years. The conductivity of PEDOT: PSS can be significantly enhanced by secondary doping,[145–147] and light[148] and thermal treatments.[149] However, due to its instability in air, the polymer chain gets oxidized (formation of carbonyl group) and the conductivity drops. Here, we demonstrate that VSC can not only enhance the conductivity of the material but also restore the conductivity of the polymer film when coupling the defect C=O stretching mode.

For this work, the conducting polymer was coupled to surface plasmons (SPs). We recall that SPs are formed from the coupling of the electromagnetic field with the collective electron oscillations of a metal. Since the momentum of SPs is larger than that of freely propagating light, specific conditions are required to attain momentum-matching. One way to optically excite SPs is to illuminate the metal surface through a dielectric prism which has a higher refractive index, thus increasing the momentum of light. The alternative option is to corrugate the metal surface with a periodic grating for attaining the coupling condition:

$$k_{sp} = k_0 \pm \boldsymbol{G} \qquad (5.1)$$

where the difference between the momentum of freely propagating light (k_0) and surface plasmons (k_{sp}) is matched through the reciprocal wavevector of the grating ($\boldsymbol{G}$).[150] In 1998, it was shown that transmission through a 2D periodic array of subwavelength holes can be strongly enhanced through the phenomenon of extraordinary optical transmission (EOT).[151] This triggered lot of research in plasmonics in the early 2000s, [123,152–161] some of which focused also on the 1D arrays of slits[161–166] – the simplified version of hole arrays. Since the metallic gratings are at the substrate – air interface, the SP resonant frequencies on both interfaces are detuned by the index difference. This asymmetry can be removed by the fabrication of samples with the dielectric - index matching.[156,167,168]

Recent works have shown the possibility of achieving momentum matching through periodic gratings in the mid-IR region,[169–174] but it is still difficult to achieve strong coupling conditions. Theoretical calculations done by Prof. Luis Martin-Moreno and his colleagues at the University of Zaragoza, showed that to obtain the SP modes with the required features for strong coupling it was not only important to have index matching but also have deep narrow slits. Such high contrast structures are hard to fabricate and we asked Prof. Sang Hyun-Oh and his group at the University of Minnesota, to help us. After several trials, plasmonic structures

with resonances having significantly improved Q (quality) factors reaching what is necessary for achieving VSC in the mid-IR were prepared and tested.

5.2. Experimental methods

5.2.1 System under study

For this experiment, an initial screening was carried out on many organic semiconductors to measure their transport properties under VSC. However, low conductivity (over large channel lengths) and poor film quality (for >1 μm thick films) limited the possibility of achieving the strong coupling condition and recording conductivity measurements for many of the candidates. The p-type semiconductor PEDOT: PSS, however, works well. Due to its high conductivity (0.4 to 4080 S/cm), PEDOT: PSS, developed at Bayers AG research lab in

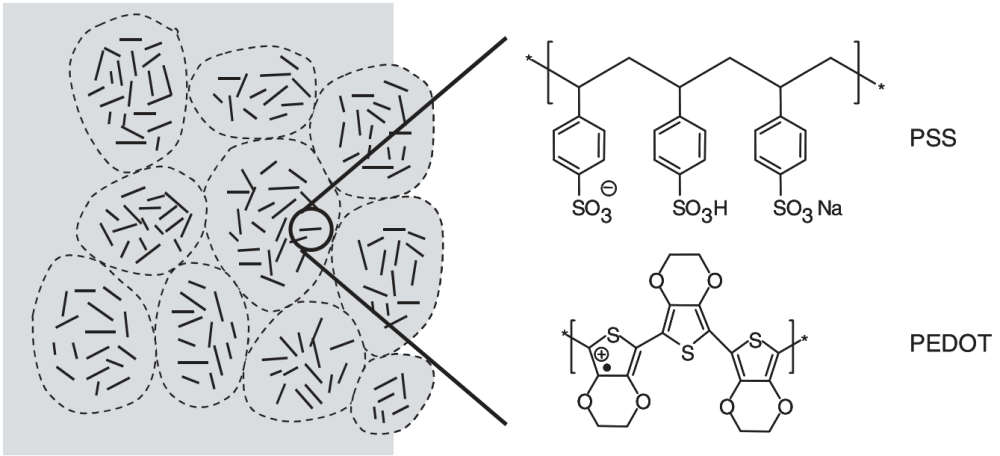

Figure 5.1. Schematic representation of the morphology and chemical structure of PEDOT: PSS. Reproduced from [175]

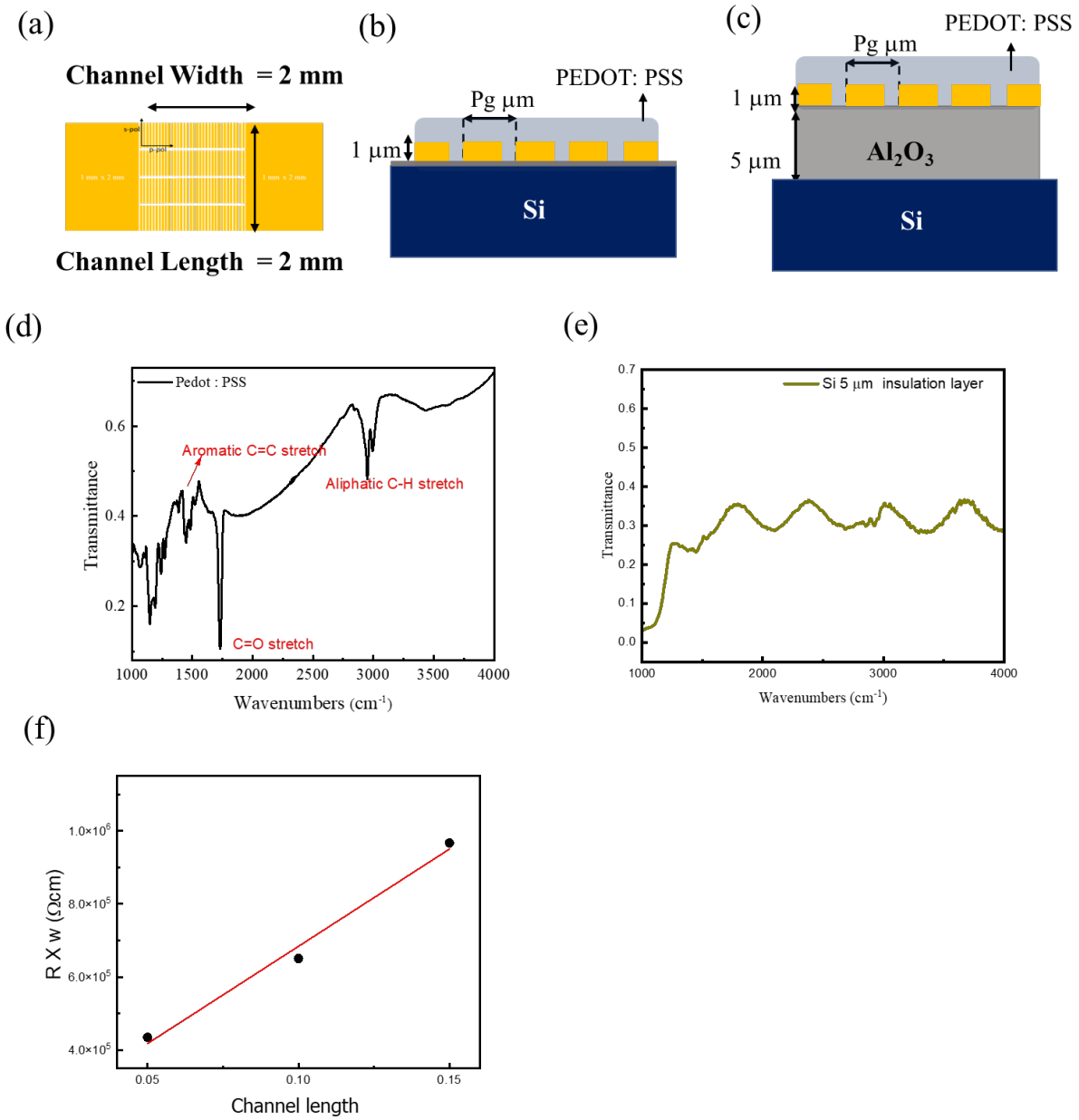

Figure 5.2. Top and side view of the devices. (a) Schematic representation of the configuration optimized for measuring the conductivity of organic semiconductor under VSC. Illustration of Au gratings on Si substrate with a (b) 50 nm insulation layer to avoid strong coupling condition and (c) thick layer of sapphire to achieve index matching. (d) FTIR spectrum of poly(3,4-ethylene dioxythiophene) polystyrene sulfonate (PEDOT: PSS), inset shows the chemical structure of PEDOT: PSS. (e) FTIR transmission spectra of Si substrates with 50 nm insulation layer and thick layer of Sapphire. (f) Plot of total resistance versus channel length measured for ~1.1 µm thick films of PEDOT: PSS spin-coated on thick (~5 µm) layer of sapphire.

Germany, has been used to make large electronic devices[176–181] The conductivity of the polymer depends on the PSS content, particle size distribution and the morphology of dried particles (or morphology of grains) in the film, the latter varies with respect to the annealing conditions.[175] The hole polaron transport into the PEDOT segments is not the only factor determining the electrical conductivity, but also their hopping between grains.[182] As thickness of the film increases, the polymer chains becomes disordered and the surface becomes rougher (low crystallinity).[183,184] Irreversible structural changes due to thermal annealing[182,185] or UV light[186] reduces the polymer chain length and decreases the conductivity. The C=O stretch, seen at 1728 cm^{-1} in the FTIR spectrum of the film (Figure 5.2 d), is due to the oxidation of polymer chain which reduces its conductivity. For our experiments, commercially available PEDOT: PSS solution (3.0 – 4.0% in H_2O, Sigma-Aldrich) was sonicated for 2 hours before spin-coating on the substrates. The spin-coated samples were then annealed at 105 °C in air for 5 minutes.[187]

5.2.2 Optimization of plasmonic gratings

Plasmonic structures are well suited for conductivity measurements (Figure 5.2 a) but it is difficult to achieve strong coupling conditions due to the broad SP dissipative resonances. Following the simulations discussed in the introduction, deep metal gratings (depth: 1 μm) were fabricated on double-sided polished Si wafers (Figure 5 b, c) using electron beam lithography (EBL) and their transmission spectra were recorded using the FTIR setup. At first, we measured the transmission spectra of the samples (shown in Figure 5.2 b), with gratings of different periodicity Pg (3.5, 4, 4.5, and 5 μm) fabricated on Si wafer with a thin 50 nm insulation layer. The lack of index matching in this first set resulted in poor quality plasmonic resonance, and so it was not possible to achieve strong coupling condition with the polymer.

The poor quality SP modes is not surprising when one recalls that the refractive index of Si in the mid-IR is around 3.4 and hence the index contrast is very large on the bare Si substrate.

To achieve strong coupling, index matching was obtained by sputtering a thick layer (5 μm) of sapphire (Al_2O_3) on the Si wafer, as detailed in the next paragraph, before depositing the metal and making the plasmonic structures. The refractive index of Al_2O_3 is around 1.6, a close match to the conducting polymer. Periodicity (Figure 5.2 c) was varied by changing metal strip-width and keeping the slit-width and depth constant. Figure 5.2 e shows the optical transparency of Si wafers in mid IR region with 5 μm thick insulation layers in the absence of gratings.

5.2.2.1. Deposition of thick layer of Al_2O_3

Deposition of Al_2O_3 above critical temperature leads to the blistering of the Al_2O_3 film due to the gaseous desorption on the surface. To avoid this, we have followed the procedure reported elsewhere.[188] The double-sided polished Si wafer is baked at 350 °C and then cooled down to room temperature. The passivation layer (50 nm of Al_2O_3 which inhibits the gaseous desorption from the surface) is then deposited on top of the Si wafer, through radio frequency sputtering in Plassys MP400S equipment. After a second annealing at 350 °C, Al_2O_3 was deposited for ~35 hours to achieve the desired thickness (~5 μm).

5.2.3 Electrical characterization of the samples

The 2-terminal device was electrically characterized using Cascade Microtech MPS-150 probe station equipped with micro-positioners to contact the electrode pads. The I-V curves were recorded by means of a Keithley 2636B source meter interfaced with Labtracer 2.0

software. The plots of total resistance (which is the product of the sample resistance, contact resistance and the channel width w) versus channel length measured for ~1.1 μm thick films of PEDOT: PSS spin-coated on substrates with ~5 μm thick insulation layer (i.e. in the absence of plasmonic structures) are shown in Figures 5.2 f. From such plots, the contact resistance and the sample resistance can be extracted.[189,190]

5.3 Results and discussions

5.3.1 Characterization of gratings

SEM images of gratings with periodicities (Pg) 3.5, 4 and 5 μm are shown in Figure 5.3 a-c. and the corresponding FTIR transmission spectra are shown in Figure 5.4 a, c and e. We

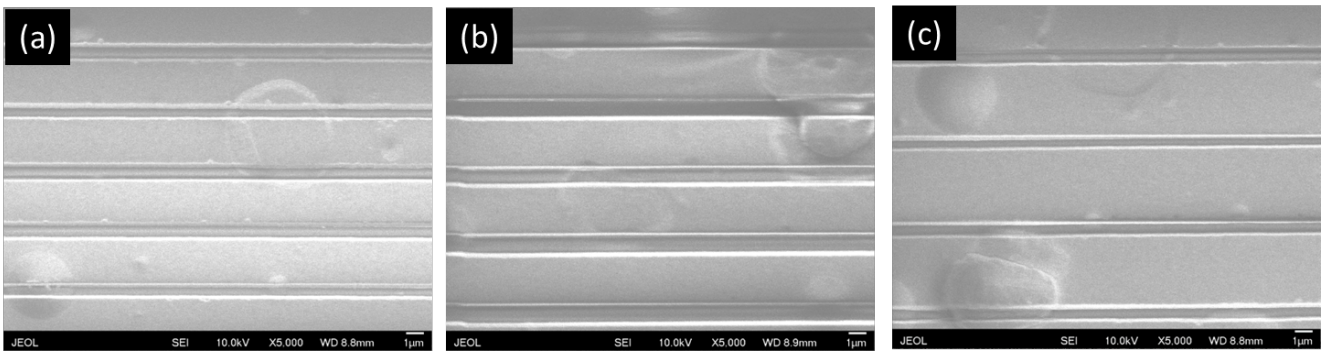

Figure 5.3. SEM images of gratings (fabricated on substrates with thick layer of sapphire) with Pg = (a) 3.5 μm, (b) 4 μm and (c) 5 μm.

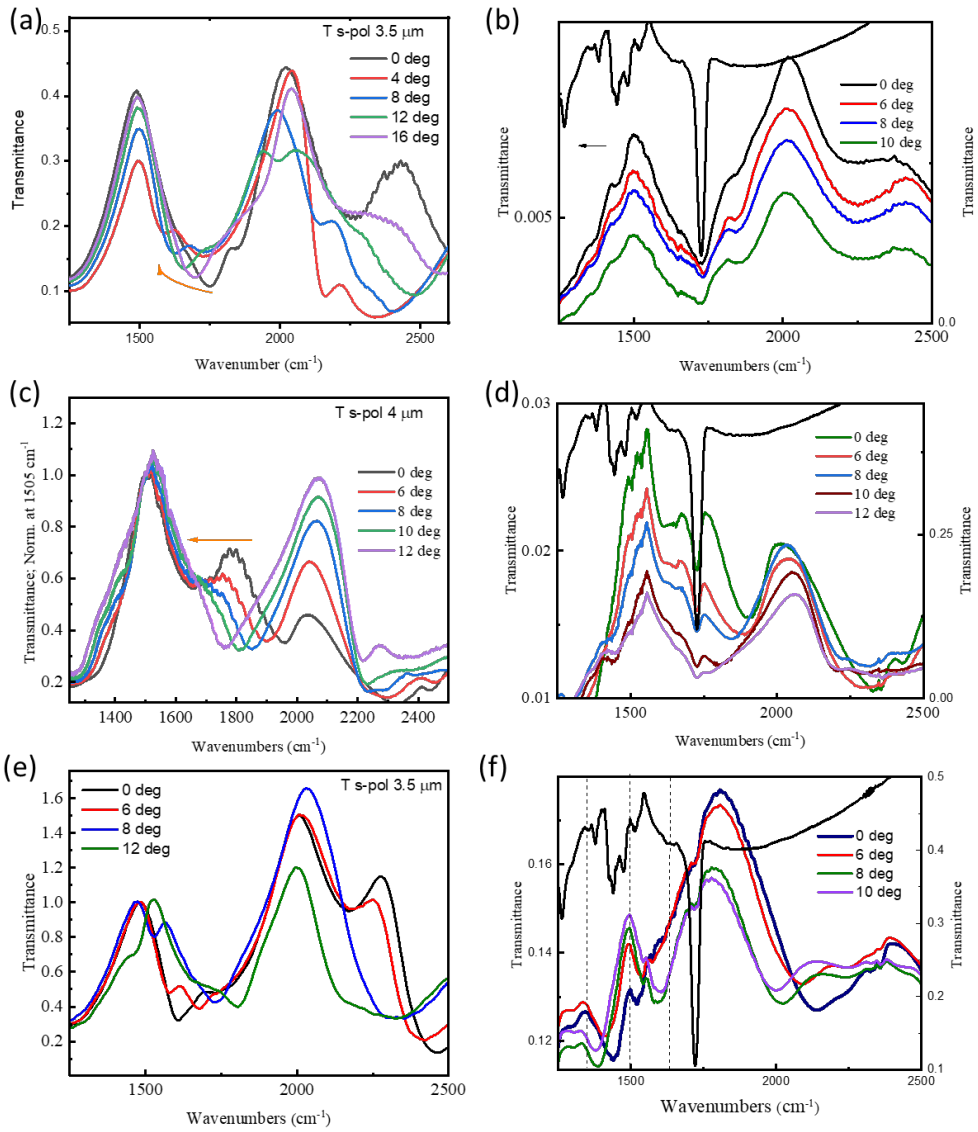

Figure 5.4. FTIR spectra of substrates with a thick (~5 μm) layer of sapphire**,** for Pg = 3.5, 4 and 5 μm, as a function of angle for both bare gratings (a, c and e) and coated ones with PEDOT : PSS film (b, d and f). The PEDOT:PSS is ~1.1 μm thick.

observed three sharp plasmonic resonances. The peaks around ~1500 and ~2000 cm^{-1} are non-dispersive while the third peak is dispersive (propagating surface plasmon) and varies with

the grating period (Pg = 3.5 μm - ~2400 cm^{-1}, Pg = 4 μm - ~2250 cm^{-1}, and Pg = 5 μm - ~1800 cm^{-1}). The non-dispersive peaks are probably due to slit modes which are formed due to the impedance mismatch between the slit gap and free space.[161] The samples with similar periodicities but varying slit-widths are being fabricated to confirm the nature of these modes. Figures 5.4 b, d and f shows the FTIR spectra of gratings spin-coated with ~1.1 μm thick PEDOT: PSS films. In Pg = 3.5 μm (Figure 5.4 b), the small peak at 1750 cm^{-1} is coupled (Rabi splitting ~ ca. 120 cm^{-1}) to the C=O stretch of the conducting polymer. C=O stretch of PEDOT: PSS is coupled to the dispersive plasmonic peak in gratings with Pg = 5 μm (Figure 5.4 d, Rabi splitting ~ ca. 83 cm^{-1}), while aromatic C=C stretch is coupled to the non-dispersive peak in Pg = 4 μm (Figure 5.4 f, Rabi splitting is ~ ca. 150 cm^{-1}).

5.3.3 Conductivity measurements

5.3.3.1 Pristine PEDOT: PSS

The conductivity of pristine PEDOT: PSS (processed through the method discussed above) is ca. 0.08 S/cm. This is smaller than that reported in the literature for a non-oxidized film. As discussed before, this is probably due to the oxidation of the film during processing.

5.3.3.2 PEDOT: PSS on gratings (~ 50 nm thin insulation layer)

Since it is not possible to achieve strong coupling condition with these gratings having ~50 nm thick insulation layer due to lack of index matching, it is not surprising that we do not see any change in the conductivity of PEDOT: PSS films (Figure 5.5 a) compared to the control sample (Red trace).

5.3.3.3 PEDOT: PSS on gratings (~ 5 µm thick insulation layer)

The current-voltage curves (Figure 5.5 b) are plotted as a function of the Pg of the metallic gratings. The black trace shows the I-V curve of PEDOT: PSS without coupling it to the gratings' plasmonic resonance, serves as control measurement. As discussed before, the calculated conductivity value (σ) of bare film (black trace) is lower than the literature reports.[191,192] Conductivity of PEDOT: PSS on bare gold film serves as additional control experiments, we observed a small increase in the conductivity of the conducting polymer on gold film. When the plasmonic resonance is coupled to different vibrational stretches of PEDOT: PSS film, as can be seen from Figure 5.5 b (green, blue, and red traces), conductivity of the polymer

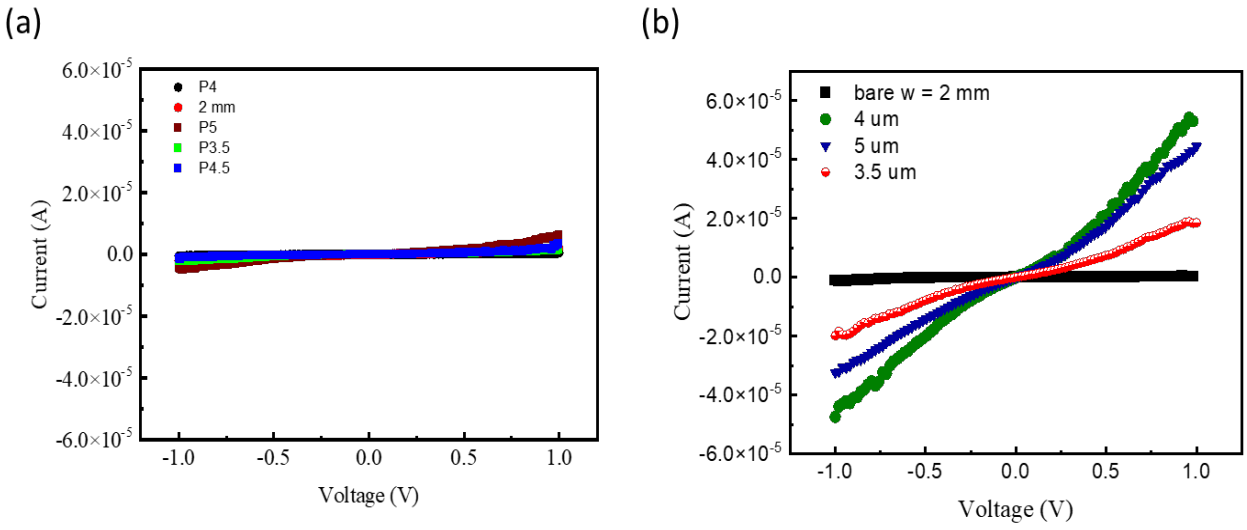

Figure 5.5. I-V curves of PEDOT: PSS as a function of periodicity of gratings. (a) 50 nm insulation layer. (b) ~5 µm thick Sapphire layer. (Black trace corresponds to the I-V curve of PEDOT: PSS in the absence of gratings. Red, blue and green correspond to the I-V curves of gratings with Pg = 3.5, 4 and 5 µm).

is enhanced. With the gratings Pg = 5 μm, the plasmonic resonance is coupled to the C=O stretch of PEDOT: PSS film. From the I-V curves (Figure 5.5, green trace), we can see that current is enhanced by a factor of ~60 and the calculated conductivity (σ) is 0.92 S/cm. An increase in current (blue and red traces) is also observed when the C=C stretch of the high conducting polymer is strongly coupled to the plasmonic resonance of gratings Pg =4 μm and the calculated conductivity value (σ) is 0.7 S/cm. With the gratings Pg = 3.5 μm, C=O stretch of the polymer is coupled to the non-dispersive peak and the calculated conductivity value (σ) is 0.3 S/cm.

5.4 Conclusion

The enhanced conductivity of PEDOT: PSS films under vibrational strong coupling indicates that even by coupling the vibrational transitions, one can enhance the transport properties of organic semiconductors. Interestingly coupling the defect C=O stretching mode restored the conductivity of the semiconductor. Such an enhancement in conductivity is probably due to the collective and coherent character of vibro-polaritonic states which might be helping the conducting polymer to overcome the defects. By defects, here we are referring to the oxidized films which shortens the conjugation and chain length and thus limits the hopping of charge carriers. Our results indicate that like ESC, VSC can also be used as a tool to improve the transport properties of organic semiconductors and probably other transport properties such as of excitons. To complete this work, further experiments are necessary to confirm the results and understand many of the details.

6.

CONCLUSION AND OUTLOOK

The possibility of large-scale synthesis, low cost, electronic tuning, room temperature stability, and many other advantages of organic semiconductors (OSCs), has triggered much research over the past 50 years because of the potential. Despite much improvement in their properties, large disorder and low mobility still limits their technological applications. Over the past decade, light-matter strong coupling has emerged as a powerful tool in modifying chemical and material properties. In such a coupling condition, the coherent collective states, P+, P- and DS extend over the mode volume[193] which can benefit transport properties which are normally limited by molecular disorder.[3–15] The main objective of this thesis was to understand and use light- matter strong coupling as a tool to enhance the charge carrier mobility of organic semiconductors.

In 2015, it was already shown that conductivity of n-type OSC can be enhanced by an order of magnitude under ESC and that the extended dark states play a key role.[4] This was extended to p-type organic semiconductors wherein charge transport occurs in the valence band, in the first part of this thesis, by studying the organic semiconductor- rr-P3HT. As discussed in the third Chapter, conductivity, and photoconductivity of rr-P3HT are enhanced

by factors of 3 and 6, respectively. Such an enhancement is again due to the collective character of polaritonic states. This is also evidence that even the ground state acquires some photonic character under ultra-strong coupling as predicted by theory years ago.[106,194]

Currently, we are coupling the electronic transitions of p-type organic semiconductors with different core structures – perylene and terylene, synthesized by our collaborators at the Université Libre de Bruxelles. This will give us further insight into the fundamentals of ESC on transport properties on organic semiconductors and will utilize strong coupling to tune the properties of organic semiconductors for various technological applications.

Since we already know that the vibrations have a significant role in the mobility of organic semiconductors, the main aim of this thesis was to study the transport properties of organic semiconductors under vibrational strong coupling, which had never been done. We have been approaching this problem using different configurations – Fabry Perot cavity and plasmonic structures. In the former configuration, we observed a huge drop in current under VSC. The spectroscopic and imaging studies following this observation confirmed that cooperative VSC modifies the morphology of supramolecular assemblies, a serendipitous observation. The morphology of conducting conjugated polymer -PPE formed amorphous flakes under coupled conditions, in contrary to the fibrous network formed outside the cavity. Following this experiment, the study and comparison of structural isomers of phenylene ethynylene indicated the role of symmetry and dipole moment on the effect of vibrational strong coupling on the assembly. Our results together with those at Hokkaido University,[58] indicate that light matter strong coupling can used as a new approach to modify supramolecular assemblies. Clearly, VSC drives the system through a different supramolecular landscape and modifies intermolecular interactions[58–60,85,89].

It is already known that solvents affect the energetic balance of supramolecular assemblies thus varying the population of various polymer states.[195] When solvents or

cosolvents have a structural role in assemblies, they can also play a direct role in the packing of organic systems. Since cooperative VSC modifies both the solute and solvent properties, VSC can be used as a tool to access the morphologies/different polymer states which are otherwise not thermodynamically stable. However, systematic experiments are required to understand the fundamentals and to control and manipulate supramolecular assemblies. Another future experiment could be to study if the system follows isodesmic or cooperative mechanism depending on the coupling conditions. Such experimental studies under isothermal condition is a challenge. Nevertheless, the recent report on automated tuning of cavity using piezoelectric actuators setup[196] shows a path to undertake such experiments.

Using the alternative configuration for achieving VSC – plasmonic structures, which is more compatible for conductivity measurements, we have coupled different vibrational bands of the conducting polymer- PEDOT: PSS. We observed an enhancement in the conductivity of the organic semiconductor by an order of magnitude when C=O peak is coupled to the plasmonic resonance of metallic gratings, as discussed in the Chapter 5. This indicates that the collective and coherent properties of vibro-polaritonic states also improves the transport properties and helps to overcome defects. VSC can also be used to understand the role of different vibrations in the mobility of organic semiconductors by coupling systematically different modes. At present, we are studying the effects of VSC on ionic liquid doped polymer gel by coupling the vibrational bands on ionic liquid to improve the efficiency of electrochemical field effect transistors.

The conductivity of organic semiconductors under strong coupling show a limited enhancement (~ order of magnitude) when coupled to the plasmonic resonances. This might be due to the finite propagation length of surface plasmons on metallic surfaces due to the dissipative nature of SPs. A recent study, where electronic transition is coupled to the Bloch waves of dielectric DBR mirrors, reported enhancement in diffusion coefficient by six orders

of magnitude and a transition from diffusion to ballistic transport under strong coupling.[15] Inspired from this study, we are currently optimizing the conditions to couple the vibrational mode to such a surface bound optical wave.

Light-matter strong coupling has emerged as a new frontier in science, it provides a novel approach to control and manipulate chemical and material properties. New findings have led to surprises about the consequences of coupling to the vacuum field. The technical implementation of strong coupling is quite simple and the fact that it can be achieved at room temperature, even in the absence of photons, opens a plethora of opportunities for applications. However, more detailed experiments and theory are required to understand the fundamental of strong coupling and to realize its full potential in different fields.

7.

RÉSUMÉ DE LA THESE

7.1 Introduction

La théorie de la mécanique quantique développée par Dirac, il y a près de cent ans, a posé les bases de l'électrodynamique quantique en cavité (cQED)[1], qui implique l'étude de l'interaction entre la matière et le champ électromagnétique confiné d'une cavité optique. Dans les années 1970, les études cQED se concentrait principalement sur les effets quantiques sur les atomes dans le régime perturbatif. Puis dans les années 1980 les propriétés optiques des semi-conducteurs en cavités ont suscité beaucoup d'intérêt, en particulier dans le régime dit de couplage fort. Depuis une douzaine d'année, la démonstration des effets très prononcés du couplage fort lumière-matière[2] sur les propriétés des matériaux et la chimie telles que la conductivité [3–9], la fonction de travail[10], l'optique non linéaire[11], la réactivité chimique[12-14] transferts d'énergie, [15-17] et le magnétisme[18] a surpris tout le monde surtout que ces modifications ont lieu même dans le noir. En effet, le couplage de l'absorption moléculaire et d'un mode optique conduit à la génération d'états hybrides lumière-matière, appelés états polaritoniques (Figure 1 a), se forment par l'interaction du l'énergie du point zéro de la transition moléculaire et celui de la cavité (appelé le champ électromagnétique du vide). De

plus dans ces états sont délocalisés sur de nombreuses molécules. En plus des états clairs (P+ et P-), des états noirs se forment également. Dans le régime de couplage fort, l'échange d'énergie entre les deux modes de résonance est plus rapide que

dans les processus de désintégration. Ce couplage est possible même dans l'obscurité grâce à l'interaction avec les énergies du point zéro du mode optique. En raison de la cohérence étendue et de la délocalisation des états hybrides lumière-matière, les propriétés de transport sont favorisées par un couplage fort.[3–9]

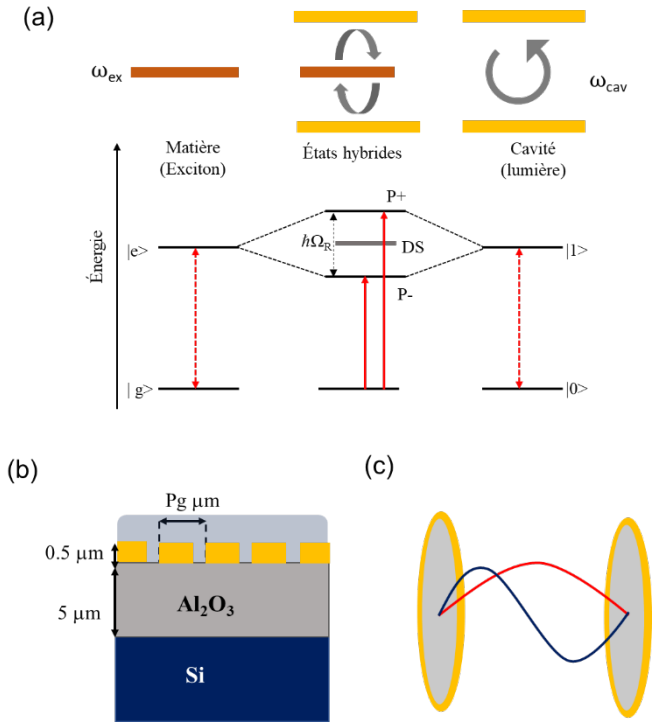

Figure 7.1. Illustration schématique de (a) couplage fort lumière-matière avec des états polaritoniques P+ et P- et des états noirs DS, (b) structures plasmoniques et (c) une cavité Fabry-Perot.

Les semi-conducteurs inorganiques conventionnels sont devenu omniprésents au cours du siècle dernier, dans diverses applications et depuis environ 50 ans on cherche à améliorer les semiconducteurs organiques (SCO) qui présentent de nombreux avantages pour la mise en

valeur technologique telles que leur faible coût et simplicité dans la fabrication de composants électroniques. Néanmoins, la faible mobilité et le grand désordre dans les SCO limitent leurs applications. La cohérence et la délocalisation des états polaritoniques offrent une possibilité pour surmonter cela. Dans cette thèse, nous avons étudié l'effet du couplage fort lumière-matière sur la conductivité des semi-

conducteurs organiques en couplant leurs transitions électroniques et vibrationnelles au mode électromagnétique résonant d'une cavité de Fabry-Pérot ou d'une structure plasmonique (Figure b, c).

7.2. Résultats et discussions

Dans la première partie de la thèse, nous avons étudié l'effet du couplage fort électronique (ESC) sur les propriétés de transport de charge en couplant la transition électronique du semi-conducteur de type p au mode optique des structures plasmoniques. Dans la deuxième partie, nous avons étudié l'effet du couplage fort vibrationnel (VSC) sur la conductivité des SCO à travers deux configurations différentes : la cavité de Fabry-Perot et les structures plasmoniques. Durant ces études, nous avons fait l'observation fortuite que l'assemblage supramoléculaire est modifié par le VSC qui a donné lieu à deux articles.

7.2.1 Couplage fort dans la région UV-visible

En 2015, George et al. ont montré que la conductivité de SCO de type *n* peut être améliorée en couplant fortement la transition électronique aux modes plasmoniques transformant la bande de conduction en deux états hybrides lumière-matière (P+ et P-).[4]

Cependant, l'effet du couplage fort électronique sur la conductivité des semi-conducteurs organiques de type *p* dans lesquels le transport

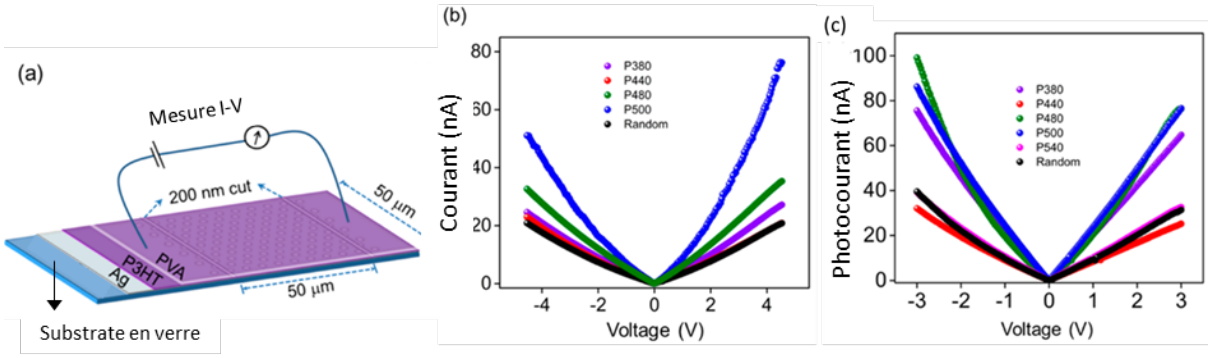

Figure 7.2. (a) Représentation schématique utilisée pour les mesures de conductivité sous ESC (b) Courbes I-V de rr-P3HT en fonction de la périodicité des réseaux de trous, (c) Courbes I-V de rr-P3HT en fonction de la périodicité des réseaux de trous sous illumination visible. Reproduit de la réf [197].

de charge (les trous sont les porteurs majoritaires) se produit dans la bande de valence, n'avait pas été exploré. On sait par des études théoriques que si le couplage fort est suffisamment fort, l'état fondamental acquiert un caractère photonique et on peut donc s'attendre à un effet sur la conduction par la bande valence.

Alors nous avons étudié les propriétés de transport du poly-(3-hexylthiophène) régio-régulier (rr-P3HT), un SCO type *p* sous couplage électronique fort (ESC). La transition électronique de P3HT est fortement couplée à la résonance plasmonique des réseaux de trous dans lesquels le mode optique peut être réglé en modifiant la périodicité (P) des réseaux. Pour rr-P3HT la séparation de Rabi (entre P+ et P-) est d'environ ~0,6 eV à résonance, ce qui correspond à 27 % de l'énergie de transition, ce qui implique que le système est dans l'ultra- régime de couplage fort. Comme on peut le voir sur la figure 2b, le courant est amélioré dans des conditions de couplage (trace bleue), un réseau de trous aléatoire sert de mesure de référence. De plus,

puisque la photoconductivité bénéficie de l'amélioration de la conductivité, elle est également améliorée par un facteur de 3.

L'amélioration des propriétés de transport du SCO de type *p* confirme que le couplage ultra-fort induit un caractère polaritonique dans la bande de valence.

7.2.2 Couplage fort dans la région IR moyen (VSC)

Comme mentionné précédemment, nous avons exploré deux configurations différentes : une cavité Fabry-Perot (FP) et des structures plasmoniques, pour coupler les modes vibrationnels dans l'IR (VSC). En étudiant les propriétés de transport des assemblages supramoléculaires d'un polymère conducteur dans la première configuration, nous avons observé un effet drastique sur le processus d'auto-assemblage du polymère, une observation fortuite.[19] Nous avons également étudié les isomères structuraux du phénylène éthynylène (PE) pour comprendre l'influence de la symétrie sur l'effet du couplage fort VSC sur l'organisation supramoléculaire comme décrit dans le paragraphe suivant.[20] En parallèle, nous avons étudié cette dernière architecture qui est plus compatible pour mesurer la conductivité mais qui souffre d'avoir de larges résonances dissipatives. Nous avons optimisé les structures plasmoniques avec des résonances ayant des facteurs Q (qualité) considérablement améliorés se rapprochant de ce qui est nécessaire pour atteindre la VSC dans l'IR moyen. Lorsque différentes bandes vibrationnelles de polymère hautement conducteur : poly(3,4-éthylènedioxythiophène) sulfonate de polystyrène (PEDOT : PSS) sont couplées à la résonance plasmonique, nous constatons une amélioration de la conductivité.

7.2.2.1 VSC en cavité Fabry-Pérot

Pour les besoins de notre étude, nous avons sélectionné le poly(para-phénylèneéthynylène, PPE) substitué par dinonanoyloxy qui est un polymère conjugué classique. Le comportement de gélification des PPE avec des chaînes latérales alkyle ou alcoxy a été bien étudié.[21] L'objectif initial étant d'étudier l'effet des VSC sur les propriétés de transport du gel, les modes vibrationnels moléculaires ont été fortement couplés au mode optique de la cavité de Fabry-Perot par effet coopératif. Lors des mesures de conductivité du gel PPE sous

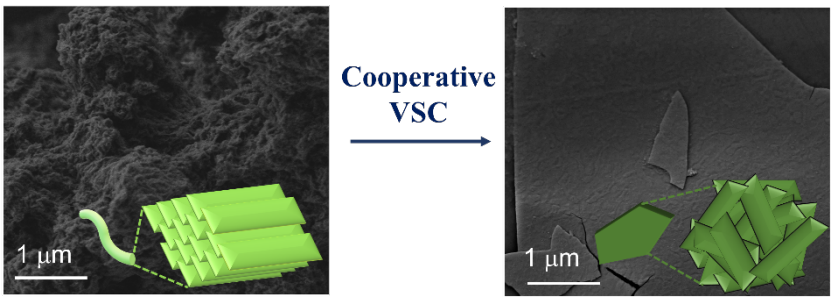

Figure 7.3. Modification de la morphologie de l'assemblage supramoléculaire PPE sous couplage vibrationnel fort coopératif. Reproduit de la réf [59].

VSC, nous avons observé une énorme chute de courant. Une analyse plus approfondie par des études d'absorption et de fluorescence a révélé que l'auto-assemblage et l'organisation supramoléculaire du PPE avait probablement été modifiés sous VSC. Ceci a été confirmé par des images de microscopie électronique (Figure 3) où on peut voir que le gel fibreux est transformé en flocons amorphes sous VSC.

En plus des expériences sur le PPE, nous avons pu voir le rôle de la symétrie dans l'influence de l'effet de couplage fort lumière-matière en étudiant deux isomères structuraux de molécules organiques conjuguées - - phénylène éthynylène (PE) linéaire (PE1) et courbé (PE2). Les bandes vibrationnelles des isomères sont fortement couplées au mode optique de la cavité

de Fabry-Perot par effet coopératif. Les spectres d'absorption et de fluorescence ont révélé que le VSC induit des changements drastiques dans le processus d'auto-assemblage mais seulement pour l'isomère PE2 (Figure 4).

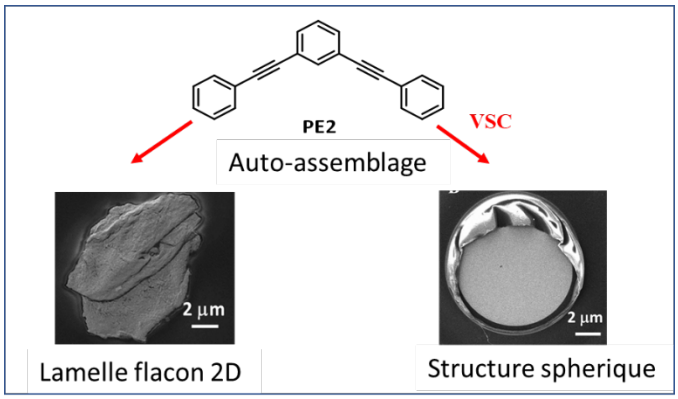

Figure 7.4. Modification de la morphologie de l'assemblage supramoléculaire PE sous couplage vibrationnel fort coopératif. Reproduit de la réf [60].

Les effets très différents du VSC sur PE1 ($D_{\infty h}$, molécule linéaire) et PE2 (C_{2v}, molécule coudée) confirme l'influence de la symétrie sur l'effet du couplage fort lumière-matière.

7.2.2.2 Structures plasmoniques

La configuration alternative pour étudier les mesures de conductivité sous VSC est celle des structures plasmoniques - réseaux métalliques (Figure 5 a). Même si les structures plasmoniques sont plus compatibles pour les mesures de conductivité, il est difficile d'obtenir des conditions de couplage

fortes dans l'IR en raison des larges résonances dissipatives. Pour surmonter cela, nous avons adapté le concept de « index matching ». À cette fin, une couche épaisse de saphir a été évaporée sur des tranches de silicium polies double face pour mesurer les spectres de transmission infrarouge à transformée de Fourier (FTIR). Des réseaux métalliques profonds

(profondeur : 1 µm) ont été fabriqués sur de tels substrats en utilisant la technique - lithographie par faisceau d'électrons (EBL) et leurs spectres de transmission ont été enregistrés en utilisant la configuration FTIR. La périodicité (Pg, figure 6) est modifiée en faisant varier la largeur de la bande métallique à largeur de fente constante. Les courbes courant-tension (figure 5 b) sont tracées en fonction de la périodicité des réseaux métalliques. La courbe noire sur la figure 5 b montre la courbe I-V de PEDOT : PSS sans couplage qui sert de référence. Lorsque la résonance plasmonique est couplée à différentes vibrations de PEDOT : film PSS, la conductivité du polymère est améliorée figure 5b (courbes vertes, bleues et rouges).

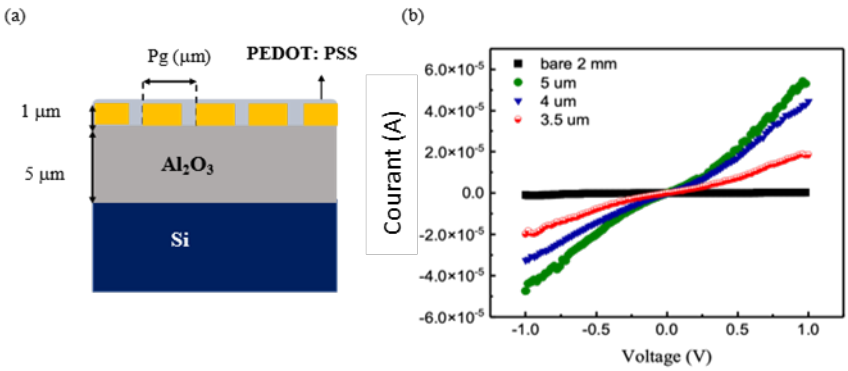

Figure 7.5 (a) Illustration schématique du dispositif avec des structures plasmoniques spin-coated avec PEDOT : PSS (b) Courbes I-V en fonction de la périodicité des réseaux. La courbe noire correspond à la courbe I-V de PEDOT : PSS en l'absence de réseaux.

7.3. Conclusion générale

Dans cette thèse, nous avons exploré l'effet du couplage fort électronique et vibrationnel sur la conductivité des semi-conducteurs organiques, étudiant ainsi l'amélioration du transport

de charge due à la cohérence étendue et à la délocalisation des états hybrides lumière-matière. La conductivité et la photoconductivité du semi-conducteur de type *p* étant améliorées, les résultats confirment que le caractère polaritonique est induit même dans la bande de valence sous un couplage ultra-fort. L'amélioration de la conductivité du PEDOT : PSS sous VSC montre pour la première fois que le VSC peut induire des états collectifs étendus qui influent sur le transport. Ainsi le couplage fort au champ du vide par ESC et VSC ouvrent des perspectives prometteuses pour améliorer la conductivité des semi-conducteurs organiques. De plus nous avons montré que le VSC peut servir à modifier les assemblages supramoléculaires, apportant ainsi un nouvel outil pour contrôler l'organisation de la matière.

BIBLIOGRAPHY

1. Dirac, P. A. M. The quantum theory of emission and absorption of radiation. *Proc. R. Soc. Lond. A* **114**, 243–265 (1927).
2. Garcia-Vidal, F. J., Ciuti, C. & Ebbesen, T. W. Manipulating matter by strong coupling to vacuum fields. *Science* **373**, No. eabd0336 (2021).
3. Nagarajan, K. *et al.* Conductivity and Photoconductivity of a p-Type Organic Semiconductor under Ultrastrong Coupling. *ACS Nano* **14**, 10219–10225 (2020).
4. Orgiu, E. *et al.* Conductivity in organic semiconductors hybridized with the vacuum field. *Nat. Mater.* **14**, 1123–1129 (2015).
5. Lerario, G. *et al.* High-speed flow of interacting organic polaritons. *Light Sci. Appl.* **6**, e16212-6 (2017).
6. Zakharko, Y. *et al.* Radiative pumping and propagation of plexcitons in diffractive plasmonic crystals. *Nano Lett.* **18**, 4927–4933 (2018).
7. Pandya, R. *et al.* Microcavity-like exciton-polaritons can be the primary photoexcitation in bare organic semiconductors. *Nat. Commun.* **12**, 1–11 (2021).
8. Hagenmüller, D., Schachenmayer, J., Schütz, S., Genes, C. & Pupillo, G. Cavity-enhanced transport of charge. *Phys. Rev. Lett.* **119**, 223601 (2017).
9. Krainova, N., Grede, A. J., Tsokkou, D., Banerji, N. & Giebink, N. C. Polaron photoconductivity in the weak and strong light-matter coupling regime. *Phys. Rev. Lett.* **124**, 177401 (2020).
10. Bhatt, P., Kaur, K. & George, J. Enhanced charge transport in two-dimensional materials through light-matter strong coupling. *ACS Nano* **15**, 13616–13622 (2021).
11. Zeng, P. *et al.* Photoinduced electron transfer in the strong coupling regime: Waveguide-plasmon polaritons. *Nano Lett.* **16**, 2651–2656 (2016).

12. Feist, J. & Garcia-Vidal, F. J. Extraordinary exciton conductance induced by strong coupling. *Phys. Rev. Lett.* **114**, 196402 (2015).

13. Schachenmayer, J., Genes, C., Tignone, E. & Pupillo, G. Cavity-enhanced transport of excitons. *Phys. Rev. Lett.* **114**, 196403 (2015).

14. Pandya, R. *et al.* Tuning the coherent propagation of organic exciton-polaritons through dark state delocalization. *Adv. Sci.* **9**, 2105569 (2022).

15. Balasubrahmaniyam, M., Simkovich, A., Golombek, A., Ankonina, G. & Schwartz, T. Unveiling the mixed nature of polaritonic transport: From enhanced diffusion to ballistic motion approaching the speed of light. *arXiv Prepr. arXiv2205.06683* (2022).

16. Hutchison, J. A. *et al.* Tuning the work-function via strong coupling. *Adv. Mater.* **25**, 2481–2485 (2013).

17. Wang, K. *et al.* Large optical nonlinearity enhancement under electronic strong coupling. *Nat. Commun.* **12**, 1486 (2021).

18. Thomas, A. *et al.* Ground state chemistry under vibrational strong coupling: Dependence of thermodynamic parameters on the Rabi splitting energy. *Nanophotonics* **9**, 249–255 (2020).

19. Lather, J., Bhatt, P., Thomas, A., Ebbesen, T. W. & George, J. Cavity catalysis by cooperative vibrational strong coupling of reactant and solvent molecules. *Angew. Chemie Int. Ed.* **58**, 10635–10638 (2019).

20. Nagarajan, K., Thomas, A. & Ebbesen, T. W. Chemistry under vibrational strong coupling. *J. Am. Chem. Soc.* **143**, 16877–16889 (2021).

21. Ahn, W., Herrera, F. & Simpkins, B. S. Modification of urethane addition reaction via vibrational strong coupling. *ChemRxiv 10.26434/chemrxiv-2022-wb6vs* (2022).

22. Thomas, A. *et al.* Tilting a ground-state reactivity landscape by vibrational strong coupling. *Science* **363**, 615–619 (2019).

23. Thomas, A. *et al.* Large enhancement of ferromagnetism under a collective strong coupling of YBCO nanoparticles. *Nano Lett.* **21**, 4365–4370 (2021).

24. Planck, M. Zur Theorie des Gesetzes der Energieverteilung im Normalspektrum. *Verhandlungen der Deutschen Physikalischen Gesselschaft* vol. 2 237–245 (1900).

25. Einstein, A. Zur Quantentheorie der Strahlung. *Physik* **18**, 121 (1917).

26. Bohr, N. Part II . – Systems containing only a single Nucleus. *Philos. Mag.* **26**, (1913).

27. Fermi, E. Quantum theory of radiation. *Rev. Mod. Phys.* **4**, 127–183 (1932).

28. Lamb, W. E. & Retherford, R. C. Fine structure of the hydrogen atom by a microwave method. *Phys. Rev.* **72**, 241–243 (1947).

29. Purcell, E. M., Torrey, H. C., Pound, R. V. Resonance absorption by nuclear magnetic moments in a solid. *Phys. Rev* **69**, 37–38 (1946).

30. Purcell, E. M. Spontaneous emission probabilities at radio frequencies. *Confin. Electrons Photons.* **Springer,** 839 (1995).

31. Drexhage, K. H. IV Interaction of light with monomolecular dye layers. *Prog. Opt.* **12**, 163–232 (1974).

32. Pockrand, I., Brillante, A. & Möbius, D. Exciton-surface plasmon coupling: An experimental investigation. *J. Chem. Phys.* **77**, 6289–6295 (1982).

33. Drexhage, K. H., Kuhn, H., Schäfer, F. P. Variation of the fluorescence decay time of a molecule in front of a mirror. *Ber.Bunsenges. Phys. Chem.* **72**, 329 (1968).

34. Kleppner, D. Inhibited spontaneous emission. *Phys. Rev. Lett.* **47**, 233–236 (1981).

35. Amos, R. M. & Barnes, W. L. Modification of the spontaneous emission rate of Eu 3+ ions close to a thin metal mirror. *Phys. Rev. B* **55**, 7249–7254 (1997).

36. V. Agranovich and A. Malshukov. Surface polariton spectra if the resonance with the transition layer vibrations exist. *Opt. Commun.* **11**, 169–171 (1974).

37. Yakovlev, V. A., Nazin, V. G. & Zhizhin, G. N. The surface polariton splitting due to

thin surface film LO vibrations. *Opt. Commun.* **15**, 293–295 (1975).

38. Haroche, S. & Kleppner, D. Quantum cavity electrodynamics. *Phys. Today* **42**, 24–30 (1989).

39. Kaluzny, Y., Goy, P., Gross, M., Raimond, J. M. & Haroche, S. Observation of self-induced Rabi oscillations in two-level atoms excited inside a resonant cavity: The ringing regime of superradiance. *Phys. Rev. Lett.* **51**, 1175–1178 (1983).

40. Rempe, G., Walther, H. & Klein, N. Observation of quantum collapse and revival in a one-atom maser. *Phys. Rev. Lett.* **58**, 353–356 (1987).

41. Raizen, M. G., Thompson, R. J., Brecha, R. J., Kimble, H. J. & Carmichael, H. J. Normal-mode splitting and linewidth averaging for two-state atoms in an optical cavity. *Phys. Rev. Lett.* **63**, 240–243 (1989).

42. Thompson, R. J., Rempe, G. & Kimble, H. J. Observation of normal-mode splitting for an atom in an optical cavity. *Phys. Rev. Lett.* **68**, 1132–1135 (1992).

43. Haroche, S. & Raimond, J. M. Exploring the quantum: Atoms, cavities, and photons. *Oxford Univ. Press* (2006).

44. Weisbuch, C., Nishioka, M., Ishikawa, A. & Arakawa, Y. Observation of the coupled exciton-photon mode splitting in a semiconductor quantum microcavity. *Phys. Rev. Lett.* **69**, 3314–3317 (1992).

45. Canaguier-Durand, A., Genet, C., Lambrecht, A., Ebbesen, T. W. & Reynaud, S. Non-Markovian polariton dynamics in organic strong coupling. *Eur. Phys. J. D* **69**, (2015).

46. Houdré, R. Early stages of continuous wave experiments on cavity-polaritons. *Phys. Status Solidi Basic Res.* **242**, 2167–2196 (2005).

47. Houdré, R. *et al.* Measurement of cavity polariton dispersion curve. *Superlattices Microstruct.* **15**, 263 (1994).

48. Baumberg, J. J. *et al.* Parametric oscillation in a vertical microcavity: A polariton

condensate or micro-optical parametric oscillation. *Phys. Rev. B* **62**, R16247–R16250 (2000).

49. Weihs, G., Deng, H., Snoke, D. & Yamamoto, Y. Polariton lasing in a microcavity. *Phys. Status Solidi Appl. Res.* **201**, 625–632 (2004).

50. Imamoglu, A., Ram, R. J., Pau, S. & Yamamoto, Y. Nonequilibrium condensates and lasers without inversion: Exciton-polariton lasers. *Phys. Rev. A - At. Mol. Opt. Phys.* **53**, 4250–4253 (1996).

51. Dietrich, C. P. *et al.* An exciton-polariton laser based on biologically produced fluorescent protein. *Sci. Adv.* **2**, 1–8 (2016).

52. Ünlü, M. S. & Strite, S. Resonant cavity enhanced photonic devices. *J. Appl. Phys.* **78**, 607–639 (1995).

53. Fujita, T., Sato, Y., Kuitani, T. & Ishihara, T. Tunable polariton absorption of distributed feedback microcavities at room temperature. *Phys. Rev. B - Condens. Matter Mater. Phys.* **57**, 12428–12434 (1998).

54. Lidzey, D. G. *et al.* Strong exciton-photon coupling in an organic semiconductor microcavity. *Nature* **395**, 53–55 (1998).

55. Hobson, P. A. *et al.* Strong exciton-photon coupling in a low-Q all-metal mirror microcavity. *Appl. Phys. Lett.* **81**, 3519–3521 (2002).

56. Dintinger, J., Klein, S., Bustos, F., Barnes, W. L. & Ebbesen, T. W. Strong coupling between surface plasmon-polaritons and organic molecules in subwavelength hole arrays. *Phys. Rev. B* **71**, 1–5 (2005).

57. Bellessa, J., Bonnand, C., Plenet, J. C. & Mugnier, J. Strong coupling between surface plasmons and excitons in an organic semiconductor. *Phys. Rev. Lett.* **93**, 3–6 (2004).

58. Hirai, K., Ishikawa, H., Chervy, T., Hutchison, J. A. & Uji-i, H. Selective crystallization via vibrational strong coupling. *Chem. Sci.* **12**, 11986–11994 (2021).

59. Joseph, K. *et al.* Supramolecular assembly of conjugated polymers under vibrational strong coupling. *Angew. Chemie - Int. Ed.* **60**, 19665–19670 (2021).

60. Kulangara, S. *et al.* Manipulating the self-assembly of phenyleneethynylenes under vibrational strong coupling. *J. Phys. Chem. Lett.* **13**, 1209–1214 (2022).

61. Fukushima, T., Yoshimitsu, S. & Murakoshi, K. Inherent promotion of ionic conductivity via collective vibrational strong coupling of water with the vacuum electromagnetic field. *J. Am. Chem. Soc.* **144**, 12177–12183 (2022).

62. Hutchison, J. A., Schwartz, T., Genet, C., Devaux, E. & Ebbesen, T. W. Modifying chemical landscapes by coupling to vacuum fields. *Angew. Chemie - Int. Ed.* **51**, 1592–1596 (2012).

63. Wang, S. *et al.* Phase transition of a perovskite strongly coupled to the vacuum field. *Nanoscale* **6**, 7243–7248 (2014).

64. Zhong, X. *et al.* Energy transfer between spatially separated entangled molecules. *Angew. Chemie* **129**, 9162–9166 (2017).

65. Hou, S. *et al.* Ultralong-range energy transport in a disordered organic semiconductor at room temperature via coherent exciton-polariton propagation. *Adv. Mater.* **32**, 2002127 (2020).

66. Zhong, X. *et al.* Non-radiative energy transfer mediated by hybrid light-matter states. *Angew. Chemie* **128**, 6310–6314 (2016).

67. Akulov, K., Bochman, D., Golombek, A. & Schwartz, T. Long-distance resonant energy transfer mediated by hybrid plasmonic-photonic modes. *J. Phys. Chem. C* **122**, 15853–15860 (2018).

68. Coles, D. M. *et al.* Polariton-mediated energy transfer between organic dyes in a strongly coupled optical microcavity. *Nat. Mater.* **13**, 712–719 (2014).

69. Coles, D. M. *et al.* Strong coupling between chlorosomes of photosynthetic bacteria and

a confined optical cavity mode. *Nat. Commun.* **5**, 1–9 (2014).

70. Nagarajan, K. *et al.* Conductivity and photoconductivity of a p-type organic semiconductor under ultrastrong coupling. *ACS Nano* **14**, 10219–10225 (2020).

71. George, J., Shalabney, A., Hutchison, J. A., Genet, C. & Ebbesen, T. W. Liquid-phase vibrational strong coupling. *J. Phys. Chem. Lett.* **6**, 1027–1031 (2015).

72. Shalabney, A. *et al.* Coherent coupling of molecular resonators with a microcavity mode. *Nat. Commun.* **6**, 1–6 (2015).

73. Thomas, A. *et al.* Ground-State chemical reactivity under vibrational coupling to the vacuum electromagnetic field. *Angew. Chemie - Int. Ed.* **55**, 11462–11466 (2016).

74. Schäfer, C., Flick, J., Ronca, E., Narang, P. & Rubio, A. Shining light on the microscopic resonant mechanism responsible for cavity-mediated chemical reactivity. *arXiv Prepr. arXiv2104.12429.* (2021).

75. Hirai, K., Takeda, R., Hutchison, J. A. & Uji-i, H. Modulation of Prins cyclization by vibrational strong coupling. *Angew. Chemie - Int. Ed.* **59**, 5332–5335 (2020).

76. Hiura, H. & Shalabney, A. Vacuum-field catalysis: accelerated reactions by vibrational ultra strong coupling. *ChemRxiv 10.26434/chemrxiv.7234721.v4* (2018) doi:10.26434/chemrxiv.7234721.

77. Lather, J., Thabassum, A. N. K., Singh, J. & George, J. Cavity catalysis: modifying linear free-energy relationship under cooperative vibrational strong coupling. *Chem. Sci.* **13**, 195–202 (2022).

78. Lather, J. & George, J. Improving enzyme catalytic efficiency by cooperative vibrational strong coupling of water. *J. Phys. Chem. Lett.* **12**, 379–384 (2021).

79. Vergauwe, R. M. A. *et al.* Modification of enzyme activity by vibrational strong coupling of water. *Angew. Chemie Int. Ed.* **58**, 15324–15328 (2019).

80. Pang, Y. *et al.* On the role of symmetry in vibrational strong coupling: The case of

charge-transfer complexation. *Angew. Chemie* **132**, 10522–10526 (2020).

81. Schütz, S. *et al.* Ensemble-induced strong light-matter coupling of a single quantum emitter. *Phys. Rev. Lett.* **124**, 113602 (2020).

82. Li, T. E., Nitzan, A. & Subotnik, J. E. Collective vibrational strong coupling effects on molecular vibrational relaxation and energy transfer: Numerical insights via cavity molecular dynamics simulations. *Angew. Chemie* **133**, 15661–15668 (2021).

83. Xiang, B. *et al.* Intermolecular vibrational energy transfer enabled by microcavity strong light–matter coupling. *Science* **368**, 665–667 (2020).

84. Sau, A. *et al.* Modifying wWoodward–Hoffmann stereoselectivity under vibrational strong coupling. *Angew. Chemie* **133**, 5776–5781 (2021).

85. Haugland, T. S., Schäfer, C., Ronca, E., Rubio, A. & Koch, H. Intermolecular interactions in optical cavities: An ab initio QED study. *J. Chem. Phys.* **154**, (2021).

86. Li, T. E., Nitzan, A., Hammes-Schiffer, S. & Subotnik, J. E. Quantum simulations of vibrational strong coupling via path integrals. *J. Phys. Chem. Lett.* **13**, 3890–3895 (2022).

87. Li, T. E., Nitzan, A. & Subotnik, J. E. Cavity molecular dynamics simulations of vibrational polariton-enhanced molecular nonlinear absorption. *J. Chem. Phys.* **154**, (2021).

88. Fischer, E. W. & Saalfrank, P. Ground state properties and infrared spectra of anharmonic vibrational polaritons of small molecules in cavities. *J. Chem. Phys.* **154**, 104311 (2021).

89. Li, T. E., Subotnik, J. E. & Nitzan, A. Cavity molecular dynamics simulations of liquid water under vibrational ultrastrong coupling. *Proc. Natl. Acad. Sci. U. S. A.* **117**, 18324–18331 (2020).

90. Phuc, N. T., Trung, P. Q. & Ishizaki, A. Controlling the nonadiabatic electron-transfer

reaction rate through molecular-vibration polaritons in the ultrastrong coupling regime. *Sci. Rep.* **10**, 1–11 (2020).

91. Li, X., Mandal, A. & Huo, P. Cavity frequency-dependent theory for vibrational polariton chemistry. *Nat. Commun.* **12**, 1–9 (2021).
92. Galego, J., Climent, C., Garcia-Vidal, F. J. & Feist, J. Cavity Casimir-Polder forces and their effects in ground-state chemical reactivity. *Phys. Rev. X* **9**, 1–22 (2019).
93. Flick, J., Schäfer, C., Ruggenthaler, M., Appel, H. & Rubio, A. Ab Initio optimized effective potentials for real molecules in optical cavities: Photon contributions to the molecular ground state. *ACS Photonics* **5**, 992–1005 (2018).
94. Ruggenthaler, M. *et al.* Quantum-electrodynamical density-functional theory: Bridging quantum optics and electronic-structure theory. *Phys. Rev. A* **90**, 1–26 (2014).
95. Li, T. E., Nitzan, A. & Subotnik, J. E. Polariton relaxation under vibrational strong coupling: Comparing cavity molecular dynamics simulations against Fermi's golden rule rate. *J. Chem. Phys.* **156**, (2022).
96. Jaynes, E. T. & Cummings, F. W. Comparison of quantum and semiclassical radiation theories with application to the beam Maser. *Proc. IEEE* **51**, 89–109 (1963).
97. Tavis, M. & Cummings, F. W. Exact solution of an N-molecule-radiation-field Hamiltonian. *Phys. Rev.* **170**, 379–384 (1968).
98. Zeb, M. A., Kirton, P. G. & Keeling, J. Exact states and spectra of vibrationally dressed polaritons. *ACS Photonics* **5**, 249–257 (2018).
99. Cwik, J. A., Kirton, P., De Liberato, S. & Keeling, J. Excitonic spectral features in strongly coupled organic polaritons. *Phys. Rev. A* **93**, 1–12 (2016).
100. Feist, J., Galego, J. & Garcia-Vidal, F. J. Polaritonic chemistry with organic molecules. *ACS Photonics* **5**, 205–216 (2018).
101. González-Tudela, A., Huidobro, P. A., Martín-Moreno, L., Tejedor, C. & García-Vidal,

F. J. Theory of strong coupling between quantum emitters and propagating surface plasmons. *Phys. Rev. Lett.* **110**, 1–5 (2013).

102. Wang, S. Strong light-molecule coupling : routes to new hybrid materials. *Ph.D. Diss. Univ. Strasbg.* (2015).

103. Bhatt, P., Dutta, J. & George, J. Electromagnetic field dependence of strong coupling in WS2 monolayers. *Phys. Status Solidi - Rapid Res. Lett.* **15**, 1–7 (2021).

104. Wang, S. *et al.* Coherent coupling of WS2 monolayers with metallic photonic nanostructures at room temperature. *Nano Lett.* **16**, 4368–4374 (2016).

105. Scholes, G. D., Delpo, C. A. & Kudisch, B. Entropy reorders polariton states. *J. Phys. Chem. Lett.* **11**, 6389–6395 (2020).

106. Ciuti, C., Bastard, G. & Carusotto, I. Quantum vacuum properties of the intersubband cavity polariton field. *Phys. Rev. B* **72**, 115303 (2005).

107. Oberhofer, H., Reuter, K. & Blumberger, J. Charge Transport in Molecular Materials: An Assessment of Computational Methods. *Chem. Rev.* **117**, 10319–10357 (2017).

108. Tsumura, A., Koezuka, H. & Ando, T. Macromolecular electronic device: Field-effect transistor with a polythiophene thin film. *Appl. Phys. Lett.* **49**, 1210–1212 (1986).

109. Li, H. *et al.* High-mobility field-effect transistors from large-area solution-grown aligned C 60 single crystals. *J. Am. Chem. Soc.* **134**, 2760–2765 (2012).

110. Jurchescu, O. D., Popinciuc, M., Van Wees, B. J. & Palstra, T. T. M. Interface-controlled, high-mobility organic transistors. *Adv. Mater.* **19**, 688–692 (2007).

111. Coropceanu, V. *et al.* Charge transport in organic semiconductors. *Chem. Rev.* **107**, 926–952 (2007).

112. Troisi, A. Charge transport in high mobility molecular semiconductors: Classical models and new theories. *Chem. Soc. Rev.* **40**, 2347–2358 (2011).

113. Grozema, F. C. & Siebbeles, L. D. A. Mechanism of charge transport in self-organizing

organic materials. *Int. Rev. Phys. Chem.* **27**, 87–138 (2008).

114. Yang, H. Modelling charge transport in organic semiconducting materials. *Ph.D. Diss. Univ. Coll. london* (2018) doi:10.1201/9780203747230-1.

115. Bredas, J. L. & Street, G. B. Polarons, bipolarons, and solitons in conducting polymers. *Acc. Chem. Res.* **18**, 309–315 (1985).

116. Dong, H., Fu, X., Liu, J., Wang, Z. & Hu, W. 25th anniversary article: Key points for high-mobility organic field-effect transistors. *Adv. Mater.* **25**, 6158–6183 (2013).

117. Asher, M. *et al.* Anharmonic lattice vibrations in small-molecule organic semiconductors. *Adv. Mater.* **32**, 1908028 (2020).

118. Fratini, S., Mayou, D. & Ciuchi, S. The transient localization scenario for charge transport in crystalline organic materials. *Adv. Funct. Mater.* **26**, 2292–2315 (2016).

119. Illig, S. *et al.* Reducing dynamic disorder in small-molecule organic semiconductors by suppressing large-Amplitude thermal motions. *Nat. Commun.* **7**, 1–10 (2016).

120. O'Brien, G. A., Quinn, A. J., Tanner, D. A. & Redmond, G. A single polymer nanowire photodetector. *Adv. Mater.* **18**, 2379–2383 (2006).

121. Dong, H., Zhu, H., Meng, Q., Gong, X. & Hu, W. Organic photoresponse materials and devices. *Chem. Soc. Rev.* **41**, 1754–1808 (2012).

122. Nawaz, A. *et al.* High mobility organic field-effect transistors based on defect-free regioregular poly(3-hexylthiophene-2,5-diyl). *Org. Electron.* **38**, 89–96 (2016).

123. Genet, C. & Ebbesen, T. W. Light in tiny holes. *Nature* **445**, 39–46 (2007).

124. Lehn, J. M. Supramolecular chemistry - Molecular information and the design of supramolecular materials. *Makromol. Chem., Macromol. Symp.* **69**, 1–17 (1993).

125. Würthner, F. Dipole-dipole interaction driven self-assembly of merocyanine dyes: From dimers to nanoscale objects and supramolecular materials. *Acc. Chem. Res.* **49**, 868–876 (2016).

126. Adhikari, B. *et al.* Light-induced unfolding and refolding of supramolecular polymer nanofibres. *Nat. Commun.* **8**, 1–10 (2017).

127. Cravotto, G. & Cintas, P. Molecular self-assembly and patterning induced by sound waves. The case of gelation. *Chem. Soc. Rev.* **38**, 2684–2697 (2009).

128. Ajayaghosh, A. & George, S. J. First phenylenevinylene based organogels: self-assembled nanostructures via cooperative hydrogen bonding and π-stacking. *J. Am. Chem. Soc.* **123**, 5148–5149 (2001).

129. Guo, C. L. *et al.* Long-range mechanical force enables self-assembly of epithelial tubular patterns. *Proc. Natl. Acad. Sci. U. S. A.* **109**, 5576–5582 (2012).

130. Bitter, S. *et al.* Ferro-self-assembly: Magnetic and electrochemical adaptation of a multiresponsive zwitterionic metalloamphiphile showing a shape-hysteresis effect. *Chem. Sci.* **12**, 270–281 (2021).

131. Quint, M. T. *et al.* Plasmon-actuated nano-assembled microshells. *Sci. Rep.* **7**, 1–11 (2017).

132. Montali, A., Smith, P. & Weder, C. Poly(p-phenylene ethynylene)-based light-emitting devices. *Synth. Met.* **97**, 123–126 (1998).

133. Kushida, S. *et al.* Light-emitting electrochemical cells based on conjugated ion gels. *ACS Appl. Mater. Interfaces* **12**, 38483–38489 (2020).

134. Perahia, D., Traiphol, R. & Bunz, U. H. F. From single molecules to aggregates to gels in dilute solution: Self-organization of nanoscale rodlike molecules. *J. Chem. Phys.* **117**, 1827–1832 (2002).

135. Huang, W. Y., Matsuoka, S., Kwei, T. K. & Okamoto, Y. Aggregation and gelation of fully conjugated rigid-rod polymers. Poly(2,5-dialkyl-1, 4-phenyleneethynylene)s. *Macromolecules* **34**, 7166–7171 (2001).

136. Bunz, U. H. F. *et al.* Photophysics of poly[p-(2,5-didodecylphenylene)ethynylene] in

thin films. *Macromolecules* **38**, 5892–5896 (2005).

137. Levitus, M. *et al.* Steps to demarcate the effects of chromophore aggregation and planarization in poly(phenyleneethynylene)s. 1. Rotationally interrupted conjugation in the excited states of 1,4-bis(phenylethynyl)benzene. *J. Am. Chem. Soc.* **123**, 4259–4265 (2001).

138. Zagami, R., Romeo, A., Castriciano, M. A. & Monsù Scolaro, L. Inverse kinetic and equilibrium isotope effects on self-assembly and supramolecular chirality of porphyrin J-aggregates. *Chem. - A Eur. J.* **23**, 70–74 (2017).

139. Li, H. *et al.* Isotope and hydrogen-bond effects on the self-assembly of macroions in dilute solution. *Chem. - A Eur. J.* **25**, 16288–16293 (2019).

140. Van Hook, W. A. Isotope effects in chemistry. *Nukleonika* **56**, 217–240 (2011).

141. Zhan, Y. Y. *et al.* Polarizability and isotope effects on dispersion interactions in water. *Commun. Chem.* **2**, 1–8 (2019).

142. Kar, S., Swathi, K., Sissa, C., Painelli, A. & Thomas, K. G. Emergence of chiroptical properties in molecular assemblies of phenyleneethynylenes: The role of quasi-degenerate excitations. *J. Phys. Chem. Lett.* **9**, 4584–4590 (2018).

143. Bunz, U. H. F. Poly(aryleneethynylene)s: Syntheses , properties , structures , and applications. *Chemi. Rev.* **100**, 1605–1644 (2000).

144. Antina, L. A. *et al.* Effect of ms-substitution on aggregation behavior and spectroscopic properties of BODIPY dyes in aqueous solution, Langmuir-Schaefer and poly(methyl methacrylate) thin films. *Colloids Surfaces A Physicochem. Eng. Asp.* **618**, 126449 (2021).

145. Ouyang, J. ‘Secondary doping’ methods to significantly enhance the conductivity of PEDOT:PSS for its application as transparent electrode of optoelectronic devices. *Displays* **34**, 423–436 (2013).

146. Ouyang, J. *et al.* On the mechanism of conductivity enhancement in poly(3,4-ethylenedioxythiophene):poly(styrene sulfonate) film through solvent treatment. *Polym. Commun.* **45**, 8443–8450 (2004).

147. Hosseini, E., Ozhukil Kollath, V. & Karan, K. The key mechanism of conductivity in PEDOT:PSS thin films exposed by anomalous conduction behaviour upon solvent-doping and sulfuric acid post-treatment. *J. Mater. Chem. C* **8**, 3982–3990 (2020).

148. Moujoud, A., Oh, S. H., Shin, H. S. & Kim, H. J. On the mechanism of conductivity enhancement and work function control in PEDOT:PSS film through UV-light treatment. *Phys. Status Solidi Appl. Mater. Sci.* **207**, 1704–1707 (2010).

149. Huang, J., Miller, P. F., De Mello, J. C., De Mello, A. J. & Bradley, D. D. C. Influence of thermal treatment on the conductivity and morphology of PEDOT/PSS films. *Synth. Met.* **139**, 569–572 (2003).

150. Watts, R. A., Preist, T. W. & Sambles, J. R. Sharp surface-plasmon resonances on deep diffraction gratings. *Phys. Rev. Lett.* **79**, 3978–3981 (1997).

151. Ebbesen, T. W., Lezec, H. J., Ghaemil, H. F., Thiol, T. & Wolff, P. A. Extraordinary optical transmission through sub-wavelengthhole arrays. *Nature* **391**, 667–669 (1998).

152. Cao, Q. & Lalanne, P. Negative role of surface plasmons in the transmission of metallic gratings with very narrow slits. *Phys. Rev. Lett.* **88**, 4 (2002).

153. Barnes, W. L., Dereux, A. & Ebbesen, T. W. Surface plasmon subwavelength optics. *Nature* **424**, 824–830 (2003).

154. Catrysse, P. B., Shin, H. & Fan, S. Propagating modes in subwavelength cylindrical holes. *J. Vac. Sci. Technol. B Microelectron. Nanom. Struct.* **23**, 2675 (2005).

155. Van Der Molen, K. L. *et al.* Role of shape and localized resonances in extraordinary transmission through periodic arrays of subwavelength holes: Experiment and theory. *Phys. Rev. B* **72**, 1–9 (2005).

156. De Dood, M. J. A., Driessen, E. F. C., Stolwijk, D. & Van Exter, M. P. Observation of coupling between surface plasmons in index-matched hole arrays. *Phys. Rev. B - Condens. Matter Mater. Phys.* **77**, 1–5 (2008).

157. Zayats, A. V., Smolyaninov, I. I. & Maradudin, A. A. Nano-optics of surface plasmon polaritons. *Phys. Rep.* **408**, 131–314 (2005).

158. Degiron, A., Lezec, H. J., Yamamoto, N. & Ebbesen, T. W. Optical transmission properties of a single subwavelength aperture in a real metal. *Opt. Commun.* **239**, 61–66 (2004).

159. Degiron, A. & Ebbesen, T. W. The role of localized surface plasmon modes in the enhanced transmission of periodic subwavelength apertures. *J. Opt. A Pure Appl. Opt.* **7**, 590–596 (2005).

160. Bravo-Abad, J., Martín-Moreno, L., García-Vidal, F. J., Hendry, E. & Gómez Rivas, J. Transmission of light through periodic arrays of square holes: From a metallic wire mesh to an array of tiny holes. *Phys. Rev. B - Condens. Matter Mater. Phys.* **76**, 1–4 (2007).

161. Pang, Y., Genet, C. & Ebbesen, T. W. Optical transmission through subwavelength slit apertures in metallic films. *Opt. Commun.* **280**, 10–15 (2007).

162. Porto, J. A., García-Vidal, F. J. & Pendry, J. B. Transmission resonances on metallic gratings with very narrow slits. *Phys. Rev. Lett.* **83**, 2845–2848 (1999).

163. Astilean, S., Lalanne, P. & Palamaru, M. Light transmission through metallic channels much smaller than the wavelength. *Opt. Commun.* **175**, 265–273 (2000).

164. García-Vidal, F. J. & Martín-Moreno, L. Transmission and focusing of light in one-dimensional periodically nanostructured metals. *Phys. Rev. B - Condens. Matter Mater. Phys.* **66**, 1–10 (2002).

165. Lalanne, P., Hugonin, J. P., Astilean, S., Palamaru, M. & Möller, K. D. One-mode model and Airy-like formulae for one-dimensional metallic gratings. *J. Opt. A Pure Appl. Opt.*

2, 48–51 (2000).

166. Takakura, Y. Optical resonance in a narrow slit in a thick metallic screen. *Phys. Rev. Lett.* **86**, 5601–5603 (2001).

167. Charbonneau, R., Lahoud, N., Mattiussi, G. & Berini, P. Demonstration of integrated optics elements based on long-ranging surface plasmon polaritons. *Opt. Express* **13**, 977 (2005).

168. Berini, P. Plasmon-polariton waves guided by thin lossy metal films of finite width: Bound modes of symmetric structures. *Phys. Rev. B - Condens. Matter Mater. Phys.* **61**, 10484–10503 (2000).

169. Menghrajani, K. S., Nash, G. R. & Barnes, W. L. Vibrational strong coupling with surface plasmons and the presence of surface plasmon stop bands. *ACS Photonics* **6**, 2110–2116 (2019).

170. Menghrajani, K. S., Fernandez, H. A., Nash, G. R. & Barnes, W. L. Hybridization of multiple vibrational modes via strong coupling using confined light fields. *Adv. Opt. Mater.* **7**, 1900403 (2019).

171. Hasan, D., Ho, C. P., Pitchappa, P. & Lee, C. Plasmonic cavity assisted dipolar resonance enhancement and optical magnetism at mid IR. *Int. Conf. Opt. MEMS Nanophotonics* 1–2 (2015) doi:10.1109/OMN.2015.7288839.

172. Břínek, L. *et al.* Plasmon resonances of mid-IR antennas on absorbing substrate: optimization of localized plasmon-enhanced absorption upon strong coupling effect. *ACS Photonics* **5**, 4378–4385 (2018).

173. Chang, Y., Yao, J., Wu, X., Wu, D. & Liu, X. Strong and weak couplings in molecular vibration–plasmon hybrid structures. *Opt. Express* **27**, 1479 (2019).

174. Brawley, Z. T., Storm, S. D., Contreras Mora, D. A., Pelton, M. & Sheldon, M. Angle-independent plasmonic substrates for multi-mode vibrational strong coupling with

molecular thin films. *J. Chem. Phys.* **154**, 104305 (2021).

175. De Kok, M. M. *et al.* Modification of PEDOT:PSS as hole injection layer in polymer LEDs. *Phys. Status Solidi Appl. Res.* **201**, 1342–1359 (2004).

176. Zhang, S. *et al.* Tuning the electromechanical properties of PEDOT:PSS films for stretchable transistors and pressure sensors. *Adv. Electron. Mater.* **5**, 1–7 (2019).

177. Shi, W. *et al.* Micron-thick highly conductive pedot films synthesized via self-inhibited polymerization: Roles of anions. *NPG Asia Mater.* **9**, 405 (2017).

178. Jonas, F. & Schrader, L. Conductive modifications of polymers with polypyrroles and polythiophenes. *Synth. Met.* **41**, 831–836 (1991).

179. Heywang, G. & Jonas, F. Poly(alkylenedioxythiophene)s - New, very stable conducting polymers. *Adv. Mater.* **4**, 116–118 (1992).

180. Bayer, A. G. Polythiophenes, process for their preparation and their use. *US-4959430-A, 339340* 339–340 (1988).

181. Jonas, F., Krafft, W. & Muys, B. Poly(3,4-ethylenedioxythiophene): Conductive coatings, technical applications and properties. *Macromol. Symp.* **100**, 169–173 (1995).

182. Vitoratos, E. *et al.* Thermal degradation mechanisms of PEDOT:PSS. *Org. Electron.* **10**, 61–66 (2009).

183. Chen, S. *et al.* Thickness dependent thermal performance of a poly(3,4-ethylenedioxythiophene) thin film synthesized: Via an electrochemical approach. *RSC Adv.* **12**, 1897–1903 (2022).

184. Bora, P. J., Anil, A. G., Vinoy, K. J. & Ramamurthy, P. C. Outstanding absolute electromagnetic interference shielding effectiveness of cross-linked PEDOT:PSS film. *Adv. Mater. Interfaces* **6**, (2019).

185. Winter, I., Reese, C., Hormes, J., Heywang, G. & Jonas, F. The thermal ageing of poly(3,4-ethylenedioxythiophene). An investigation by X-ray absorption and X-ray

photoelectron spectroscopy. *Chem. Phys.* **194**, 207–213 (1995).

186. Shi, Y. *et al.* Degradation phenomena and degradation mechanisms for highly conductive PEDOT:PSS films. *Mater. Lett.* **308**, 131106 (2022).

187. Pasha, A., Khasim, S., Al-Hartomy, O. A., Lakshmi, M. & Manjunatha, K. G. Highly sensitive ethylene glycol-doped PEDOT-PSS organic thin films for LPG sensing. *RSC Adv.* **8**, 18074–18083 (2018).

188. Vermang, B. *et al.* On the blistering of atomic layer deposited Al2O3 as Si surface passivation. *Conf. Rec. IEEE Photovolt. Spec. Conf.* 3562–3567 (2011).

189. Kirihara, K., Wei, Q., Mukaida, M. & Ishida, T. Reduction of specific contact resistance between the conducting polymer PEDOT:PSS and a metal electrode by addition of a second solvent during film formation and a post-surface treatment. *Synth. Met.* **246**, 289–296 (2018).

190. Pretl, S., Hamacek, A., Reboun, J. & Stulik, J. Contact properties of PEDOT : PSS. *4th Electron. Syst. Technol. Conf.* 1–6 (2012) doi:doi: 10.1109/ESTC.2012.6542214.

191. Kim, J. Y., Jung, J. H., Lee, D. E. & Joo, J. Enhancement of electrical conductivity of poly(3, 4-ethylenedioxythiophene)/poly(4-styrenesulfonate) by a change of solvents. *Synth. Met.* **126**, 311–316 (2002).

192. Nardes, A. M. *On the conductivity of PEDOT:PSS thin films*. *Ph.D. dissertation, Eindhoven University of Technilogy* (2007).

193. Ebbesen, T. W. Hybrid light-matter states in a molecular and material science perspective. *Acc. Chem. Res.* **49**, 2403–2412 (2016).

194. Canaguier-Durand, A., Genet, C., Lambrecht, A., Ebbesen, T. W. & Reynaud, S. Non-Markovian polariton dynamics in organic strong coupling. *Eur. Phys. J. D* **69**, 1–7 (2015).

195. Mabesoone, M. F. J., Palmans, A. R. A. & Meijer, E. W. Solute-solvent interactions in

modern physical organic chemistry: Supramolecular polymers as a muse. *J. Am. Chem. Soc.* **142**, 19781–19798 (2020).

196. Hirai, K., Ishikawa, H., Takahashi, Y., Hutchison, J. A. & Uji-i, H. Autotuning of vibrational strong coupling for site-selective reactions. *Chem. – A Eur. J.* e202201260 (2022).

197. Nagarajan, K. *et al.* SI Conductivity and Photoconductivity of a p-Type Organic Semiconductor under Ultrastrong Coupling. *ACS Nano* **14**, 10219–10225 (2020).

ACKNOWLEDGEMENTS

First and foremost, I would like to thank Prof. Thomas W. Ebbesen for the opportunity to work in this lab (Laboratoire des Nanostructures) and for his guidance and support over these three years, it has helped me to grow both on personal and scientific level.

I would like to express my gratitude to Prof. Abraham Nitzan, Prof. Aloise Degiron, and Prof. Petra Hellwig for accepting to be on my thesis Jury and for their valuable comments to improve my thesis.

I would also like to thank Dr. Cyriaque Genet for his kind advice and for correcting the thesis. I am thankful to Dr. Eloise Devaux for the suggestions regarding the experiments, and for solving all the technical problems, which helped in the smooth running of my experiments.

Moreover, I am grateful to all the members of the nanostructures lab – office partner Kuidong wang for all the scientific and non-scientific discussions and frequent Lamian trips, Shahana NS for the weekend getaways, and all the other adventures that we explored together, Soh Kushida for all the discussions and football training, Bianca Patrahau for all the experimental discussions and updates on Europe music industry, Jerome Gautier for the French translations and helping with the never-ending administrative processes, Yoichi Sasaki for the curious scientific discussions and skiing lessons, Luis for being a bouldering partner and a great friend, Remi Georlich for all the discussions, and Sudipta Saha for explaining physics in simple language.

To all the previous members in the lab – Yantao Pang, Anoop Thomas, Robrecht Vergauve, Gian Lorenzo Paravicini-Bagliani, Sandeep Kulangara and Kalaivanan Nagarajan, thank you for creating a vibrant lab environment and for sharing your vast scientific knowledge.

Also, to other former extraordinary colleagues – Samuel Albert, Yoseline Rosales-Cabara, Minghao Li, and Antoine, thank you for the friendly and cheerful work environment. I am also grateful to the new members of the lab – Arthur Fonseca and Weijian Tao.

I would also like to thank Marie-Claude Jouaiti for taking care of all the administrative protocols and simplifying the entire process.

I am grateful to all the UHMob members for the intriguing scientific and non-scientific discussions.

I would like to thank StrasMa (Anoop, Jincy, Gia, Kalaivanan, Priyanka, Venba, Sruthi, Aromal, Shahana, Shana, Christeena, Anjana, Adarsh, Vishnu, and others) for all the good memories.

Deepest gratitude to my parents, Joel and Ammachi for their unconditional love, support, and motivation.

Thank you all,

Kripa

LIST OF PUBLICATIONS

JOURNAL PUBLICATIONS

- Y. Pang, A. Thomas, K. Nagarajan, R.Vergauwe, K. Joseph, B. Patrahau, K. Wang, C. Genet, T. W. Ebbesen. **On the role of symmetry in vibrational strong coupling: The case of charge-transfer complexation.** *Angew. Chem. Int. Ed.* **2020**, 132, 10522-10526.

- K. Nagarajan, J. George, A. Thomas, E. Devaux, T. Chervy, S. Azzini, K. Joseph, A. Jouaiti, M. W. Hosseini, A. Kumar, C. Genet, N. Bartolo, C. Ciuti, T. W. Ebbesen. **Conductivity and photoconductivity of a p-type organic semiconductor under ultra-strong coupling.** *ACS Nano* **2020**, *14*, 10219–10225.

- K. Joseph*, S. Kushida*, E. Smarsly, D. Ihiawakrim, A. Thomas, G. L. Paravicini-Bagliani, K.Nagarajan, R.Vergauwe, E. Devaux, O. Ersen, U. H. F. Bunz, T. W. Ebbesen. **Supramolecular assembly of conjugated polymers under vibrational strong coupling.** *Angew. Chem. Int. Ed.* **2021**, *60*, 19665-19670.

- S. Kulangara, K. Joseph, J. Gautier, K. Nagarajan, S. Melepatt , K. G. Thomas, T. W. Ebbesen. **Manipulating the self-assembly of phenyleneethynylenes under vibrational strong coupling.** *J. Phys. Chem. Lett.* **2022**, 13, 1209-1214.

- K. Joseph *et al*. **Conductivity of PEDOT: PSS under vibrational strong coupling. (***Manuscript in preparation)*

CONFERENCE PRESENTATIONS

- *Chemistry as Innovative Science (CHAINS), 2021* Veldhovan, Netherlands, December 7-8, 2021
  (Invited oral presentation)
  Vibrational strong coupling for altering self-assembly. K. Joseph

- *MRS Spring Meeting & Exhibit,* May 23-25, 2022 *(Poster presentation)*

Supramolecular assembly of conjugated monomers under vibrational strong coupling. K. Joseph, S. Kulangara, J. Gautier, K. Nagarajan, S. Melepatt, K. G. Thomas, T. W. Ebbesen.

- *International Conference on Non- covalent Interactions (ICNI 2022),* Strasbourg, July 18-22, 2022 (Poster presentation)
  Supramolecular assemblies under vibrational strong coupling. K. Joseph, S. Kushida, A. Thomas, K. Nagarajan, T. W. Ebbesen.

- *UHMob International Conference - Organic semiconductors: From principles to applications*, Mainz, Germany, September 6-9, 2022 (Poster presentation)
  Conductivity of PEDOT: PSS under vibrational strong coupling.
  K. Joseph *et al.*

Kripa Merin JOSEPH

Conductivity and supramolecular assembly under light-matter strong coupling

Résumé

Cette thèse explore l'effet du couplage fort lumière-matière sur les propriétés de transport des semi-conducteurs organiques en couplant leurs transitions électroniques et vibrationnelles au mode électromagnétique résonnant d'une cavité Fabry-Perot ou d'une structure plasmonique, étudiant ainsi l'amélioration du transport de charges due à la cohérence étendue et à la délocalisation des états hybrides lumière-matière. En outre, l'observation fortuite de la modification des assemblages supramoléculaires indique que le couplage vibratoire fort peut être utilisé pour contrôler et manipuler l'auto-assemblage.

Mots clés : Couplage fort lumière-matière — semiconducteurs organiques — assemblages supramoléculaires — plasmonique.

Résumé en anglais

This thesis explores the effect of light-matter strong coupling on the transport properties of organic semiconductors by coupling their electronic and vibrational transitions to the resonant electromagnetic mode of a Fabry-Perot cavity or plasmonic structure, thus studying the enhancement of charge transport due to the extended coherence and delocalization of hybrid light-matter states. In addition, the serendipitous observation of modification of supramolecular assemblies indicate that vibrational strong coupling can be used to control and manipulate self-assemblies.

Key-words: Light-matter strong coupling — organic semiconductors — supramolecular assemblies — plasmonics